UNIVERSITY OF ROCHESTER
LABORATORY FOR LASER ENERGETICS

Volume 69
October–December 1996
DOE/SF/19460-152

LLE Review

Quarterly Report

UR
LLE

About the Cover:

In OMEGA's pulse generation room (PGR) lab engineer Todd Safford (left) and senior lab engineer Todd Blalock (right) examine one of the holographic gratings used to produce 2-D SSD (smoothing by spectral dispersion). The 3.3-GHz electro-optic modulator (seen through an IR mirror) is clearly visible on the left. The 2-D SSD subsystem comprises eight gratings, two modulators, and a variety of conventional optics spanning 80 ft of optical path within the PGR.

The work described in this volume includes current research at the Laboratory for Laser Energetics, which is supported by New York State Energy Research and Development Authority, the University of Rochester, the U.S. Department of Energy Office of Inertial Confinement Fusion under Cooperative Agreement No. DE-FC03-92SF19460, and other agencies.

Printed in the United States of America
Available from
National Technical Information Services
U.S. Department of Commerce
5285 Port Royal Road
Springfield, VA 22161

Price codes: Printed Copy A03
Microfiche A01

For questions or comments, contact Richard Town, *Editor*, Laboratory for Laser Energetics, 250 East River Road, Rochester, NY 14623-1299, (716) 275-1440.

UNIVERSITY OF ROCHESTER
LABORATORY FOR LASER ENERGETICS

Volume 69
October–December 1996
DOE/SF/19460-152

LLE Review

Quarterly Report

UR LLE

Contents

In Brief iii

Two-Dimensional SSD on OMEGA 1

Areal Density Measurement of Laser Targets Using Absorption Lines 11

Modeling the Temporal-Pulse-Shape Dynamics of an Actively Stabilized Regenerative Amplifier for OMEGA Pulse-Shaping Applications 18

Multiple Scale Derivation of the Relativistic Ponderomotive Force 24

Subpicosecond Imaging Based on Electro-Optic Effect 36

Nuclear Diagnostics for High-Density Implosions 46

Publications and Conference Presentations

In Brief

This volume of the LLE Review, covering the period October–December 1996, includes a review of 2-D SSD as implemented on the OMEGA laser system. A summary of the detailed mathematical formalism is shown, and the predicted level of uniformity achievable on OMEGA is given. The first experimental results on uniformity using narrow-band 2-D SSD are compared to theoretical calculations. Excellent agreement between experiment and theory is found, which gives confidence that broadband 2-D SSD with polarization wedges should achieve an rms nonuniformity in the 1%–2% level necessary for cryogenic implosion experiments.

Other highlights of research presented in this issue are

- A method for measuring the areal density $\rho\Delta r$ of the compressed shell based on the observation of absorption lines from a titanium-doped layer. The method is tested using a simulated spectrum from a one-dimensional *LILAC* simulation. The predicted peak $\rho\Delta r$ of the compressed shell was within 17% of the value calculated directly from *LILAC*.

- A description of modeling the temporal-pulse-shape dynamics of the regenerative amplifier. The laser rate equations are presented along with a discussion of the regen dynamics. Excellent agreement is found between the model's predicted output and the experimentally observed output. It is now possible to model the entire OMEGA laser system, enabling on-target pulse shapes to be specified.

- A detailed analysis of the relativistic pondermotive force. A guiding center model is postulated, which is compared to numerical simulation of the actual particle motion. The formula is also verified analytically using the method of multiple scales. Work continues on this formalism to study the effects of the pondermotive force on laser-plasma interactions.

- A description of an electro-optic sampling system capable of imaging the voltage distribution over a rectangular region. The system is comparable to an ultrafast sampling oscilloscope with more than 180,000 channels.

- Methods to measure the fuel compression using nuclear diagnostics. The three ρR diagnostics being developed for OMEGA are reviewed. A discussion of future developments is presented.

Richard Town
Editor

Two-Dimensional SSD on OMEGA

The ultimate goal of the LLE uniformity program is to reduce the rms laser-irradiation nonuniformity to the 1%–2% level, which is required for cryogenic implosion experiments on OMEGA. The combination of distributed phase plates (DPP's), two-dimensional (2-D) smoothing by spectral dispersion (SSD), polarization wedges, and beam overlap should be sufficient to reach this goal. We present here a discussion of the mathematical formalism of 2-D SSD with numerical calculations illustrating the levels of uniformity that can be achieved on OMEGA. The initial implementation of 2-D SSD is described, and the initial experimental results for uniformity are compared with theory.

2-D SSD Concept

The level of uniformity that can be achieved with SSD is determined by two factors: bandwidth and spectral dispersion. The amount of bandwidth determines the rate of smoothing, and the amount of spectral dispersion determines the maximum reduction in nonuniformity that can be achieved (as well as the longest spatial wavelength of nonuniformity that can be smoothed). Frequency-tripled glass lasers place constraints on both bandwidth and spectral dispersion. Current techniques for the high-efficiency frequency tripling of laser light limit the (full-width) bandwidth to 3 Å to 4 Å in the IR for OMEGA. Spatial-filter pinholes in the laser chain limit the spectral spread of the beam to five to ten times the beam's IR diffraction limit. With these constraints, the levels of uniformity required for OMEGA experiments can be achieved using SSD.

The starting point for a description of the uniformity that can be achieved by 2-D SSD is the speckle pattern produced by a phase plate. An example is shown in Fig. 69.1(a). It is characterized by a smooth, well-defined intensity envelope on target. However, superposed on the envelope is highly modulated intensity structure (known as speckle), which is produced by interference between light that has passed through different portions of the phase plate. SSD smoothes this speckle structure in time by progressing through a sequence of many copies of this speckle pattern, each shifted in space, so that peaks of some fill in the valleys of others at different times. When averaged in time, this effect is qualitatively similar to whole-beam deflection: 1-D SSD has the effect of sweeping the beam in only one direction, and 2-D SSD is similar to sweeping the beam in two dimensions.

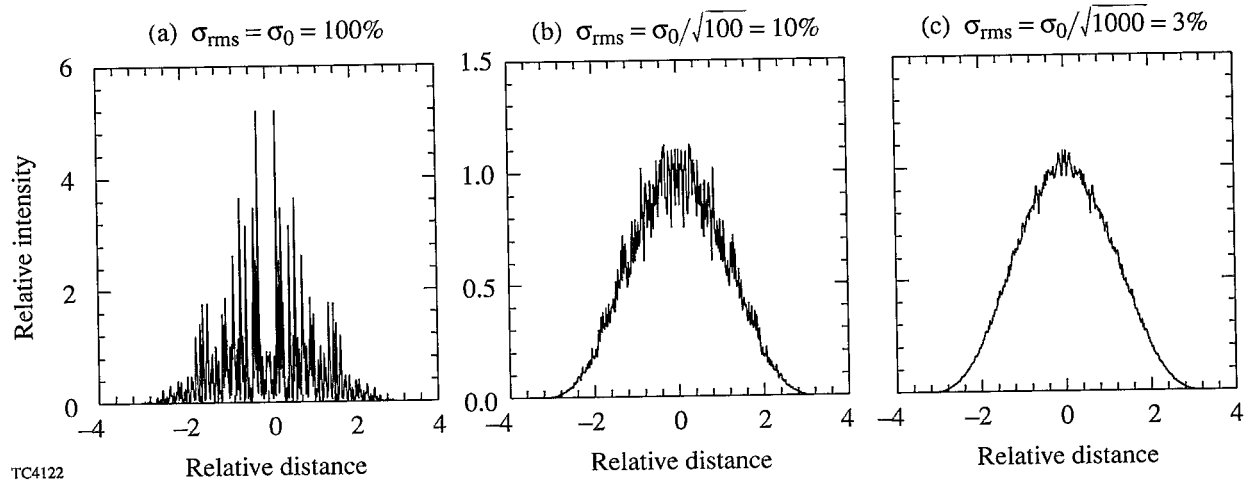

Figure 69.1
The effect of overlapping a large number of statistically different speckle patterns. For a single pattern the rms nonuniformity $\sigma_{rms} = 100\%$. For N patterns, the rms nonuniformity is reduced by $1/\sqrt{N}$.

The reduction in rms nonuniformity is statistical in nature. Patterns shifted by more than about 1/2 of a speckle width act as entirely different random speckle patterns. The overlap of N random speckle patterns reduces the rms nonuniformity σ_{rms} by $1/\sqrt{N}$. Examples in Figs. 69.1(b) and 69.1(c) show how 100 and 1,000 overlapping speckle patterns reduce the phase plate σ_{rms} of 100% to values of 10% and 3%, respectively. OMEGA will require 2000 to 10,000 of such overlapping patterns, produced as follows: 2-D SSD will provide ~500 of the speckle patterns (for a 1-ns smoothing time); the polarization shifter will provide an additional factor of 2; and multiple-beam overlap will provide another factor of ~4, for a resulting nonuniformity of 1%–2%.

SSD generates these shifted speckle patterns in a two-step process.[1] The beam is passed through an electro-optic modulator, which imposes a small spread of frequencies (bandwidth) upon the laser light. The bandwidth is then spectrally dispersed by means of diffraction gratings. For 1-D SSD, one modulator is used. For 2-D SSD, two modulators (of different frequencies) are used, with diffraction gratings oriented such that each bandwidth is dispersed in a perpendicular direction. Because of the dispersion, each spectral component focuses onto the target in a slightly different position, producing the required shifted speckle patterns (Fig. 69.2).

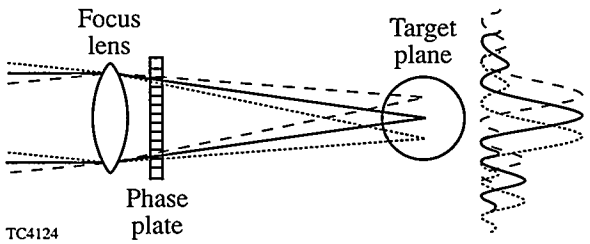

Figure 69.2
Schematic illustrating the use of spectral dispersion to generate overlapping speckle patterns. The different spectral modes are spatially shifted in the target plane. Speckle patterns that are shifted by more than 1/2 of a speckle size are statistically independent.

The spectral dispersion does not reduce the speckle fluctuations instantaneously. It creates an entirely different speckle pattern, but one that changes in time. Interference between the electric fields from different sections of the beam will fluctuate in time because of their different frequencies, and the time-averaged interference approaches zero at a rate inversely proportional to the difference in frequency. As the contributions from interference become small, the time-averaged uniformity "smoothes" to the result expected from superposing shifted intensity profiles, each corresponding to a different frequency.

The time-averaged uniformity approaches an asymptotic level that is determined by the number of statistically independent speckle patterns (which is generally smaller than the number of spectral components with different frequencies). This depends on the ratio between the maximum spatial shift (S_{max}) that can be produced by the laser and the smallest shift (S_{min}) that will produce statistical smoothing. The maximum spatial shift S_{max} is defined as the full-width distance in the target plane that rays in the laser beam are deflected by SSD dispersion. The smallest shift S_{min} is 1/2 of a speckle size and is given by

$$S_{min} = F\lambda/D, \tag{1}$$

where F is the focal length, λ is the UV wavelength, and D is the diameter of the focus lens. The maximum shift S_{max} is determined by the maximum angular spread of the light that can propagate through the spatial-filter pinholes of the laser (Fig. 69.3). This can be conveniently expressed as a multiple s of the whole beam diffraction limit (pinhole sizes are often expressed in terms of this parameter). Thus,

$$S_{max} = s \cdot (2.4\ F\lambda/D). \tag{2}$$

Currently, OMEGA pinholes can accommodate $s = 15$, while $s = 30$ is planned for the future. (Note: In this article s is quoted in terms of UV wavelength; if expressed in terms of the IR wavelength, s should be decreased by a factor of 3.) In terms of these parameters, the number of statistically independent speckle patterns (N_{stat}) is

$$N_{stat} = (S_{max}/S_{min})^2 = (2.4\,s)^2, \tag{3}$$

where the ratio is squared because 2-D SSD allows spectral shifting in two directions. (This estimate for N_{stat} is somewhat simplified because it assumes that all 2-D SSD modes have different frequencies and are therefore independent; more accurate calculations are given in the next section.) The current and future values of N_{stat} are 1300 and 5000 for OMEGA, which, by itself, should reduce the rms speckle fluctuation to 3% and 1.5%, respectively, in the asymptotic limit. For 1-D SSD, $N_{stat} = 2.4\,s$, with the asymptotic nonuniformity about a factor of 5 larger.

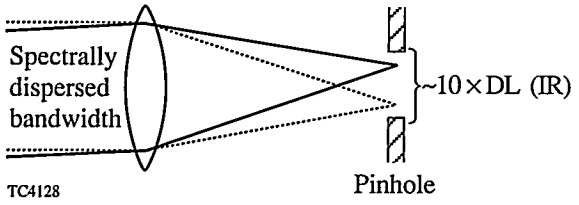

Figure 69.3
Schematic illustrating the limitation imposed by the spatial-filter pinholes on the amount of spectral dispersion that can propagate through the laser chain. Since the minimum separation between modes in the target plane is 1/2 the speckle size, the pinholes provide an upper limit on the number of modes available for smoothing.

For the current OMEGA pinhole size ($s=15$), $S_{max}=76\,\mu$m; thus, the bandwidth and grating dispersion are chosen such that rays from each phase-plate element are deflected ±38 μm during an SSD modulation cycle. This is small in comparison with a typical target diameter (~1 mm); the performance of SSD is thus limited not by the finite target size but by the selection of pinholes in the laser system.

In addition to the asymptotic level of uniformity, the rate of smoothing is of crucial importance. Smoothing must occur before the target can significantly respond to the laser nonuniformity. A rough estimate for the rate of smoothing provided by SSD can be obtained from the following argument. The rms nonuniformity, averaged over time T, will decrease with the number of noninterfering spectral components N_T as $1/\sqrt{N_T}$. (The time-averaged nonuniformity will continue to decrease until $N_T = N_{stat}$, and then it will asymptote.) The smallest frequency difference $\delta\nu$ for which interference is negligible is roughly $\delta\nu = 1/T$. For a bandwidth $\Delta\nu$, one has $N_T = \Delta\nu/\delta\nu = \Delta\nu T$. Thus, the rms nonuniformity decreases as $1/\sqrt{\Delta\nu T}$. As an example, with $\Delta\nu = 300$ GHz (equivalent to an IR bandwidth of 3 Å) and $T = 1$ ns, one finds $N_T \approx 300$. This value of N_T is less than N_{stat} for a spectral separation of 15 times diffraction limit, so that smoothing will continue beyond 1 ns (but such large smoothing times might be too long to affect target performance).

This rate of smoothing is expected to be fast enough to perform the high-compression experiments planned for OMEGA. When combined with polarization shifters and beam overlap, the resulting nonuniformity will be in the range of 1% to 2% with a smoothing time of ~500 ps. Higher levels of uniformity could be achieved with the development of new technologies for tripling larger bandwidths. New tripling crystals with a larger bandwidth acceptance are under investigation, as are improved tripling configurations using existing materials. One option under consideration is to vary the bandwidth in time. At early times, when the intensity is low and high irradiation uniformity is critical, the bandwidth would be large. At these intensities the bandwidth acceptance of the tripling crystals is larger, thus maintaining efficiency. Near the peak of the pulse where high tripling efficiency is crucial, but where laser uniformity can be relaxed because of the smoothing characteristics of the plasma atmosphere that has formed around the target, the bandwidth can be reduced.

2-D SSD Formalism and Results

The principal components of 2-D SSD are shown schematically in Fig. 69.4. With this configuration the bandwidth imposed by the two modulators will be dispersed in two perpendicular directions.

The effect of this configuration on the laser's electric field can be determined approximately from the following treatment. The electric field of the laser entering the first diffraction grating can be written as

$$E(t) = E_0(t)e^{i\omega t}, \tag{4}$$

where the spatial dependence has been suppressed, and the pulse-shape dependence is contained in $E_0(t)$. The first grating in Fig. 69.4 will introduce a time shear across the beam in the x direction, which is equivalent to spectral dispersion. (The directions of dispersion will be referred to as x or y and are perpendicular to the direction of propagation. The change in propagation direction produced by each grating is not shown in Fig. 69.4 and is not relevant to the present discussion.) With the time shear, the electric field becomes

$$E_1(t,x) = E_0(t-\beta x)e^{i\omega(t-\beta x)}, \tag{5}$$

where β is related to the grating dispersion $(\Delta\theta/\Delta\lambda)$ by

$$\beta = \frac{2\pi}{\omega}\left(\frac{\Delta\theta}{\Delta\lambda}\right). \tag{6}$$

The quantity $D\beta$ (where D is the beam diameter) remains invariant throughout the laser chain as the beam diameter changes size; its value is the time delay across the beam. For parameters at the end of the IR portion of the laser ($\Delta\theta/\Delta\lambda =$ 31 μrad/Å, $D \approx 30$ cm, $\omega \approx 1.8\times10^{15}$ s^{-1}), the time delay $D\beta$ is about 300 ps.

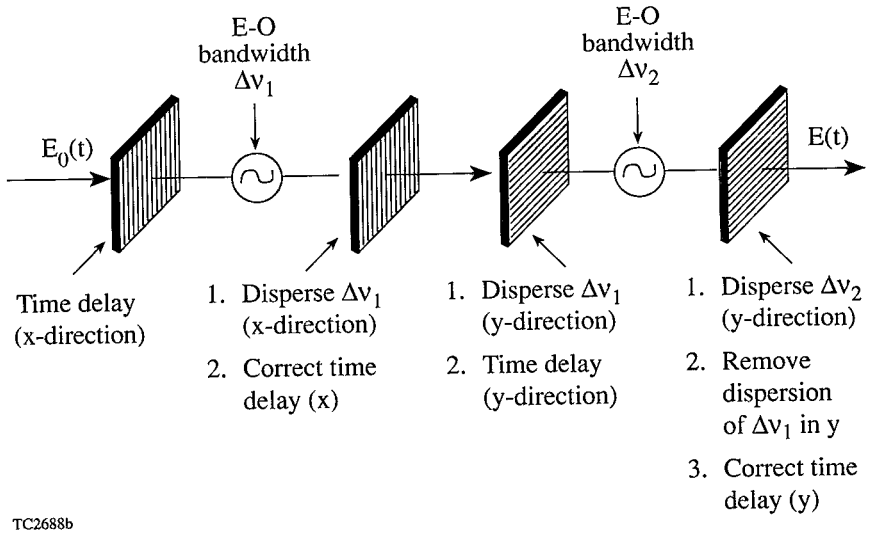

Figure 69.4
Schematic of 2-D SSD, illustrating how the bandwidths from the two modulators are dispersed in perpendicular directions.

The first electro-optic modulator introduces sinusoidal phase-modulated bandwidth to E_1, with amplitude δ_1 and angular frequency ω_1. The resulting electric field is

$$E_2(t,x) = E_0(t-\beta x)e^{i\left[\omega(t-\beta x)+\delta_1 \sin(\omega_1 t)\right]}. \quad (7)$$

The second grating reverses the time shear of the first and disperses the bandwidth in the x direction:

$$E_3(t,x) = E_2(t+\beta x, x). \quad (8)$$

The third grating introduces a time shear in the y direction, which adds spectral dispersion in that direction. The same time shear, given by β, is used in both x and y directions, although this is not a requirement:

$$E_4(t,x,y) = E_3(t-\beta y, x). \quad (9)$$

Gratings 2 and 3 can be replaced by a single grating oriented at 45° to the gratings shown. The second electro-optic modulator introduces additional bandwidth with parameters δ_2 and ω_2. At this point the electric field is

$$E_5(t,x,y) = E_0(t-\beta y)\cdot \exp i\left[\omega(t-\beta y) + \delta_1 \sin\omega_1(t+\beta x-\beta y)+\delta_2 \sin(\omega_2 t)\right]. \quad (10)$$

(There can be an arbitrary phase difference between the two modulators, but this does not affect uniformity on target and has not been included here.) Finally, the fourth grating reverses the effect that the third grating had on the beam due to the bandwidth imposed by the first modulator, and introduces y dispersion (and a time shear) to the bandwidth from the second modulator. The resulting electric field from this configuration has the bandwidth from the first modulator dispersed only in the x direction, the bandwidth from the second modulator dispersed only in the y direction, and no time shear across the beam:

$$E = E_0(t)\cdot \exp i\left[\omega t + \delta_1 \sin\omega_1(t+\beta x) + \delta_2 \sin\omega_2(t+\beta y)\right]. \quad (11)$$

This spectrally dispersed light propagates through the laser chain, through the frequency-tripling crystals and phase plates, and through the focus lenses onto the target. For the bandwidths considered here, the main effect of frequency tripling is that the modulation amplitudes δ_1 and δ_2 are each tripled, as is the laser angular frequency ω. Frequencies at the extremes of the bandwidth will triple less efficiently than those near the center. For current frequency-tripling crystals, the difference in efficiency for bandwidths below ~4 Å does not significantly effect the uniformity.

The electric field on target (in the focal plane) is

$$E_F = E_0(t)e^{i3\omega t}\sum_{mn} J_m(3\delta_1)J_n(3\delta_2) \times \operatorname{sinc}(m\gamma_1+q)\cdot\operatorname{sinc}(n\gamma_2+p)\times e^{i(m\omega_1+n\omega_2)t} \times \sum_{KL} e^{-i\left[2(m\gamma_1+q)L+2(n\gamma_2+p)K+\phi_{KL}\right]}. \quad (12)$$

This expression includes the effect of the DPP, frequency tripling, and spectral dispersion. Here the notation of Ref. 1 has been used with a generalization to two-dimensional dispersion. For simplicity, the results are written in terms of a two-level phase plate rather than the more general DPP,[2] which is actually used on OMEGA. The main effect of the more general phase plate is to replace the "sinc" envelope shape by a more general function, but the speckle statistics are very similar. The variables are defined as follows: p and q are dimensionless variables related to y and x by the factor $k_3\Delta/2F$, where k_3 is the wave number of the frequency-tripled fundamental, Δ is the distance between phase-plate elements, F is the focal length, and $\gamma_{1,2} = \omega_{1,2}\,\beta\Delta/2$. The Bessel functions J_m and J_n are the amplitudes from a Fourier decomposition of the sinusoidal phase modulation. Formally the m-n sum extends to $\pm\infty$, but the contributions from $|m| > 3\delta_1$ and $|n| > 3\delta_2$ are very small. Thus, to a good approximation, the largest spectral modes of interest are given by $m = M \equiv 3\delta_1$ and $n = N \equiv 3\delta_2$. The K-L sum is the factor that describes the phase-plate speckle. The sum is over all phase-plate elements, each having a phase ϕ_{KL}, which is either 0 or π. Note that each spectral component (m,n) has exactly the same speckle structure but is shifted by $m\gamma_1$ in q and by $n\gamma_2$ in p.

These variables have the following physical significance. The phase-plate element size Δ is generally chosen so that the distance between the zeros of the sinc function is slightly larger than the largest target that will be irradiated (to assure good uniformity). Thus, $p, q = \pi$ is characteristic of the target radius. The total spectrally induced spreads in the two directions, as fractions of the target diameter, are approximately $M\gamma_1/\pi$ and $N\gamma_2/\pi$. The total bandwidths in the two directions are $\Delta\nu_1 = M\omega_1/\pi$ and $\Delta\nu_2 = M\omega_2/\pi$. The number of times that the phase modulation repeats across the beam is $\gamma_{1,2}K_{\max}/\pi$, where $K_{\max}$ is the number of phase-plate elements in one direction.

The laser intensity I in the focal plane is given by the square of $|E_F|$:

$$I = I_0(t)\sum_{\substack{mm'\\nn'}} J_m(3\delta_1)J_{m'}(3\delta_1)J_n(3\delta_2)J_{n'}(3\delta_2) \cdot e^{i(m\omega_1+n\omega_2-m'\omega_1-n'\omega_2)t} \times \operatorname{sinc}(m\gamma+q)\operatorname{sinc}(m'\gamma+q) \times \operatorname{sinc}(n\gamma+p)\operatorname{sinc}(n'\gamma+p) \times \sum_{\substack{KK'\\LL'}} e^{i2(L'-L)q+i2(K'-K)p} \times \left\{e^{i2\gamma(m'L'-mL+n'K'-nK)+i(\phi_{K'L'}-\phi_{KL})}\right\}. \quad (13)$$

The final summation has been written in the form of a Fourier decomposition of the speckle nonuniformity with the term in brackets being the Fourier coefficients.

The time-averaged uniformity at time t in the focal plane is

$$\langle I(t)\rangle_T = \frac{1}{T}\int_{t-T/2}^{t+T/2} I(t')dt' \quad (14)$$

for an averaging time T. To examine the smoothing effect of 2-D SSD, it is instructive to evaluate the asymptotic limit of $\langle I\rangle_T$ as $T\to\infty$. To simplify the result, consider the special case for which (1) $I_0(t)$ is constant; (2) the spectral shifts are sufficiently small that the sinc envelope is not modified; and (3) the modulation frequencies are incommensurate, i.e., $m\omega_1 \neq n\omega_2$ for all integers m and n. The resulting asymptotic uniformity can be written in the following form:

$$\langle I\rangle_\infty = I_{\text{env}}(p,q)\cdot\left[1+\sum_{k\ell\neq 0} e^{i(2kp+2\ell q)}C_{k\ell}\cdot R_{k\ell}\right], \quad (15)$$

where I_{env} is the diffraction-limited phase-plate envelope, C is the spatial autocorrelation function for the phase plate, R is the reduction in nonuniformity produced by SSD, and the summation is over the distance between phase-plate elements (i.e., $k = K' - K$ and $\ell = L' - L$). These terms are defined as follows:

$$I_{\text{env}} = I_0\operatorname{sinc}^2(p)\operatorname{sinc}^2(q)N^2, \quad (16)$$

where N^2 is the number of phase-plate elements,

$$C_{k\ell} = \sum_{KL} e^{i\left(\phi_{K+k,L+\ell}-\phi_{KL}\right)}, \quad (17)$$

and

$$R_{k\ell} = \sum_{mn} J_m^2(3\delta_1) J_n^2(3\delta_2) e^{i(2\gamma_1 m\ell + 2\gamma_2 nk)}. \quad (18)$$

Using the Bessel function identity

$$\sum_n J_n(3\delta) J_{n+v}(3\delta) e^{in\gamma\ell 2} = J_v(w) e^{iv\theta}, \quad (19)$$

where $w = 6\delta|\sin\gamma\ell|$ and $\sin\theta = (3\delta\sin\gamma\ell)/w$, the SSD reduction factor becomes

$$R_{k\ell} = J_0(6\delta_1 \sin\gamma_1\ell) \cdot J_0(6\delta_2 \sin\gamma_2 k). \quad (20)$$

In the form of Eq. (15), the nonuniformity structure has been Fourier decomposed in terms of the variables p and q, with the difference between phase-plate elements k and ℓ acting as dimensionless wave numbers. The rms fluctuation is determined by the square of the Fourier coefficients:

$$\sigma_{rms} = \left[\sum_{k\ell} |C_{k\ell} \cdot R_{k\ell}|^2\right]^{1/2}. \quad (21)$$

The phase-plate result (without SSD) is recovered for $R_{k\ell} = 1$ (for all k and ℓ), in which case the rms nonuniformity is 100%.

The SSD reduction factor depends on the spatial wavelength of the nonuniformity through k and ℓ: For $\gamma_1\ell < (6\delta_1)^{-1}$ and $\gamma_2\ell < (6\delta_2)^{-1}$ the factor $R_{k\ell}$ is approximately 1. When either k or ℓ is small, the factor reduces to the 1-D SSD result. This occurs when the wave vector for the nonuniformity points toward one of the directions of dispersion. Maximum smoothing from 2-D SSD occurs when both k and ℓ are large. Figure 69.5 shows the reduction factor $|R_{k\ell}|$ using the current OMEGA values ($\delta_1 = 5.1$, $\delta_2 = 4.6$) for the cases when one wave number is kept small ($\ell = 0$) and for the case when the wave vector is at 45° to the direction of dispersion ($\ell = k$). The improved smoothing in the second case, corresponding to two-dimensional smoothing of the nonuniformity in both directions, is apparent.

The condition that there is no significant smoothing for $6\delta_1\gamma_1\ell < 1$ has a simple physical interpretation. The factor $6\delta_1\gamma_1$ is the total spectrally induced shift S_{max} in the target plane in units of q. The parameter ℓ is related to the wavelength of nonuniformity $\Delta\lambda$ by $\Delta\lambda = \pi/\ell$ (again in units of q). Thus, the largest wavelength of nonuniformity that will be smoothed by SSD is approximately πS_{max}. In other words, the spectral shift must be a significant portion of the nonuniformity wavelength for smoothing to occur.

The amount that the speckle pattern is shifted can be doubled (in one direction) by means of a polarization shifter.[3,4] This is illustrated in Fig. 69.6 for the shifter currently under investigation at LLE, a birefringent wedge of KDP placed after the frequency-tripling crystals. The birefringence of KDP separates the laser beam into two orthogonal polarizations, which are deflected by the wedge through slightly different angles. (Alternatively, a liquid-crystal wedge could be used. Depending on the type of liquid crystal, the orthogonal polarizations could be linear or circular.) The two speckle patterns produced on target are spatially displaced, thus doubling the number of independent speckle patterns. The most effective way to use this technique is to disperse the polarization over a distance larger than the spectral dispersion produced by SSD. In this way, the polarization shift smoothes out modes of nonuniformity that are not smoothed by SSD, and overlap between the two techniques is avoided.[5] The reduction

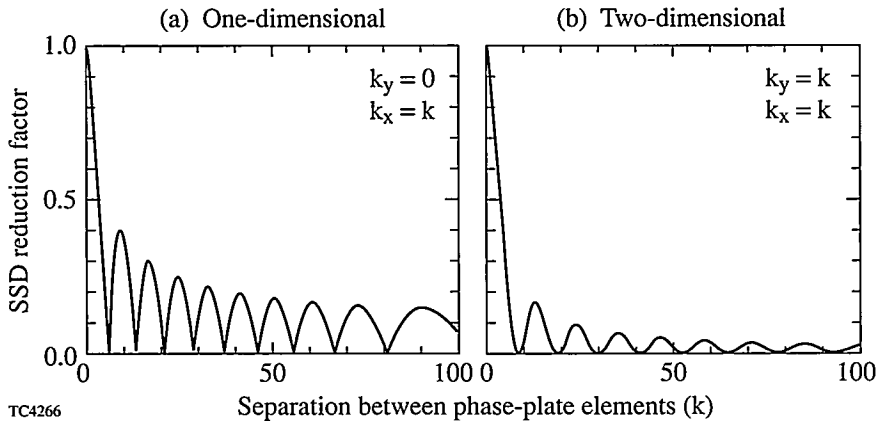

Figure 69.5
The absolute value of the 2-D SSD reduction factor as a function of nonuniformity wave vector (or equivalently the separation k between phase-plate elements). (a) The wave vector is along one of the dispersion directions. The reduction is the same as for 1-D SSD. (b) The wave vector is at 45°, resulting in the maximum 2-D reduction.

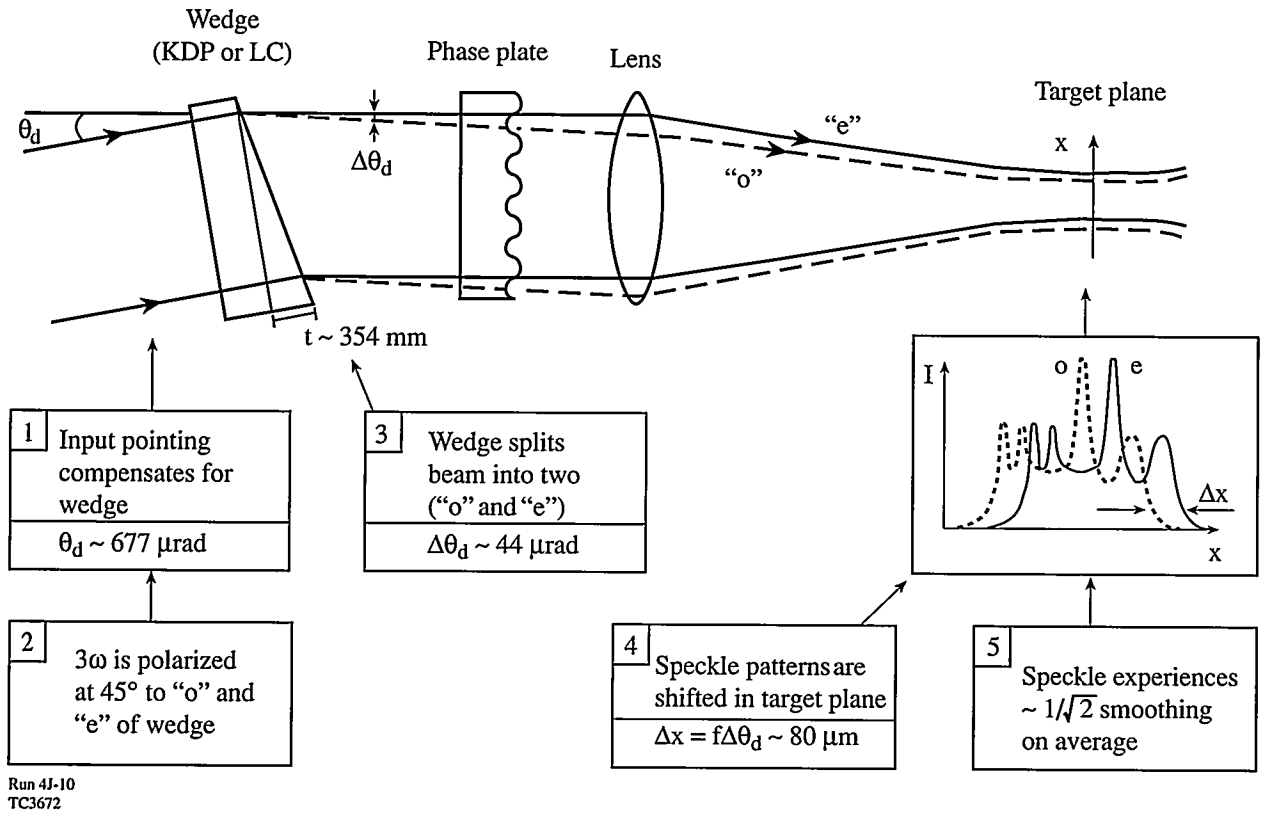

Figure 69.6
Principle of the (birefringent) polarization wedge. The laser beam is split equally into two orthogonal polarizations ("*o*" and "*e*"), which are deflected by the wedge through slightly different angles. This results in two spatially displaced speckle patterns in the target plane with orthogonal polarizations, which add in intensity rather than electric field, providing an instantaneous reduction of $1/\sqrt{2}$ in the rms nonuniformity.

in nonuniformity resulting from the polarization shifter is instantaneous because there is no interference between the two polarizations.

The predicted improvement in uniformity produced by 2-D SSD on OMEGA is shown in Fig. 69.7 as a function of the smoothing time. The results are for multiple overlapping beams on a spherical target and thus include the smoothing effect of overlapping beams. Two cases are presented. One shows the results for the current implementation of 2-D SSD in which 1.5 Å of bandwidth is dispersed in each direction. The second case shows the result of doubling the bandwidth in one direction and adding polarization dispersion in the second. This case achieves the uniformity goal of OMEGA, namely reaching the 1%–2% rms level within a smoothing time of less than 500 ps.

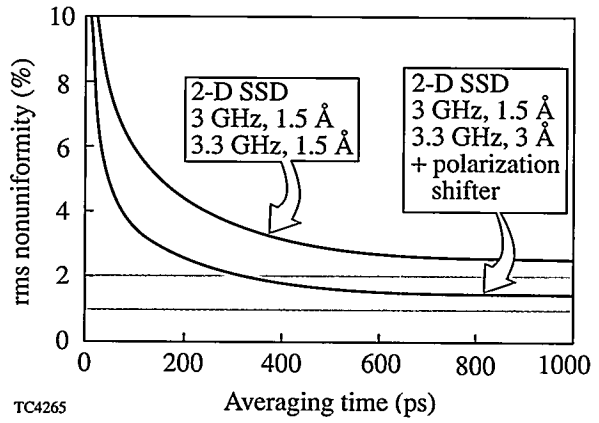

Figure 69.7
Reduction in rms nonuniformity as a function of smoothing time for multiple beam overlap on a spherical target, using the 60-beam OMEGA geometry. Spherical harmonic modes up to $\ell = 500$ have been considered with no additional smoothing assumed in the plasma atmosphere around the target. The lower curve corresponds to a higher bandwidth in one direction and the inclusion of polarization shifters.

Implementation of 2-D SSD

2-D SSD was implemented on OMEGA in January 1996. An aggressive optical design program showed that 2-D SSD

could be implemented over roughly the same time interval that was originally planned for 1-D SSD. However, it was important to adopt a conservative strategy with regard to bandwidth during the time that the operating characteristics of the new laser and SSD were being studied, because spectrally dispersed bandwidth can introduce intensity fluctuations that can damage laser optical components. As such, the initial implementation of 2-D SSD used bandwidths of only 1.5 Å and 0.75 Å. The initial results presented in this section were generated with these bandwidths. The bandwidth has recently been increased to 1.5 Å in each direction. To accommodate the increased dispersion of the beam, it has been necessary to enlarge one spatial-filter pinhole in the driver and to enlarge the second SSD modulator crystal. Future plans call for an increase in pinhole diameters later in the laser chain to allow the propagation of up to 3 Å of bandwidth.

A far-field image of the beam, after the final set of gratings, is shown in Fig. 69.8. Although the individual spectral components can not be seen in this figure, the two-dimensional dispersion is clearly evident. The extremes of the spectrum are the most intense portions for sinusoidal phase modulation. This is seen in the corners of the figure. The two directions of dispersion are not exactly orthogonal due to a 6° misalignment of the periscope that takes the beam out of the pulse generation room (PGR), but this has no effect on the irradiation uniformity on target. The amount of dispersion in each direction is proportional to the bandwidth from each modulator.

Images of the final beam profile,[6] in an equivalent target plane (ETP), are shown in Fig. 69.9. These images are for a single beam profile and therefore take no account of the additional smoothing achieved by beam overlap. The first image [Fig. 69.9(a)] shows the frequency-tripled beam without a phase plate or SSD. The intensity nonuniformity is the result of phase aberrations that have accumulated throughout the laser chain. Figure 69.9(b) shows the improvement produced by a phase plate. A well-defined intensity envelope has been established, but superposed on the envelope is highly modulated speckle. Figure 69.9(c) shows smoothing of the speckle by 1-D SSD, for which the bandwidth is turned on in one modulator and off in the other. Both combinations are shown. The "stripes" in the images show the direction of spectral dispersion. Nonuniformity perpendicular to the dispersion is not smoothed. Finally, the last image [Fig. 69.9(d)] shows the improved smoothing produced by two-dimensional dispersion. Note that the "stripes" have now been eliminated.

These images were time integrated over the laser pulse. The uniformity achieved is characteristic of an SSD smoothing time roughly equal to the pulse width, which was ~1 ns for this experiment. The rms fluctuations of the intensity around smooth envelopes are listed in Table 69.I, which gives both the measured and theoretically predicted values. A large part of the improved uniformity for 2-D SSD compared with 1-D SSD (a factor of ~2) is related to the smoothing duration: 1-D SSD reaches an asymptotic level of uniformity after ~300 ps; 2-D SSD continues to smooth throughout the entire time of the pulse (1 ns). There is an increased bandwidth for 2-D SSD (due to contributions from both modulators), but this has a much smaller effect on the improved uniformity than the increased smoothing duration, for this example.

Very recently a prototype KDP polarization wedge has been tested on OMEGA. One-dimensional lineouts through equivalent-target-plane (ETP) images (Fig. 69.10) show that the predicted $\sqrt{2}$ uniformity improvement is indeed obtained.

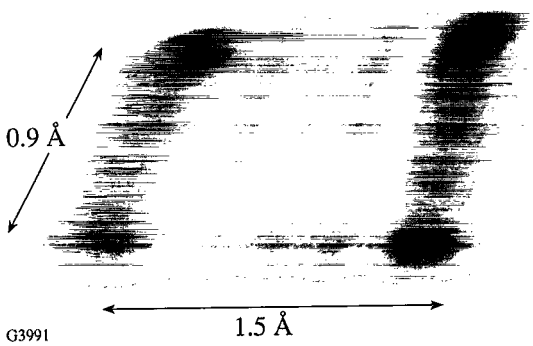

Figure 69.8
A far-field image of the beam (after the final diffraction gratings) showing that the two-dimensional dispersion of the beam is proportional to the bandwidth applied by each modulator.

Table 69.I: rms nonuniformity for the single-beam images in Fig. 69.9, compared with the theoretically predicted values (when averaged over the 1-ns pulse).

Image	Bandwidth (Å)	Measured rms	Calculated rms
(b)	0	0.96	0.98
(c)	0.75, 0	0.27	0.28
(c)	0, 1.5	0.24	0.21
(d)	0.75, 1.5	0.12	0.11

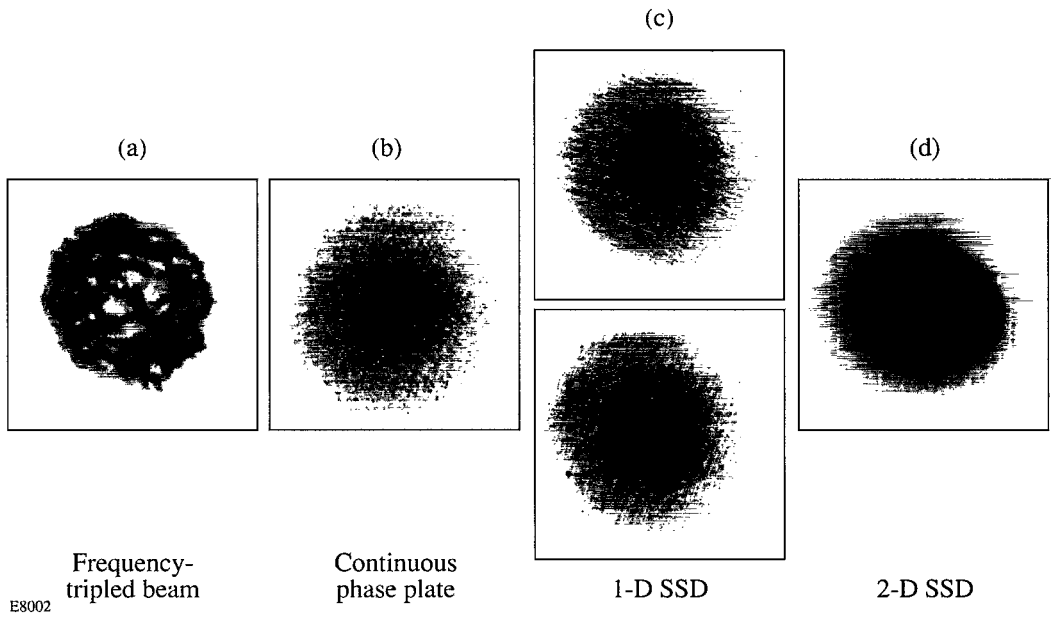

Figure 69.9
Equivalent-target-plane images, integrated over the ~1-ns pulse width, of a single OMEGA beam with four levels of smoothing: (a) unsmoothed, frequency-tripled; (b) phase plate, no bandwidth; (c) bandwidth in only one modulator; (d) bandwidth in both modulators.

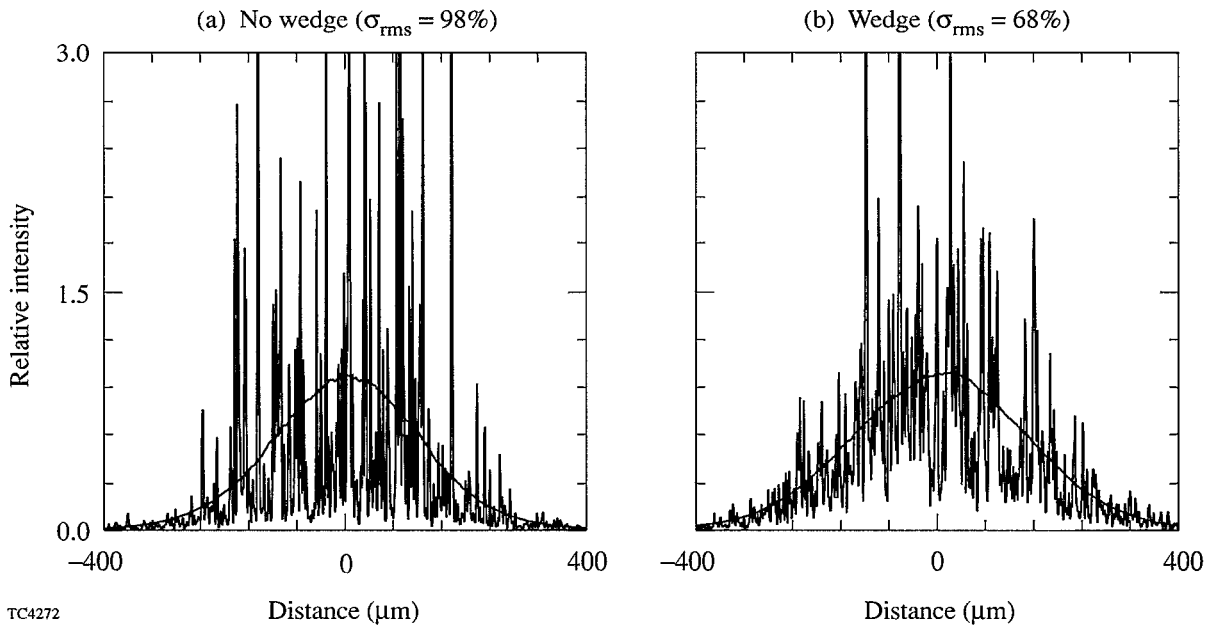

Figure 69.10
One-dimensional lineouts of the ETP images on OMEGA produced (a) without a polarization wedge and (b) with a polarization wedge. The measured rms nonuniformities of σ_{rms} = 98% and 68%, respectively, demonstrate the predicted $\sqrt{2}$ uniformity improvement made possible by the wedge.

ACKNOWLEDGMENT

This work was supported by the U.S. Department of Energy Office of Inertial Confinement Fusion under Cooperative Agreement No. DE-FC03-92SF19460, the University of Rochester, and the New York State Energy Research and Development Authority. The support of DOE does not constitute an endorsement by DOE of the views expressed in this article.

REFERENCES

1. S. Skupsky, R. W. Short, T. Kessler, R. S. Craxton, S. Letzring, and J. M. Soures, J. Appl. Phys. **66**, 3456 (1989).

2. Laboratory for Laser Energetics LLE Review **45**, NTIS document No. DOE/DP40200-149, 1990 (unpublished), p. 1

3. T. J. Kessler, Y. Lin, J. J. Armstrong, and B. Velazquez, in *Laser Coherence Control: Technology and Applications*, edited by H. T. Powell and T. J. Kessler (SPIE, Bellingham, WA, 1993), Vol. 1870, p. 95.

4. Y. Lin, T. J. Kessler, and G. N. Lawrence, Opt. Lett. **20**, 864 (1995).

5. R. S. Craxton and S. Skupsky, Bull. Am. Phys. Soc. **40**, 1826 (1995).

6. T. R. Boehly, R. L. Keck, C. Kellogg, J. H. Kelly, T. J. Kessler, J. P. Knauer, Y. Lin, D. D. Meyerhofer, W. Seka, S. Skupsky, V. A. Smalyuk, S. F. B. Morse, and J. M. Soures, presented at the *Second Annual International Conference on Solid State Lasers for Application to Inertial Confinement Fusion* (ICF), Paris, France, 22–25 October 1996.

Areal Density Measurement of Laser Targets Using Absorption Lines

Absorption lines due to $1s$–$2p$ transitions in titanium ions are predicted to be observed in the implosion of titanium-doped shells. The measured absorption of these lines can be used to determine the peak areal density $\rho\Delta r$ of the doped layer and hence of the total compressed shell. The absorption lines are studied by solving the radiation transport equation using opacity tables and hydrodynamic simulations. The absorption is a function not only of $\rho\Delta r$ but also of the density and temperature of the absorbing layer. However, it is shown that the areal density can be estimated with reasonable accuracy by using the measured intensity of absorption and its distribution over the various absorption lines. The considerations affecting the choice of doping parameters are discussed, as well as the effect of integrating the measured spectrum over time and target volume.

Recently published work[1] showed that a titanium-doped layer within a polymer shell of a laser-imploded target can yield information on core-shell mixing. We show here that the absorption lines predicted to be produced by such a doping provide a signature of shell areal density ($\rho\Delta r$) at peak compression. This areal density is an important parameter characterizing the implosion performance, which in turn is determined by target instability and mixing.

In the work on mixing diagnostics,[1] the doped-layer location within the shell was removed from the fuel-shell interface so that, in the absence of mixing, only titanium absorption lines would be observed, but mixing could cause titanium material to move into inner target regions and emit titanium lines. Even for the assumed level of mixing, *the absorption lines were essentially unchanged from the no-mixing case.* Thus, such a doped layer can provide information on the overall $\rho\Delta r$ of the compressed (or overdense) shell, even if its inner part undergoes mixing. The doped layer is placed in the target far from the interface but still close enough not to be ablated away.

Measurement of the absorption spectrum yields the areal density of only the doped layer.[2] This by itself is of interest because the comparison of measured and predicted $\rho\Delta r$ for the doped layer is a measure of target performance. Additionally, the total areal density of the compressed shell can be deduced if the thickness of target layer that is ablated away is measured (e.g., by charge collectors).

The absorption lines are studied by solving the radiation transport equation using OPLIB[3] opacity tables and one-dimensional *LILAC*[4] hydrodynamic simulations. The absorption is a function not only of $\rho\Delta r$ but also of the density and temperature of the absorbing layer. However, it is shown that the areal density can be estimated with reasonable accuracy by using the measured intensity of absorption and its distribution over the various absorption lines. The initial $\rho\Delta r$ of the titanium doping must be small enough, or the effect of local emission in the absorption region will lead to underestimating the $\rho\Delta r$. It is further shown that integrating the measured spectrum over the target volume causes only a small error, while integrating over time causes the $\rho\Delta r$ to be underestimated by about a factor of 2.

Modeling a Test Case

We calculate the expected x-ray spectrum of a particular simulated target implosion on the OMEGA laser. For this test case, *LILAC* results were used for the expected temperature (T) and density (ρ) profiles, and a post-processor[5] code was used to calculate the emission and radiation transport through the target. To simulate the emergent absorption and emission spectrum, multigroup opacity tables were generated using the OPLIB opacity library.[3]

The target is a polymer shell of 940-μm diam and 30-μm thickness, filled with 80 atm DT gas. A layer doped with 1% titanium (by atom number) is embedded in a CH polymer shell; the doped layer is placed 2.4 μm from the interface and its thickness is varied. As explained in earlier work,[1] such a doped layer shows significant absorption at the wavelengths of titanium lines, while showing little effect on overall target behavior. The laser pulse is trapezoidal, rising linearly over a 0.1-ns period to 13.5 TW, then remaining constant for 2.2 ns, before dropping linearly over a 0.1-ns period. *LILAC* hydrody-

namic simulations show[1] that the shell compresses to a mean radius of ~50 μm and thickness of ~30 μm, with a density in the range of ~10 to 50 g/cm^3, corresponding to a $\rho\Delta r$ value of ~90 mg/cm^2. The electron temperature in the shell ranges from ~800 (at the shell-fuel interface) to ~80 eV (at the peak of the shell density); the line absorption occurs within the colder, outer part of this compressed shell. The profiles at maximum compression are shown in Fig. 69.11.

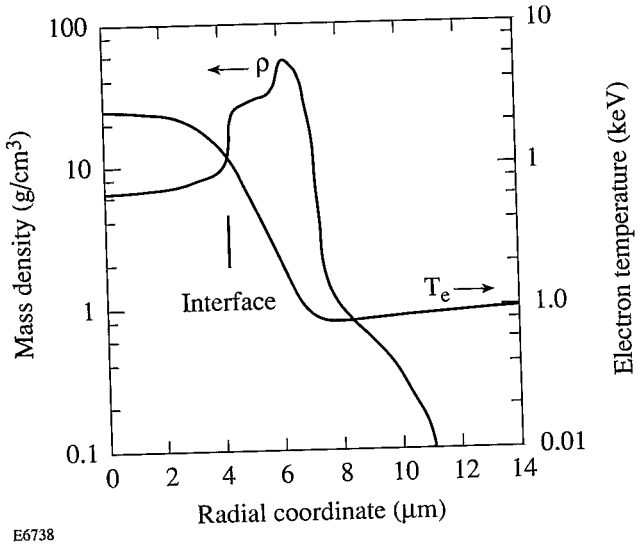

Figure 69.11
The density and temperature profiles predicted by the *LILAC* hydrodynamics simulation code at peak compression.

Figure 69.12 shows examples of the predicted spectrum at two instances during the implosion, showing titanium absorption lines. The time 2.9 ns corresponds to peak compression. These lines correspond to transitions of the type $1s$–$2p$ in titanium ions of an incomplete L shell: Ti^{+13} to Ti^{+20}. The designation Li in Fig. 69.12 stands for lithium-like titanium ion, and likewise for the other designations. Each peak contains several lines that are unresolved mostly because of broadening due to the finite source size. For example, the peak marked C (carbon-like) consists of 35 transitions of the type $1s^22s^22p^2$–$1s2s^22p^3$. On approaching peak compression, the intensity of the continuum radiation is seen to rise sharply and the absorption-line manifold is seen to shift to higher ionization states. This shift, caused by the increase in shell temperature as the shell becomes more compressed, is discussed further below.

The absorption lines are formed when radiation emitted by the compressed core traverses colder shell layers. By the definition of the opacity k, the intensity within an absorption

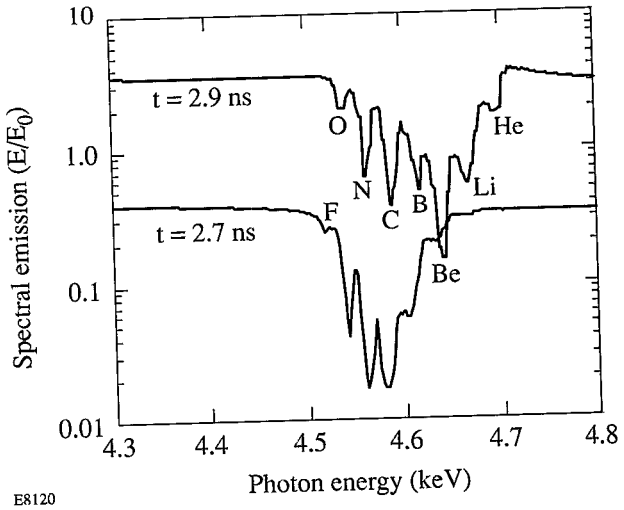

Figure 69.12
The predicted spectrum emitted by the test case (1%-titanium-doped layer) at two times during the implosion; $E_0 = 7 \times 10^{15}$ keV/(keV ns Ω). The time 2.9 ns corresponds to peak compression. The designation Li stands for the lithium-like titanium ion, and likewise for the other designations. The emission is integrated over the target volume.

line at an energy E is given by

$$I(E) = I_0(E)\,\exp\left[-\int k(E)\rho dr\right], \qquad (1)$$

where I_0 is the core-emitted intensity and $k(E)$ is the opacity per unit areal density. Equation (1) assumes that the local emission within the absorption region is neglected; this point is discussed further below. From Eq. (1) it follows that the $\rho\Delta r$ of the absorbing layer can be deduced from the measured spectrum through the relationship $\rho\Delta r = \ln\left[I_0(E)/I(E)\right]/k(E)$. However, $k(E)$ depends also on the (unknown) temperature and density in the absorption layer. Note that the density dependence of the opacity is in addition to the explicit dependence of the attenuation on $\rho\Delta r$ [Eq. (1)]. Next we examine these dependencies and show how Eq. (1) can be used to estimate the $\rho\Delta r$ of the absorbing layer, even without an exact knowledge of the temperature and the density.

Areal Density Determination Using Absorption Lines

Figures 69.13 and 69.14 show examples from OPLIB[3] of the opacity spectrum for 1% titanium in CH, as a function of temperature and density. As seen, 1%-titanium doping provides an ample contrast ratio between line absorption by titanium ions and the nonresonant absorption by both titanium

and CH. As the temperature increases (Fig. 69.13), the absorption-line manifold shifts to higher photon energies, or higher ionizations. The shift seen in Fig. 69.12 is similarly due to an increase in shell temperature on approaching peak compression. On the other hand, Fig. 69.14 shows that for the same temperature, a higher density causes the manifold to shift to lower ionizations. This is because the three-body (or collisional) recombination increases with increasing density faster than the two-body collision processes. The three-body recombination is important only at or near LTE (local thermodynamic equilibrium),[6] which is the atomic model used to generate the OPLIB tables. However, it can be shown[7] that for the ions and temperatures under consideration, the LTE approximation for the distribution of ion populations holds for densities (of the mostly polymer material) higher than ~6 g/cm^3; much higher shell densities than this are predicted for the test case. From Fig. 69.13 a doubling of the temperature leads to a 0.05-keV shift in the peak absorption. A similar shift in peak absorption requires, from Fig. 69.14, a factor-of-10 increase in density. Thus the peak positions are more sensitive to changes in temperature than in density. Figures 69.13 and 69.14 clearly show that the absorption at any given photon energy depends on both the temperature and the density; consequently, Eq. (1) cannot be used in a simple way to derive $\rho\Delta r$. In addition it should be noted that (1) changes in temperature and density cause primarily an energy shift in the absorption lines and (2) the total absorption-line manifold has only a weak dependence on temperature and density. Thus we choose the integral $\int \ln[I_0(E)/I(E)]dE$ over the whole absorption-line manifold as the experimental signature. We refer to the integral $\int \ln(I_0/I)dE$ as the area within the absorption lines [if film density is proportional to $\ln(I)$, this indeed is the area under the absorption lines on film]. From Eq. (1) we obtain

$$\int \ln[I_0(E)/I(E)]dE = \rho\Delta r \int k(E)dE. \qquad (2)$$

The opacity integral on the right can be obtained from opacity spectra such as those in Figs. 69.13 and 69.14. It turns out that even after integrating the opacity over the absorption-line manifold, the opacity still depends appreciably on temperature and density. For example, the opacity varies from 35 to 85 cm^2 keV/g when the temperature is varied from 0.3 to 10 keV and the density is varied from 1 to 50 g/cm^3. However, in addition to the integral over the spectrum we can also make use of the measured distribution among the absorption peaks. More specifically, the peak of strongest absorption provides an additional signature that also depends on both temperature and density and helps to narrow the range of opacity values.

To make use of this additional information, we calculated the integrated opacity for temperatures in the range of 0.3 to 1.0 keV and densities in the range of 1 to 50 g/cm^3. Fig-

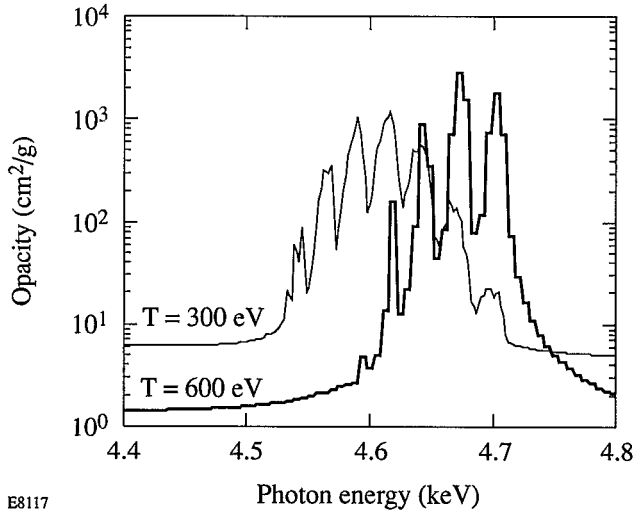

Figure 69.13
The opacity of 1%-titanium-doped CH at a density of 3.2 g/cm^3 (from OPLIB[3]), showing a shift to higher photon energies (higher ionizations) with increasing temperature. The absorption lines are due to $1s$–$2p$ transitions in titanium ions with increasing number of L-shell vacancies.

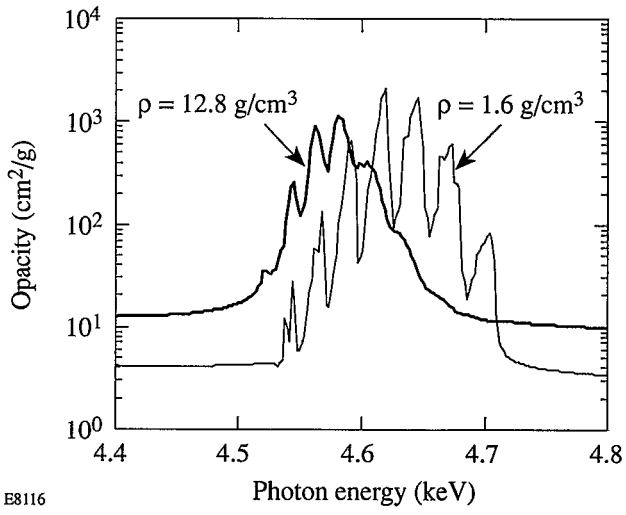

Figure 69.14
The opacity of 1%-titanium-doped CH at a temperature of 300 eV, showing a shift to lower photon energies (lower ionizations) with increasing density.

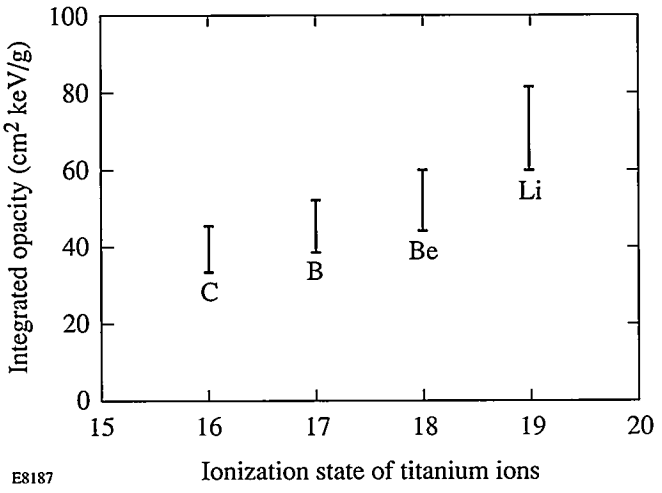

Figure 69.15
Area under the opacity-spectrum peaks, such as those in Figs. 69.13 and 69.14. For temperatures in the range of 300 to 1000 eV and densities in the range of 1 to 50 g/cm^3, the points are grouped according to the strongest absorption peak in the opacity spectrum (Li stands for cases where the lithium-like peak is the strongest, and likewise for the other designations).

ure 69.15 shows the results, arranged according to the strongest opacity peak (marked Li for cases where the lithium-like peak is the strongest, etc.). The four charge states (C-like to Li-like) cover the range likely to be encountered in target implosions. Figure 69.15 shows that knowing the peak of maximum absorption (without knowing the temperature or the density) narrows down the range of integrated opacity from ±42% to within ±15%.

To apply Fig. 69.15 to an experimental result, we first note the peak of maximum absorption in the spectrum. For example, if the Be-like peak dominates, we obtain from Fig. 69.15 the value 52 for the integrated opacity $\int k(E)dE$, *without having to know the temperature or the density*. Substituting this value in Eq. (2) produces a relation between the $\rho\Delta r$ of the doped layer and the measured area within the absorption lines (the integral on the left side of the equation). The error in determining $\rho\Delta r$ based of Fig. 69.15 is ±15%; other sources of error are discussed below.

Using the area under the absorption lines rather than the intensity profiles obviates the need to know the line profiles (e.g., due to Doppler and Stark effects). However, the measured and calculated intensity profiles should actually be quite similar because the absorption profile for each ion specie is comprised of many closely spaced components. In the experiment these components are smeared by the source-size broadening, whereas in the OPLIB[3] calculations they are smeared by the energy bin width, chosen to be similar to the source-size broadening. The final absorption profile for each ion specie is the envelope over these components and depends mostly on their relative intensity and separation.

Application of the Method to a Simulated Implosion

To test the method of determining $\rho\Delta r$ by the spectrum of absorption lines we apply it to a simulated spectrum from the implosion of the test case and compare the resulting $\rho\Delta r$ to the actual $\rho\Delta r$ of the profiles used in the calculation of the spectrum. This procedure simulates the application of the method to an experimentally observed spectrum.

Figure 69.16 shows two examples of the calculated emergent spectrum for the test case. For very high opacities, the attenuation in the emergent lines cannot be arbitrarily high because local emission within the absorption region fills in the absorption dips. Therefore, the doped layer must be sufficiently thin, or the $\rho\Delta r$ will be underestimated. Similarly, the depth of the observed absorption lines is limited by the finite dynamic range of the film (or other detector). To demonstrate the effect of self-absorption, we show in Fig. 69.16 a comparison of the spectra emitted from two identical titanium-doped targets except for the thickness of the doped layer, which was

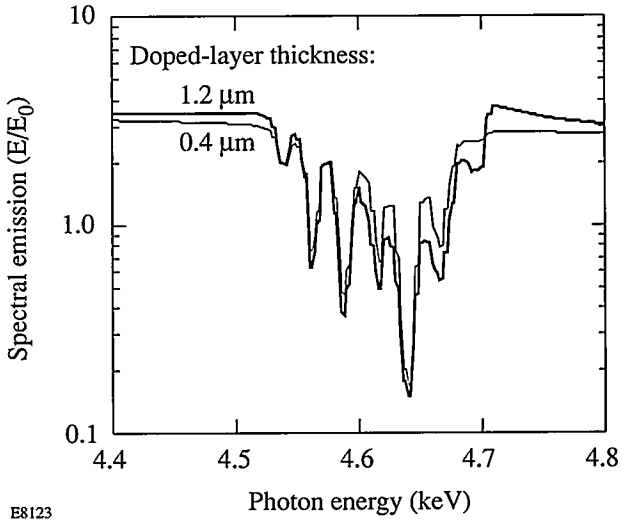

Figure 69.16
Comparison of the spectrum emitted from two identical 1%-titanium-doped targets except for the thickness of the doped layer, which was 0.4 and 1.2 μm, respectively. Both spectra refer to the time of peak compression and are integrated over the target volume; $E_0 = 7 \times 10^{15}$ keV/(keV ns Ω). The near coincidence of the two spectra is caused by the local emission in the absorption region.

0.4 and 1.2 μm, respectively. We refer to these two target simulations as the "thin case" and the "thick case." The separation of the outer surface of the doped layer from the shell-fill interface was 2.4 μm in both cases (the thick case's inner boundary was closer to the shell-fill interface than the thin case's). Both spectra refer to the time of peak compression and are integrated over the target volume. The similarity of the two spectra is clear evidence of local emission in the absorption region. Thus, at the wavelengths of highest absorption, only radiation emitted on the outer surface of the doped layer can emerge, and its intensity is independent of the thickness of the doped layer. On the other hand, for the weak absorption peaks [where the attenuation factor $\ln(I_0/I)$ is smaller than ~1] we would expect the absorption depths to be proportional to the doped-layer thickness. The reason for the weaker changes evident in Fig. 69.16 is that the thin doped layer happens to sample the highest-absorbing part (higher ρ, lower T) of the doped region. Thus, a too-thick doped layer gives rise to difficulties due to both local emission and gradients in plasma parameters.

We now apply the method of determining the areal density to the two spectra in Fig. 69.16. The area $\int \ln(I_0/I)\,dE$ in Fig. 69.16 is equal to 0.17 keV for the thin case and 0.21 keV for the thick case. The strongest absorption peak is at 4.65 keV and corresponds to Be-like titanium. From Fig. 69.15 we use the average integrated opacity for the Be-like titanium, which has the value 52 cm^2 keV/g (with an error of ±15%). Substituting these values into Eq. (2) we finally obtain $\rho\Delta r$ = 3.2 mg/cm^2 for the thin case and $\rho\Delta r$ = 4.0 mg/cm^2 for the thick case. This is compared with *LILAC*'s $\rho\Delta r$ values at peak compression: $\rho\Delta r$ = 3.1 mg/cm^2 for the thin case and $\rho\Delta r$ = 13.5 mg/cm^2 for the thick case. Thus, the method works well for the thin case but significantly underestimates the $\rho\Delta r$ in the thick case because of local emission within the absorption region.

To obtain accurate $\rho\Delta R$ measurements from this technique the target doping must be such that $k\rho\Delta r < 1$, which can be achieved in two ways: The choice of target doping can be based on simulations, or one can start with high-$\rho\Delta r$ doping and repeat the experiment with successively lower doping levels until the measured absorption is seen to decrease with decreasing doping. The latter procedure is also desirable for the following reason: if the achieved $\rho\Delta r$ is smaller than predicted, the absorption lines may not be observed at all. Thus, starting with a thicker doped layer ensures the observation of absorption lines even in such a case. In the test case studied here, a 0.4-μm-thick layer doped at 1% was shown to be an appropriate final choice for doping.

The emergent spectrum from the simulated target has been shown in earlier publications.[1] However, that spectrum was computed for a spatially and temporally resolved measurement (axial view at peak compression). We show here the effect of integrating the calculated emergent spectrum over space and time. First, Fig. 69.17 shows a comparison of an axial-view spectrum (per unit area) with the space-integrated spectrum. The spectral intensity refers to the flux per unit area in units of $I_0 = 7 \times 10^{20}$ keV/(keV ns cm^2 Ω), whereas the emission refers to the flux from the whole target in units of $E_0 = 7 \times 10^{15}$ keV/(keV ns Ω). The ratio between the two curves is essentially equal to the inverse of the cross section of the emitting core (giving in Fig. 69.17 a core diameter of ~80 μm). The two spectra have very similar shapes, and the spatially integrated spectrum has an area $\int \ln(I_0/I)\,dE$ that is only ~15% smaller than that of the spatially resolved spectrum. This is not surprising since any ray from the core in the direction of observation traverses essentially the same shell thickness.

Figure 69.18 shows a comparison between the emergent spectrum at the time of peak compression (2.9 ns) and the time-integrated spectrum; both are integrated over the target volume. Note that the peak in absorption for the time-integrated spectra is not as clear cut as the peak for the time-resolved spectra. As

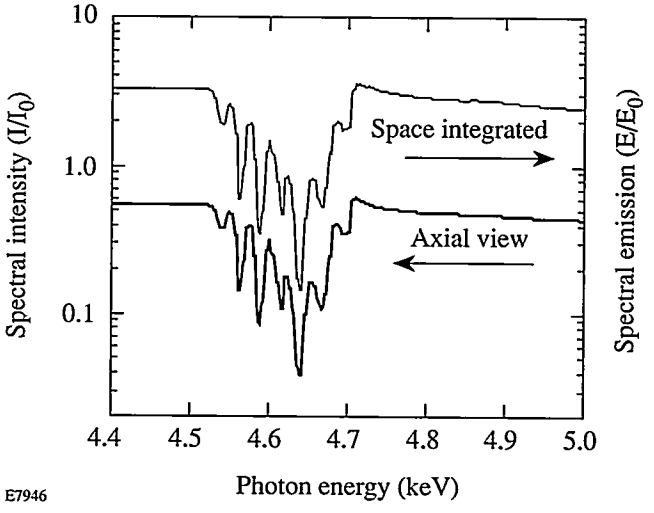

Figure 69.17
Comparison of simulated axial-view spectrum (per unit area) and space-integrated spectrum from an imploded, 1%-titanium-doped target. $I_0 = 7 \times 10^{20}$ keV/(keV ns cm^2 Ω); $E_0 = 7 \times 10^{15}$ keV/(keV ns Ω). The ratio between the two is essentially equal to the inverse of the cross section of the emitting core.

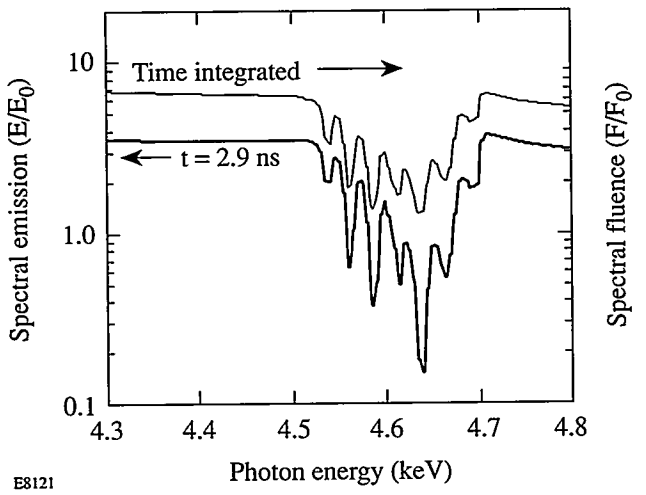

Figure 69.18
Comparison of simulated peak-compression and time-integrated spectra from an imploded, 1%-titanium-doped target (both are integrated over the target volume). $E_0 = 7 \times 10^{15}$ keV/(keV ns Ω); $F_0 = 2.3 \times 10^{15}$ keV/(keV Ω). The ratio between the two curves is essentially equal to the inverse of the core emission duration in nanoseconds.

the implosion progresses, the titanium dopant experiences an increase in temperature and density, and consequently there is a shift in the absorption peak with time. The time-integrated measurement averages over all these peaks. The emission, as in Fig. 69.17, is in units of $E_0 = 7 \times 10^{15}$ keV/(keV ns Ω) and the fluence is in units of $F_0 = 2.3 \times 10^{15}$ keV/(keV Ω). The ratio between the two curves is essentially equal to the inverse of the core emission duration in nanoseconds (Fig. 69.18 gives a duration of ~0.6 ns). The area $\int \ln(I_0/I)\,dE$ for the time-integrated spectrum is about half that of the peak-emission spectrum and using it would result in an underestimate of the $\rho\Delta r$ by the same factor.

As mentioned earlier, the total $\rho\Delta r$ of the compressed shell, $(\rho\Delta r)_{\text{total}}$, can be deduced from that of the doped layer, $(\rho\Delta r)_{\text{doped}}$, if the total ablated mass is measured (e.g., by charge collectors). A simple geometrical consideration shows that for a *uniformly compressed shell* the ratio

$$(\rho\Delta r)_{\text{doped}} / (\rho\Delta r)_{\text{total}}$$

is proportional to its initial value through a proportionality constant C, which depends on the spherical convergence and the location of the doped layer within the shell; C is smaller than, but close to 1. In the simulated test case the density of the compressed shell was constant to within ±30%. For that case, with an initial 30-μm-thick shell and a 0.4-μm-thick doped layer (the thin case), we deduced above a $\rho\Delta r$ for the doped layer of 3.2 mg/cm^2. The simulations by *LILAC* show that 16 μm of the shell thickness is unablated (this in an experiment will be deduced from charge collectors), so the total shell areal density at peak compression is estimated as $\rho\Delta r = 3.2 \times (16/0.4) = 128$ mg/cm^2. Here we assumed that the convergence is unknown and used $C = 1$. This result compares with *LILAC*'s value for peak compression of $\rho\Delta r = 110$ mg/cm^2. If the convergence is known (for example, from imaging), a better value of C can be used and the discrepancy reduced.

It might be thought that a thicker layer doped at a lower concentration could reduce the problem of relating the measured $\rho\Delta r$ to that of the total shell. However, this is undesirable because enlarging the doped layer results in averaging over the steep temperature gradient in the shell. This introduces an uncertainty in the choice of peak to be used in Fig. 69.15 and thus an additional error in the derived areal density.

Conclusion

An effective method has been described for measuring the areal density of the compressed (or overdense) shell of laser-imploded targets, based on the observation of absorption lines from a titanium-doped layer. Four factors have been shown to affect the precision of such measurement:

(a) If the initial $\rho\Delta r$ of the doped layer is too high, the problem of local emission in the absorption region will lead to an underestimate of the $\rho\Delta r$ at peak compression. To address this problem, the experiment can be repeated with progressively thinner doped layers (or lower doping concentrations), until the absorption is seen to decrease with decreasing $\rho\Delta r$ of the initial doped layer. This procedure is also desirable to ensure the observation of absorption lines even if the actual compression is smaller than predicted.

(b) If the spectrum is not streaked in time, the $\rho\Delta r$ will be grossly underestimated (typically by a factor of 2).

(c) If the spectrum is not spatially resolved, the $\rho\Delta r$ will be slightly underestimated (typically by ~15%). Thus, it is more important to resolve the spectrum in time than in space.

(d) The total ablated mass must first be determined (for example, by employing charge collectors) to be able to relate the measured $\rho\Delta r$ of the doped layer to the total $\rho\Delta r$ of the overdense shell.

ACKNOWLEDGMENT

This work was supported by the U.S. Department of Energy Office of Inertial Confinement Fusion under Cooperative Agreement No. DE-FC03-92SF19460, the University of Rochester, and the New York State Energy Research and Development Authority. The support of DOE does not constitute an endorsement by DOE of the views expressed in this article.

REFERENCES

1. B. Yaakobi, R. S. Craxton, R. Epstein, and Q. Su, J. Quant. Spectrosc. Radiat. Transfer **55**, 731 (1996).

2. A. Hauer, R. D. Cowan, B. Yaakobi, O. Barnouin, and R. Epstein, Phys. Rev. A **34**, 411 (1986).

3. M. F. Argo and W. F. Huebner, J. Quant. Spectrosc. Radiat. Transfer **16**, 1091 (1976).

4. E. Goldman, Laboratory for Laser Energetics Report No. 16, 1973 (unpublished); J. Delettrez and E. B. Goldman, Laboratory for Laser Energetics Report No. 36, 1976 (unpublished).

5. Laboratory for Laser Energetics LLE Review **58**, NTIS document No. DOE/SF/19460-17, 1994 (unpublished), p. 57.

6. H. R. Griem, *Plasma Spectroscopy* (McGraw-Hill, New York, 1964), Chap. 6.

7. *ibid.*, Eq. (6-60).

Modeling the Temporal-Pulse-Shape Dynamics of an Actively Stabilized Regenerative Amplifier for OMEGA Pulse-Shaping Applications

Advances in laser-fusion technology indicate that the temporal profile of the laser pulse applied to laser-fusion targets is important for improving the performance of these targets.[1] The OMEGA laser is a 60-beam laser-fusion system capable of producing a total of 30 kJ of ultraviolet (351-nm) energy on target, where the temporal profile of the optical pulse applied to a laser-fusion target can be specified in advance. This is accomplished by a pulse-shaping system that produces an optical pulse with a specific temporal pulse shape at the nanojoule energy level.[2] This pulse seeds an actively stabilized Nd:YLF regenerative amplifier[3] (regen) followed by and wavelength matched (1053 nm) to a series of Nd:glass amplifiers. The beams are then frequency tripled to the third harmonic using KDP nonlinear crystals. To achieve the desired on-target optical pulse shape, the temporal dynamics of the entire OMEGA laser system must be accurately modeled to determine the specific temporal profile of the seed pulse required from the pulse-shaping system at the beginning of the laser. The temporal profile of this low-energy seed pulse, when amplified and frequency tripled by the laser system, will then compensate for the temporal distortions caused by gain saturation in the regen and amplifiers and by the tripling process, and will produce the desired pulse shape on target.

To determine the required temporal profile of the optical pulse at the beginning of the system, all sources of temporal distortions in the system must be understood and compensated for. The temporal distortion due to the frequency-tripling process is modeled with a time-dependent simulation of the appropriate nonlinear equations for this process.[4] The temporal-pulse distortions in the system's Nd:glass amplifiers are easily modeled with our beam code *RAINBOW*. Modeling the actively stabilized Nd:YLF regen at the beginning of the system is the topic of this article. With the regen model described here, OMEGA's temporal dynamics can now be completely modeled. Pulse distortions in the system can be easily compensated for by proper choice of the seed temporal profile determined from the overall model.

The gain of the OMEGA system from the pulse-shaping modulator to the target is approximately 10^{14}; a gain of 10^7 in the actively stabilized regen is included in this overall gain. Modeling the actively stabilized regen is complicated by many factors. The regen must be treated as a multipass amplifier, the last few passes of which experience significant gain saturation in the Nd:YLF laser rod. The lifetime of the lower-laser-level manifold in Nd:YLF has been measured to be 21 ns,[5] and the round-trip time in the cavity is 26 ns. A Frantz-Nodvik–type solution[6] for the gain in the Nd:YLF medium cannot account for this finite lower-laser-level lifetime and, hence, is inappropriate; the rate equations must be used to describe the single-pass gain in the Nd:YLF medium. Finally, the regen incorporates a feedback mechanism that measures the circulating pulse energy each round-trip.[3] When the circulating pulse energy exceeds a threshold (~25 μJ), a feedback mechanism is activated. The feedback mechanism introduces appropriate losses into the cavity each round-trip in order to stabilize the circulating pulse energy to a fixed but low-energy level. During this prelase stabilization phase the regen is operating with a net gain (round-trip gain/loss) approximately equal to unity and establishes a constant and stable pulse-energy output from the regen. After this prelase stabilization is achieved, the laser can be Q-switched by eliminating the feedback losses from the cavity. The regen will then emit a Q-switched envelope of pulses. The pulse at the peak of the Q-switched envelope is switched out and sent to the OMEGA amplifiers. This stabilized regen produces pulses with a long-term shot-to-shot energy stability of approximately 0.2%, despite the fluctuations introduced by the flash-lamp pumping, and is insensitive to injected-pulse energy variations of more than two orders of magnitude.[3]

The regen is modeled by numerical integration of the rate equations and careful consideration of the regen dynamics. The regen model described here includes gain saturation in the Nd:YLF laser rod, intracavity losses, lower-laser-level lifetimes, and the active losses introduced by the stabilizer-feed-

back circuit. Careful measurements of the input and output shaped optical pulses from the regen have been made and will be discussed. The calculations on this regen agree well with the measured output of the regen and serve as a model for this important OMEGA component. With this regen model, the entire temporal-pulse-shaping dynamics of OMEGA can now be modeled from the pulse-shaping system to the final on-target pulse shape. This modeling provides us with the capability to accurately produce any desired temporally shaped optical pulse on target for laser-fusion experiments.

Rate Equations

OMEGA's pulse-shaping system produces a shaped optical pulse that is injected into the actively stabilized regenerative amplifier. The output-pulse shape of the regen is determined by gain saturation in the active medium and by the cavity dynamics. The regen model consists of injecting a temporally shaped pulse into the cavity and calculating the new shape after every pass through the cavity. The effect on the pulse shape due to each component is treated separately in the calculation. In this section we discuss the temporal distortion due to a single pass through the gain medium and in the next section incorporate this into the calculation of the overall regen dynamics.

Gain saturation due to a single pass through a gain medium is calculated by solving the laser rate equations[7]

$$\frac{\partial\varphi(z,t)}{\partial t}+\frac{c}{n}\frac{\partial\varphi(z,t)}{\partial z}=\frac{c\sigma\varphi(z,t)}{n}\left[f_2N_2(z,t)-f_1N_1(z,t)\right], \tag{1a}$$

$$\frac{\partial N_1(z,t)}{\partial t}=\frac{c\sigma\varphi(z,t)}{n}\left[f_2N_2(z,t)-f_1N_1(z,t)\right]+\frac{N_2(z,t)}{\tau_{21}}-\frac{N_1(z,t)}{\tau_{10}}, \tag{1b}$$

$$\frac{\partial N_2(z,t)}{\partial t}=-\frac{c\sigma\varphi(z,t)}{n}\times\left[f_2N_2(z,t)-f_1N_1(z,t)\right]-\frac{N_2(z,t)}{\tau_{21}}, \tag{1c}$$

which describe the evolution of the cavity photon flux φ, the atomic population N_1 of the lower laser manifold, and the atomic population N_2 of the upper laser manifold. These rate equations explicitly account for the lifetimes of these upper and lower laser manifolds. In these equations c is the speed of light in vacuum; n is the index of refraction of the gain medium; σ is the stimulated emission cross section (1.2×10^{-19} cm^2); and $\tau_{i,j}$ is the relaxation time of the transition from manifold i to manifold j (here, level 0 represents the ground state). The upper laser manifold N_2 consists of two sublevels labeled with energies $E_{2,n}$ ($n=1,2$), and the lower laser manifold N_1 consists of six sublevels labeled with energies $E_{1,m}$ ($m=1$ to 6), two of which are degenerate in energy (sublevels 2 and 3) as shown in Fig. 69.19. The stimulated emission terms in the rate equations [Eqs. (1)] (first terms on the right side in each equation) involve transitions between the sublevels E_{21} and E_{12} as shown in Fig. 69.19; hence, the thermal occupation f_iN_i of these laser-active sublevels is used in these terms. The thermal occupation of these sublevels is calculated by

$$f_1N_1=\frac{e^{-E_{12}/kT}N_1}{\sum_{m=1}^{m=6}e^{-E_{1m}/kT}}=0.207\ N_1 \tag{2a}$$

and

$$f_2N_2=\frac{e^{-E_{21}/kT}N_2}{e^{-E_{21}/kT}+e^{-E_{22}/kT}}=0.570\ N_2, \tag{2b}$$

where $E_{i,j}$ is the energy of level i sublevel j relative to the lowest

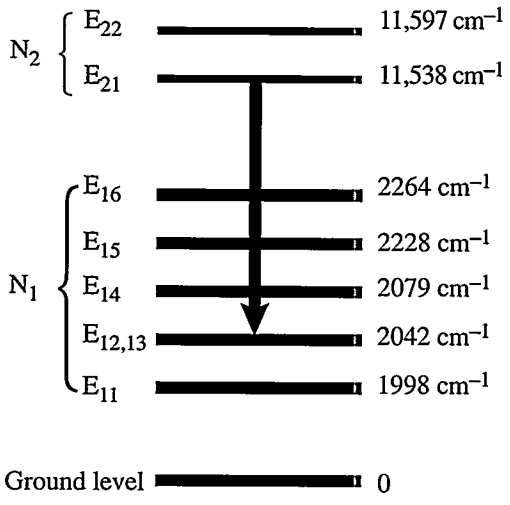

Figure 69.19
The energy levels involved in the 1.053-μm-Nd:YLF laser transition. The arrow shows the laser transition between sublevels within the manifolds shown.

energy level in the manifold, k is the Boltzman constant, and T is the temperature (assumed to be room temperature).

The rate equations [Eqs. (1)] can be solved numerically. We transform these equations along their characteristics in the time-distance plane with the transformation equations

$$x \rightarrow z + \frac{ct}{n} \qquad \tau \rightarrow t - \frac{nz}{c}. \tag{3}$$

If we use the chain rule and the substitution

$$\Delta N = \frac{\sigma\varphi(x)}{2}\left[f_2 N_2(z,t) - f_1 N_1(z,t)\right]dx \tag{4}$$

with $cdt/n = dz = dx/\sqrt{2}$, we get the set of finite-difference equations

$$d\varphi = \Delta N, \tag{5a}$$

$$dN_1 = \sqrt{2}\,\Delta N + \frac{N_2}{\tau_{21}}dt - \frac{N_1}{\tau_{10}}dt, \tag{5b}$$

$$dN_2 = -\sqrt{2}\,\Delta N - \frac{N_2}{\tau_{21}}dt \tag{5c}$$

for the transformed rate equations. Here we have transformed Eq. (1a) using the transformation equations [Eqs. (3)], and we have left Eqs. (1b) and (1c) untransformed since the photon flux evolves in both space and time, whereas the populations evolve in time only. These equations can be solved numerically given appropriate boundary conditions.

In the model, the photon flux is specified at the entrance face of the laser rod and is given by the temporal profile of the pulse entering the rod. The initial upper-laser-level population is determined from measurements of the laser rod small-signal gain, and for simplicity the initial lower-laser-level population is assumed to be zero. With these boundary conditions, Eqs. (5) can be numerically integrated to yield the photon flux at any time and for any position in the laser rod. Of interest for our calculations is the output-pulse shape specified at the output face of the laser rod. These equations with these boundary conditions, along with the regen dynamics discussed below, have been solved numerically, and the results are presented below.

Regenerative Amplifier Model

Modeling the regen consists of injecting a pulse with a given pulse shape and energy into the regen and calculating the new pulse shape and energy after each round-trip through the cavity. A single round-trip through the regenerative amplifier is depicted in Fig. 69.20. The pulse first experiences gain through the laser rod followed by propagation to the output-coupling mirror and back. The pulse then experiences gain again followed by propagation to the end mirror and back. Losses due to the output-coupling mirror and the feedback stabilizer (discussed below) are included in the calculation. During propagation of the pulse in the cavity, the upper- and lower-laser-level manifolds are allowed to decay with their respective lifetimes. This calculation for a single pass through the cavity gives the output-pulse shape and energy, given the input-pulse shape and energy for the pass. The output pulse for each pass is used as the input pulse for the next pass through the cavity, and the procedure is repeated for a given number of round-trips through the cavity.

The loss due to the feedback stabilizer depends on several factors. The cavity incorporates two Pockels cells, one of which is feedback controlled. Specific voltages are applied to all four electrodes of the two Pockels cells at specific times.[3] During the beginning of the flash-lamp cycle, high losses are introduced into the cavity to allow the gain to build up in the rod. At the peak of the gain, a pulse is injected into the cavity at time t_1, and all losses are removed from the cavity (with the exception of the static losses here assumed to be 55% in our laser, which includes the 50% output coupler loss) allowing the circulating-pulse energy to increase. The applied voltages after time t_1 are shown schematically in Fig. 69.21(a) (however, not to scale). When the circulating-pulse energy reaches a threshold value (adjusted to ~25 μJ), the feedback stabilizer is activated. At this time (t_2) a dc voltage V_{dc} is applied to one electrode of the first Pockels cell, which introduces a dc loss into the cavity. Simultaneously, a modulated feedback-con-

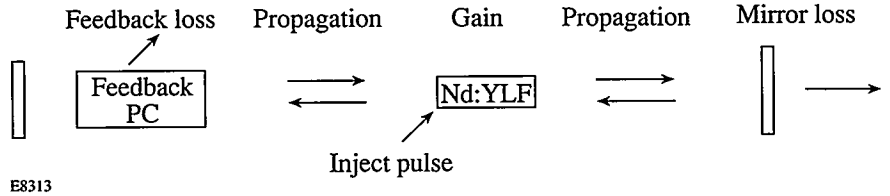

Figure 69.20
The regen model calculates the pulse shape and energy after a round-trip in the cavity, then iterates for many round-trips. The calculation includes the effects of gain saturation, propagation, and static and feedback losses.

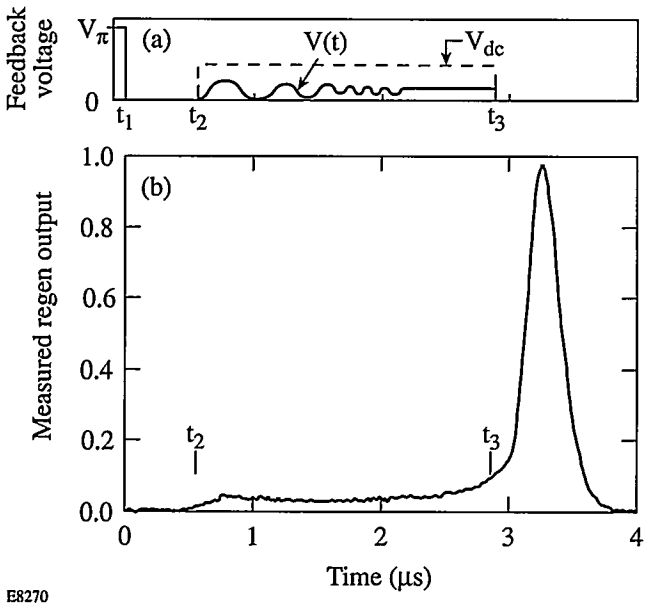

Figure 69.21
Regen temporal dynamics showing (a) feedback-controlled Pockels cell voltages (not to scale), and (b) measured regen-output envelope filtered to remove individual pulses in the train.

trolled voltage $V(t)$ is applied to an electrode of the feedback-controlled Pockels cell, which introduces a feedback-controlled modulated loss in the cavity. The function of the feedback-controlled modulated loss is to stabilize the circulating pulse energy to a specified constant low value. If the pulse energy falls below (above) this energy, loss is removed (added) to maintain the specified output-pulse energy. Specially designed circuitry for this modulated feedback-controlled voltage[3] eliminates pulse-shape distortions caused by fast feedback-voltage changes during pulse propagation through the Pockels cell, as in the previous design.[8] This ensures that pulse-shape distortions in the regen are due mainly to gain saturation. Finally, after the output-pulse energy is stabilized by the feedback mechanism during this prelase phase, the laser is Q-switched, at which time (t_3) all feedback loss is removed and a Q-switched pulse envelope is allowed to build up. (During this time an adjustable low-level dc loss is left in the cavity to control the final output-pulse energy; however, this loss is not included in the model.) The measured output-pulse train envelope from the regen is shown in Fig. 69.21(b).

The voltage applied to the feedback-controlled Pockels cell during the prelase stabilization is modulated every round-trip so that the Pockels cell transmission is given by

$$T = \cos^2\left(\frac{\pi}{2}\frac{V(t)}{V_\pi}\right), \tag{6}$$

where $V(t)$ is the instantaneous value of the modulated voltage difference between the electrodes and V_π is the quarter-wave voltage of the Pockels cell. The modulated voltage for a particular pass when the feedback circuitry is active is modeled by

$$V_{i+1} = \left[V_i + \Delta V_i\right] e^{-\tau_{rt}/\tau_{fb}}, \tag{7}$$

where V_i is the value of the modulated voltage at the beginning of the pass, ΔV_i is the increase in voltage due to the feedback circuitry, and V_{i+1} is the value of the modulated voltage after the pass. The change in voltage ΔV_i is given by

$$\Delta V_i = \text{pulse energy (J)} \times \text{feedback gain (V/J)}, \tag{8}$$

where the feedback gain is determined by the feedback circuitry. In Eq. (7), the final voltage is allowed to decay every round-trip (round-trip time $\tau_{rt} = 26$ ns) with the exponentially decreasing feedback decay time $\tau_{fb} = 35$ ns. When the laser is Q-switched at time t_3, all feedback loss is removed from the cavity allowing the free buildup of the Q-switched pulse train.

The above model describes how to calculate the output-pulse shape from the regen given the input-pulse shape. Often it is necessary to calculate the inverse, that is, calculate the required input-pulse shape to the regen that will produce a desired output-pulse shape. A good approximation for this input-pulse shape can be gotten from the output-pulse shape with a simple procedure. A transfer function for the regen can be calculated by using the desired regen-output-pulse shape $\left[I^{out}(t)\right]$ as input to the calculation to obtain a new output-pulse shape $\left[\text{e.g., } I^{new}(t)\right]$. The transfer function $T(t)$ for the regen is obtained by dividing these two functions to get

$$T(t) = \frac{I^{new}(t)}{I^{out}(t)}. \tag{9}$$

The required input-pulse shape $\left[I^{in}(t)\right]$ can now be calculated with this transfer function and is given by

$$I^{in}(t) = \frac{I^{out}(t)}{T(t)}. \tag{10}$$

This simple procedure is used to obtain the required regen-input-pulse shape that will produce the desired regen-output-pulse shape. More importantly, this procedure is useful in producing the desired OMEGA on-target pulse shape.

Experiments

The regen in OMEGA uses a Nd:YLF laser rod pumped to a single-pass, small-signal gain of approximately 2.9. The laser uses a 50% reflecting output coupler, the cavity-round-trip time is 26 ns, and the laser operates at 5 Hz. Typical output energies of the pulse switched out at the peak of the Q-switched envelope are approximately 1.0 mJ.

The measured output-pulse train from the regen is shown in Fig. 69.21(b). The output has been filtered to show only the envelope of the pulse-train output from the regen. It can be seen that the feedback is activated at time t_2 approximately 600 ns after the pulse is injected into the cavity at time $t_1 = 0$. At $t_3 = 2.9$ μs, the laser is Q-switched and a pulse train builds up and decays as the gain is depleted.

Figure 69.22 shows the calculated-output-pulse train from the regen for the above case. Individual pulses within the train are shown. The calculation is based on the model described above with typical values for the regen parameters. Note the good agreement between the measured-output-pulse train in Fig. 69.21(b) and the predictions shown in Fig. 69.22.

Figure 69.23 shows regen input/output-pulse shapes for a square pulse injected into the regen. The output-pulse shape is the pulse that is switched out at the peak of the Q-switched envelope. The input square pulse (curve plotted with long dashed lines) and measured-regen-output pulse (curve plotted with short dashed lines) are shown in Fig. 69.23, along with the calculated-output-pulse shape (curve plotted with solid line) obtained with the above numerical method using the measured-square-pulse shape as input to the calculation. The regen parameters used in the calculation correspond to the measured regen parameters with slight adjustments to obtain good agreement with the data. By adjusting the regen parameters in this way, the model is calibrated to the data. Once this calibration procedure is performed, the parameters in the model are left unchanged and other shaped pulses can be calculated and compared to measurements.

Figure 69.24 shows the same information as Fig. 69.23, but for a shaped optical pulse injected into the regen. The regen parameters were identical to those used for the calculation in Fig. 69.23. This pulse shape, when injected into OMEGA, will produce a square pulse shape at 351-nm wavelength at the output of OMEGA.

In summary, we have modeled the temporal evolution of a shaped optical pulse injected into our feedback-stabilized regen to a high degree of accuracy. We have solved the rate

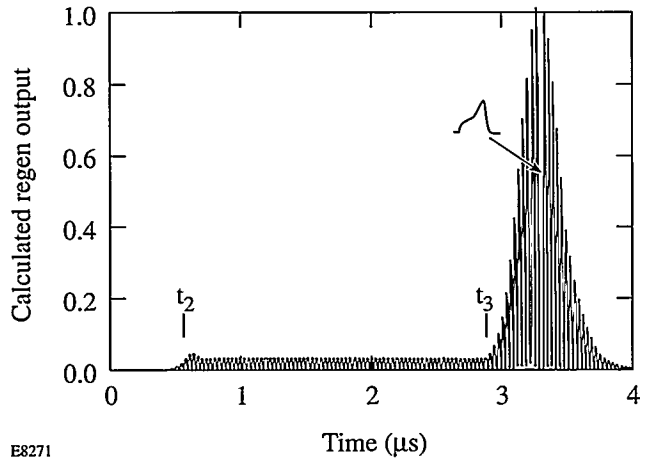

Figure 69.22
Calculated regen-output envelope corresponding to the case measured in Fig. 69.21(b). Individual pulses are shown.

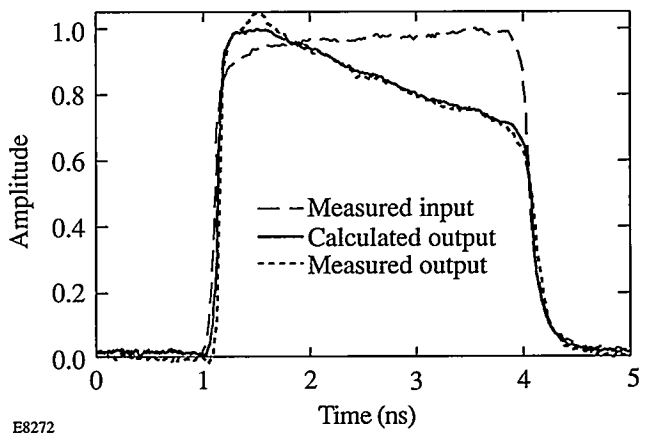

Figure 69.23
Square-pulse distortion from the regen showing the input-pulse shape (long dashed lines), the measured-output-pulse shape (short dashed lines), and the calculated-output-pulse shape (solid line).

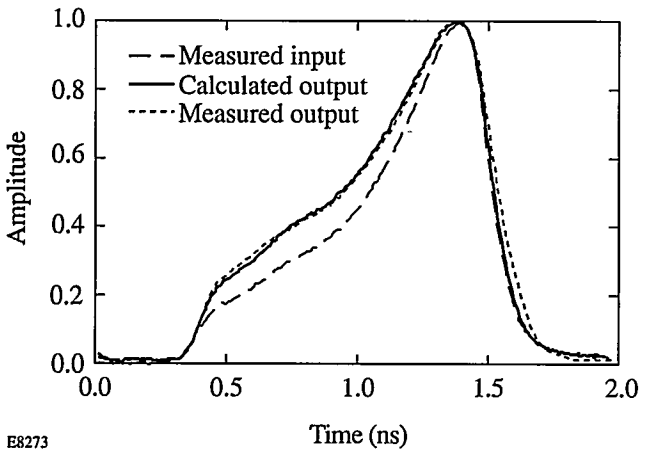

Figure 69.24
Shaped pulse from the regen showing the input-pulse shape (long dashed lines), the measured-output-pulse shape (short dashed lines), and the calculated-output-pulse shape (solid line).

equations including upper- and lower-laser-level lifetimes explicitly. We provide a prescription for determining the injection-pulse shape required to produce a given output-pulse shape from this regen. Finally, with this model of the regen, the entire OMEGA laser system can be modeled, and on-target pulse shapes can be specified in advance by OMEGA users.

ACKNOWLEDGMENT

This work was supported by the U.S. Department of Energy Office of Inertial Confinement Fusion under Cooperative Agreement No. DE-FC03-92SF19460, the University of Rochester, and the New York State Energy Research and Development Authority. The support of DOE does not constitute an endorsement by DOE of the views expressed in this article.

REFERENCES

1. J. D. Lindl, Phys. Plasmas 2, 3933 (1995).
2. A. Okishev, M. D. Skeldon, S. A. Letzring, W. R. Donaldson, A. Babushkin, and W. Seka, in *Superintense Laser Fields*, edited by A. A. Andreev and V. M. Gordienko (SPIE, Bellingham, WA, 1996), Vol. 2770, pp. 10–17.
3. A. Babushkin, W. Bittle, S. A. Letzring, A. Okishev, M. D. Skeldon, and W. Seka, "Stable, Reproducible, and Externally Synchronizable Regenerative Amplifier for Shaped Optical Pulses for the OMEGA Laser System," to be presented at Advanced Solid-State Lasers, Orlando, FL, 27–29 January 1997, paper ME9.
4. R. S. Craxton, IEEE J. Quantum Electron. **QE-17**, 1771 (1981).
5. J. D. Zuegel and W. Seka, IEEE J. Quantum Electron. **31**, 1742 (1995).
6. L. M. Frantz and J. S. Nodvik, J. Appl. Phys. **34**, 2346 (1963).
7. A. E. Siegman, *Lasers* (University Science Books, Mill Valley, CA, 1986).
8. A. Okishev, M. D. Skeldon, S. A. Letzring, W. Seka, and I. Will, in *OSA Proceedings on Advanced Solid-State Lasers*, edited by B. H. T. Chai and S. A. Payne (Optical Society of America, Washington, DC, 1995), Vol. 24, pp. 274–276.

Multiple Scale Derivation of the Relativistic Ponderomotive Force

The ponderomotive force associated with a light wave of variable amplitude[1–10] drives many phenomena that occur in inertial confinement fusion[11] and particle acceleration[12] experiments. The existing formula for the ponderomotive force was derived under the assumption that the quiver speed of electrons oscillating in the applied electric field is much less than the speed of light. With the advent of intense laser pulses,[13] it is important to extend this formula to electron quiver speeds that are comparable to the speed of light.

As an introduction to this subject, we review the derivation of the ponderomotive term in the electron-fluid momentum equation. The standard form of this equation is

$$\left(\partial_t + \mathbf{v}\cdot\nabla\right)(\gamma\,\mathbf{v}) = -(\mathbf{E} + \mathbf{v}\times\mathbf{B}), \tag{1}$$

where

$$\gamma = \left(1 - v^2\right)^{-1/2} \tag{2}$$

is the Lorentz factor associated with the fluid velocity and

$$\mathbf{E} = -\partial_t\mathbf{A}, \quad \mathbf{B} = \nabla\times\mathbf{A} \tag{3}$$

in the radiation gauge. These differ from the usual equations in that $\omega t \to t$, $k\mathbf{x} \to \mathbf{x}$, $\mathbf{v}/c \to \mathbf{v}$, $e\mathbf{E}/m\omega c \to \mathbf{E}$, $e\mathbf{B}/m\omega c \to \mathbf{B}$, and $e\mathbf{A}/mc^2 \to \mathbf{A}$.

By using the vector identity[14]

$$(\mathbf{v}\cdot\nabla)(\gamma\mathbf{v}) = \nabla\gamma - \mathbf{v}\times\left[\nabla\times(\gamma\mathbf{v})\right], \tag{4}$$

one can rewrite the momentum equation as

$$\partial_t(\gamma\,\mathbf{v} - \mathbf{A}) = \mathbf{v}\times\left[\nabla\times(\gamma\,\mathbf{v} - \mathbf{A})\right] - \nabla\gamma, \tag{5}$$

from which follows the relativistic vorticity equation

$$\partial_t\left[\nabla\times(\gamma\,\mathbf{v} - \mathbf{A})\right] = \nabla\times\left\{\mathbf{v}\times\left[\nabla\times(\gamma\,\mathbf{v} - \mathbf{A})\right]\right\}. \tag{6}$$

For a plasma that is at rest before the laser pulse arrives, $\nabla\times(\gamma\,\mathbf{v} - \mathbf{A}) = 0$ initially. Equation (6) ensures that $\nabla\times(\gamma\,\mathbf{v} - \mathbf{A}) = 0$ for all time. Thus, the momentum equation can be rewritten as[14]

$$\partial_t(\mathbf{u} - \mathbf{A}) = -\nabla\gamma, \tag{7}$$

where the fluid momentum $\mathbf{u} = \gamma\,\mathbf{v}$. It follows from this definition that $\gamma = \left(1 + u^2\right)^{1/2}$.

The ponderomotive term on the right side of Eq. (7) is valid for arbitrary laser intensity. Together with the continuity and Maxwell equations, it allows one to analyze the interaction of a laser pulse with an electron fluid. However, there is a tradition in plasma physics of looking at the same phenomenon from different viewpoints. By doing so, one often gains physical insight into the phenomenon under study. The ponderomotive term in Eq. (7) is not the force on a Lagrangian fluid element or a single electron. Consequently, it cannot be used as the foundation of a single-particle or kinetic analysis of the interaction of a laser pulse with a plasma.

In the following sections we present (1) an analytical study of the motion of an electron in a light wave of constant amplitude; (2) using the results of this study, a heuristic derivation of the formula for the ponderomotive force associated with a light wave of variable amplitude; (3) numerical and analytical verification of this formula; and, finally, (4) a summary of the results.

Particle Motion in a Plane Wave

The motion of a charged particle, of charge q and mass m, in an electromagnetic field is governed by the equation[15]

$$d_\tau\left(u_\mu + a_\mu\right) = u^\nu \partial_\mu a_\nu , \tag{8}$$

where τ is the proper time of the particle multiplied by c, u^μ is the four-velocity of the particle divided by c, a^μ is the four-potential of the field multiplied by q/mc^2 and $\partial_\mu = \partial/\partial x^\mu$. For an elliptically polarized field

$$a^\mu = \left(0, 0, e_y \cos\phi, e_z \sin\phi\right), \tag{9}$$

where $e_y = e\delta$, $e_z = e\left(1-\delta^2\right)^{1/2}$, and $\phi = t-x$.

The motion of a charged particle in a plane wave is well known.[16–19] We present an analysis of this motion here because it is the foundation of analyses presented later in this article. Since the four-potential does not depend on y or z, it follows from Eq. (8) that

$$d_\tau\left(\mathbf{u}_\perp + \mathbf{a}_\perp\right) = 0. \tag{10}$$

Transverse canonical momentum is conserved. It follows from Eq. (10) that

$$\mathbf{u}_\perp(\tau) = \mathbf{u}_\perp(0) + \mathbf{a}_\perp(0) - \mathbf{a}_\perp(\tau). \tag{11}$$

The t and x components of Eq. (8) are

$$d_\tau \gamma = \tfrac{1}{2}\partial_t u_\perp^2 , \quad d_\tau u_x = -\tfrac{1}{2}\partial_x u_\perp^2 . \tag{12}$$

Since the four-potential is a function of t–x, it follows from Eqs. (12) that

$$d_\tau\left(\gamma - u_\parallel\right) = 0. \tag{13}$$

Because the particle gains energy and momentum at the expense of the field, the ratio of particle momentum to particle kinetic energy is identical to the ratio of field momentum to field energy, which is 1 in the units of Eq. (8). By combining Eq. (13) with the definition of γ, one can show that

$$u_\parallel(\tau) = u_\parallel(0) + \frac{u_\perp^2(\tau) - u_\perp^2(0)}{2\left[\gamma(0) - u_\parallel(0)\right]}. \tag{14}$$

The corresponding equation for $\gamma(t)$ follows from Eqs. (13) and (14). Because the transverse potential $\mathbf{a}_\perp$ is a function of ϕ rather than τ, Eqs. (11) and (13) describe the particle momentum implicitly. One can make this description explicit and determine the particle trajectory $x^\mu(\tau)$ by using the result

$$d_\tau \phi = \gamma(0) - u_\parallel(0). \tag{15}$$

The proper frequency of the wave is constant.

It is clear from Eqs. (11), (14), and (15) that the particle motion is a superposition of sinusoidal oscillations in τ and steady drifts in τ. It follows from Eq. (11) that the transverse drifts are given by

$$\begin{aligned} \left\langle u_y \right\rangle &= u_y(0) + e_y \cos\left(-x_0\right), \\ \left\langle u_z \right\rangle &= u_z(0) + e_z \sin\left(-x_0\right), \end{aligned} \tag{16}$$

where $\langle . \rangle$ denotes the τ-average $\int_0^{2\pi} . \, d\tau/2\pi$ and $(x_0,0,0)$ is the initial position of the particle. By decomposing the longitudinal momentum into its oscillatory component

$$u_\parallel(\tau) - \left\langle u_\parallel \right\rangle = \frac{u_\perp^2(\tau) - \left\langle u_\perp^2 \right\rangle}{2\left[\gamma(0) - u_\parallel(0)\right]} \tag{17}$$

and its drift component

$$\left\langle u_\parallel \right\rangle = u_\parallel(0) + \frac{\left\langle u_\perp^2 \right\rangle - u_\perp^2(0)}{2\left[\gamma(0) - u_\parallel(0)\right]}, \tag{18}$$

and combining Eqs. (11) and (18), one can show that the longitudinal drift is given by

$$\begin{aligned} \left\langle u_x \right\rangle = u_x(0) + \Big[& 4\left\langle u_y \right\rangle e_y \cos\left(-x_0\right) \\ & + 4\left\langle u_z \right\rangle e_z \sin\left(-x_0\right) - e_y^2 \cos\left(-2x_0\right) \\ & + e_z^2 \cos\left(-2x_0\right)\Big] / 4\left[\gamma(0) - u_x(0)\right]. \end{aligned} \tag{19}$$

For linear polarization Eq. (19) reduces to

$$\begin{aligned} \left\langle u_x \right\rangle = u_x(0) + \Big[& 4\left\langle u_y \right\rangle e \cos\left(-x_0\right) \\ & - e^2 \cos\left(-2x_0\right)\Big] / 4\left[\gamma(0) - u_x(0)\right], \end{aligned} \tag{20}$$

whereas for circular polarization it reduces to

$$\langle u_x \rangle = u_x(0) + e\Big[\langle u_y \rangle \cos(-x_0) + \langle u_z \rangle \sin(-x_0)\Big]\Big/\sqrt{2}\,[\gamma(0) - u_x(0)]. \quad (21)$$

The corresponding equations for $\langle \gamma \rangle$ follow from Eq. (13) and Eqs. (19)–(21).

For completeness, a covariant analysis of the particle motion is given in **Appendix A**.

Heuristic Derivation of the Ponderomotive Force

The method used to solve Eq. (8) for a plane wave of constant amplitude can also be used when the wave amplitude e is a function of t–x. In fact, Eqs. (11), (14), and (15) are still valid. When the wave amplitude varies slowly compared to the wave phase, the particle motion consists of an oscillation about a guiding center and a guiding-center drift that varies slowly. As the guiding center drifts, the oscillation amplitude follows the wave amplitude at the guiding center adiabatically.

To describe this motion quantitatively, let ξ^μ be the position four-vector of the guiding center and $v^\mu = d_\tau \xi^\mu$ be the associated four-momentum. The ponderomotive four-force is the proper rate of change of the guiding-center four-momentum. One might expect this four-force to also be the average rate of change of the particle four-momentum. However, by averaging the transverse particle motion, one finds that

$$\begin{aligned} \langle d_\tau u_y \rangle &\approx \big[d_{\tau_0} e_y(\tau_0)\big]\cos(\tau_0), \\ \langle d_\tau u_z \rangle &\approx \big[d_{\tau_0} e_z(\tau_0)\big]\sin(\tau_0), \end{aligned} \quad (22)$$

where τ_0 is the initial phase with respect to which the average is taken. Because the oscillation amplitude changes during each oscillation, the transverse components of the momentum change by amounts that depend on the initial phase. However, it follows from Eq. (11) that the transverse components of the guiding-center momentum are constant. Thus, if one is to determine the ponderomotive four-force by averaging, one must discount terms that depend on the initial phase. With this caveat added to the definition of $\langle\,.\,\rangle$, one can write

$$d_\tau v_y = \langle d_\tau u_y \rangle \approx 0, \quad d_\tau v_z = \langle d_\tau u_z \rangle \approx 0 \quad (23)$$

and show that

$$d_\tau v_x = \langle d_\tau u_x \rangle \approx d_\tau\big(e_y^2 + e_z^2\big)\big/4\big[\gamma(0) - u_\parallel(0)\big]. \quad (24)$$

By using the relationship between x and ϕ, and Eq. (15), one can show that $d_\tau = -\big[\gamma(0) - u_\parallel(0)\big]\partial_x$. It follows from this result and Eq. (24) that

$$d_\tau v_x \approx -\partial_x\big(e^2/4\big). \quad (25)$$

In a similar way, one can show that

$$d_\tau v_t \approx \partial_t\big(e^2/4\big). \quad (26)$$

By using the facts that $e^2/2 = \langle a_\perp^2 \rangle$ and $a_\perp^2 = -a_\nu a^\nu$, one can rewrite Eqs. (23), (25), and (26) as

$$d_\tau v_\mu \approx -\partial_\mu \langle a_\nu a^\nu/2 \rangle. \quad (27)$$

The second term in this relation is the ponderomotive four-force.

The guiding-center Eq. (27) was derived for the special case in which e is a function of t–x. However, the principle of Lorentz covariance suggests that it is valid for the general case in which e is a function of t, x, y, and z. Consequently, we postulate that[20]

$$d_{\tau\tau}^2 \xi_\mu = -\partial_\mu \langle a_\nu a^\nu/2 \rangle\big|_{\xi_\mu} \quad (28)$$

and the initial guiding-center momentum in a wave of variable amplitude is identical to the particle drift momentum in a wave of constant amplitude, which is given by Eqs. (16) and (19). For future reference, Eq. (28) has associated with it the conservation equation

$$d_\tau\big(v_\mu v^\mu/2 + \langle a_\nu a^\nu/2 \rangle\big) = 0. \quad (29)$$

Numerical Study of the Particle Motion

To test the guiding-center model described in the previous section, we studied three representative examples numerically. The first example concerns a particle that moves in front of a laser pulse. We considered a wide, circularly polarized pulse,

with $e = 3\sin^2[0.05(t-x)]$, and chose $u_x(0) = 1$, $u_y(0) = 1$, and $u_z(0) = 1$. Because the pulse propagates at the speed of light, it overtakes the particle. The resulting particle motion is illustrated in Figs. 69.25 and 69.26, in which the solid lines denote the particle trajectory, determined numerically from Eq. (8) and the initial conditions, and the dashed lines denote the guiding-center trajectory, determined numerically from Eqs. (28), (16), and (19). As the pulse overtakes the particle, the amplitudes of the transverse components of the oscillation increase and decrease in proportion to the pulse intensity. However, there is no change in the transverse components of the average momentum, and the particle exits the pulse with $u_y = 1$ and $u_z = 1$. The amplitude of the longitudinal component of the oscillation also increases and decreases in proportion to the pulse intensity. However, because Eq. (14), which describes the relation between the longitudinal and transverse components of the momentum, is nonlinear, the longitudinal component of the average momentum changes. This change can be analyzed quantitatively. It follows from the t and x components of Eq. (28), and the assumed dependence of e on t–x, that

$$d_\tau(v_t - v_x) = 0. \tag{30}$$

Since v_y and v_z are constant, Eq. (29) reduces to

$$d_\tau\left[\left(v_t^2 - v_x^2\right)/2 - e^2/4\right] = 0. \tag{31}$$

By combining Eqs. (30) and (31) with the initial conditions, one can show that $v_t = 2 + e^2/4$ and $v_x = 1 + e^2/4$. At the peak of the pulse v_x = 13/4, in agreement with Fig. 69.25(a). Because the x component of the ponderomotive force is positive in the front of the pulse and negative in the back of the pulse, the guiding center is accelerated and decelerated by equal amounts. In this example the correspondence between the guiding-center motion and the particle motion is excellent.

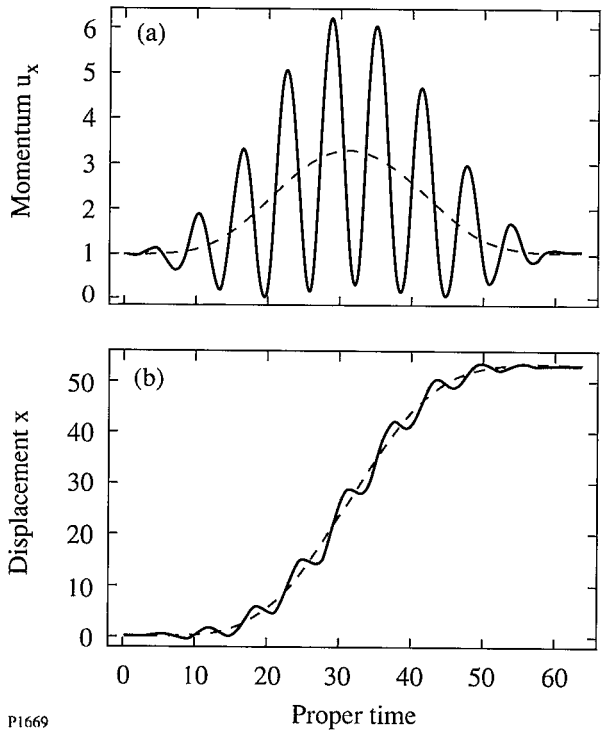

Figure 69.25
Particle motion (solid line) and guiding-center motion (dashed line) caused by a circularly polarized pulse with amplitude $e = 3\sin^2[0.05(t-x)]$. Initially, $u_x = 1$, $u_y = 1$, and $u_z = 1$. (a) The x component of the momentum. (b) The x component of the displacement caused by the pulse. The initial drift upon which this displacement is superimposed is not shown.

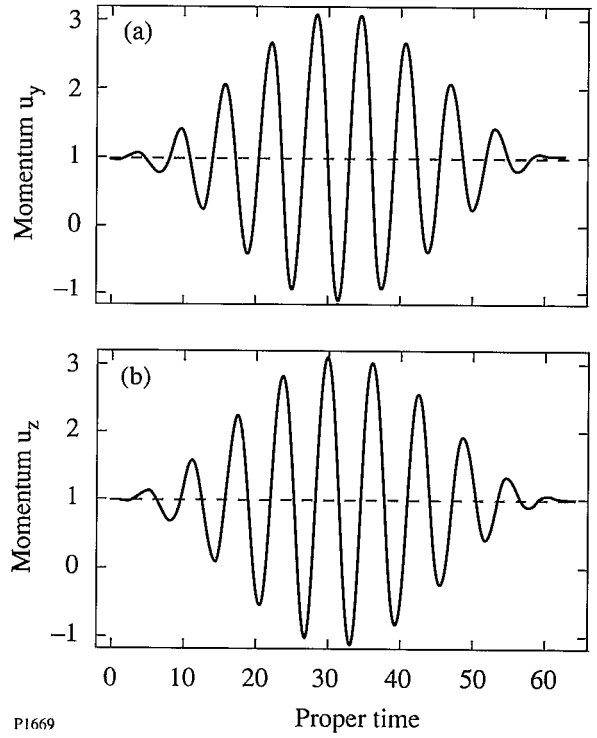

Figure 69.26
Particle motion (solid line) and guiding-center motion (dashed line) caused by a circularly polarized pulse with amplitude $e = 3\sin^2[0.05(t-x)]$. Initially, $u_x = 1$, $u_y = 1$, and $u_z = 1$. (a) The y component of the momentum. (b) The z component of the momentum.

The second example concerns a particle that is born inside a laser pulse by high-field ionization.[21] We considered a long pulse that is linearly polarized in the y direction, with $e = \cos^2(0.05\,z)$, and chose $u_x(0) = 0$, $u_y(0) = 0$, and $u_z(0) = 0$. The resulting particle motion is illustrated in Figs. 69.27 and 69.28. The particle is born near the propagation axis of the pulse and is pushed outward by the z component of the ponderomotive force. As the particle moves outward, the amplitudes of the longitudinal and transverse components of the oscillation decrease in proportion to the pulse intensity. This transverse expulsion can be analyzed quantitatively. Since v_t, v_x, and v_y are all constant, Eq. (29) reduces to

$$d_\tau\left(v_z^2/2 + e^2/4\right) = 0, \tag{32}$$

in which $v_z^2/2$ plays the role of kinetic energy and $e^2/4$ plays the role of potential energy. It follows from Eq. (32) and the initial conditions that $v_z^2 \approx \left(1 - e^2\right)/2$. As the guiding center exits the pulse, $v_z \approx 1/\sqrt{2}$, in agreement with Fig. 69.27(a). Although the particle is born at rest, it exits the pulse with $u_x \approx 3/4$ and $u_y \approx 1$. This behavior is consistent with Eqs. (16) and (19). In this example the correspondence between the guiding-center motion and the particle motion is excellent.

The third example concerns a particle that is injected into a laser pulse from the side. We considered a long pulse that is linearly polarized in the y direction, with $e = \sin^2(0.05y)$, and chose $u_x(0) = 0.0$, $u_y(0) = 0.7$, and $u_z(0) = 0.0$. The resulting particle motion is illustrated in Figs. 69.29 and 69.30. As the particle moves inward, the amplitudes of the longitudinal and transverse components of the oscillation increase in proportion to the pulse intensity. However, the y component of the ponderomotive force opposes the inward motion, and the particle is repelled just before it reaches the propagation axis of the pulse. As the particle moves outward, the amplitudes of the longitudinal and transverse components of the oscillation decrease in proportion to the pulse intensity. This transverse repulsion can be analyzed quantitatively. Since v_t, v_x, and v_z are all constant, Eq. (29) reduces to

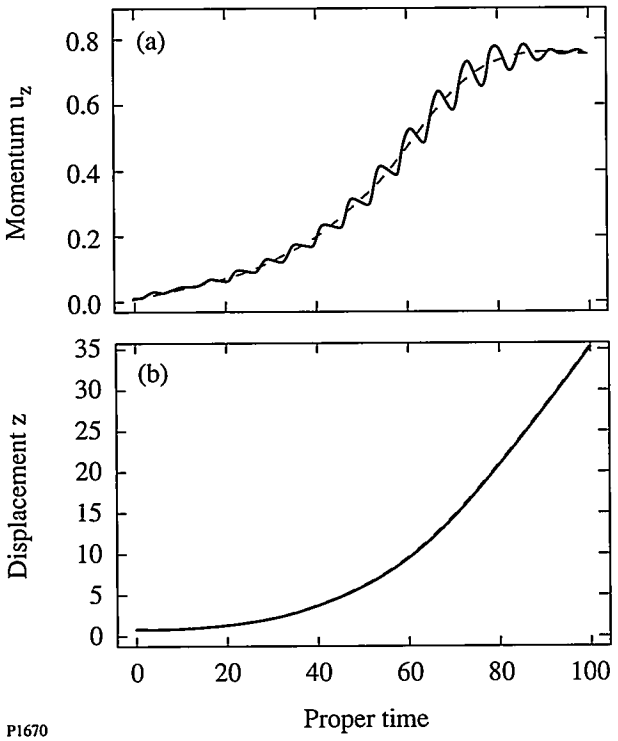

Figure 69.27
Particle motion (solid line) and guiding-center motion (dashed line) caused by a linearly polarized pulse with amplitude $e_y = \cos^2(0.05z)$. Initially, $u_x = 0$, $u_y = 0$, and $u_z = 0$. (a) The z component of the momentum. (b) The z component of the displacement.

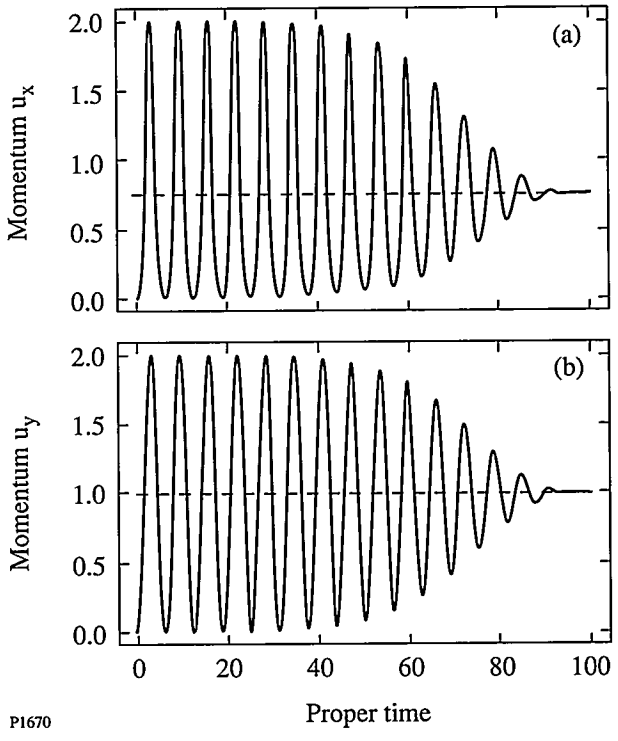

Figure 69.28
Particle motion (solid line) and guiding-center motion (dashed line) caused by a linearly polarized pulse with amplitude $e_y = \cos^2(0.05z)$. Initially, $u_x = 0$, $u_y = 0$, and $u_z = 0$. (a) The x component of the momentum. (b) The y component of the momentum.

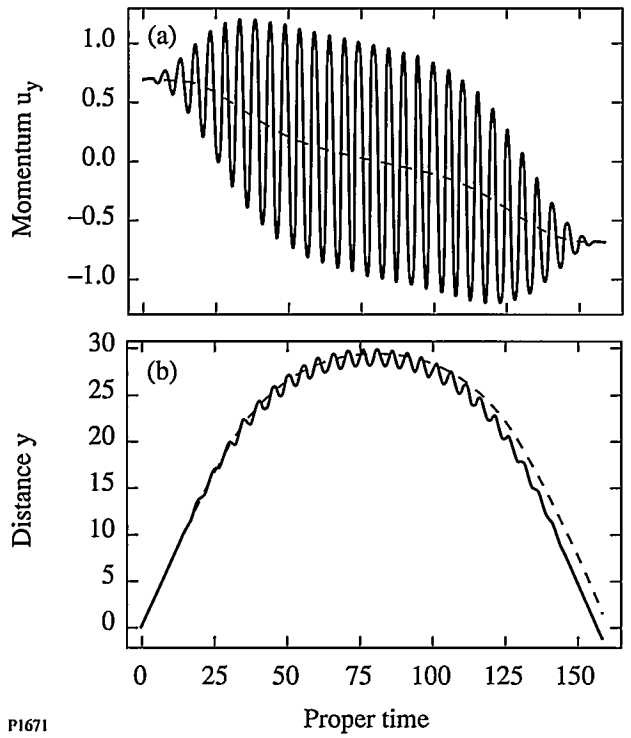

Figure 69.29
Particle motion (solid line) and guiding-center motion (dashed line) caused by a linearly polarized pulse with amplitude $e_y = \sin^2(0.05y)$. Initially, $u_x = 0.0$, $u_y = 0.7$, and $u_z = 0.0$. (a) The y component of the momentum. (b) The y component of the displacement.

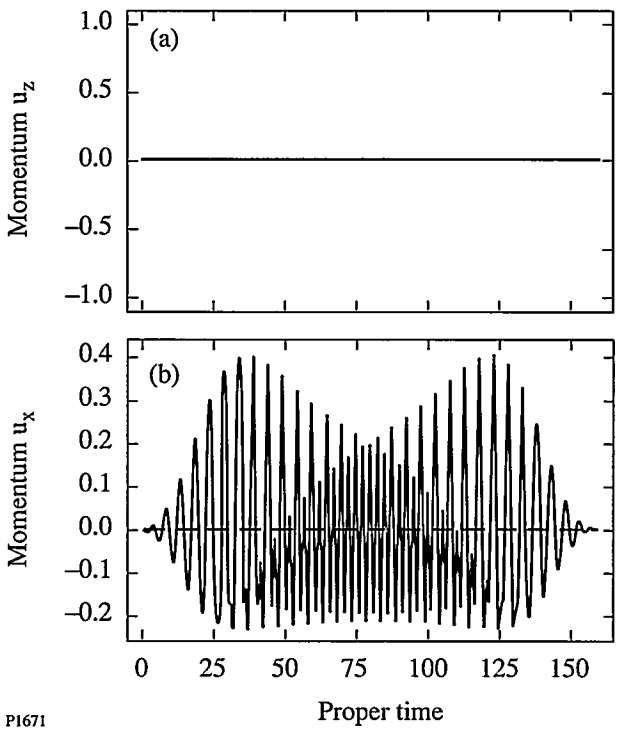

Figure 69.30
Particle motion (solid line) and guiding-center motion (dashed line) caused by a linearly polarized pulse with amplitude $e_y = \sin^2(0.05y)$. Initially, $u_x = 0.0$, $u_y = 0.7$, and $u_z = 0.0$. (a) The z component of the momentum. (b) The x component of the momentum.

$$d_\tau\left(v_y^2/2 + e^2/4\right) = 0. \tag{33}$$

It follows from Eq. (33) and the initial conditions that $v_y^2 \approx \left(1 - e^2\right)/2$. The outward guiding-center trajectory is the inverse of the inward trajectory. In this example the correspondence between the guiding-center motion and the particle motion is good. We found the correspondence to be even better for gentler gradients in pulse intensity.

In Figs. 69.25–69.30 the particle and guiding-center positions were plotted as functions of the proper time. We verified numerically that plotting the spatial components of the guiding-center position as functions of the temporal component of the guiding-center position produces the correct guiding-center motion in the laboratory frame.

Multiple Scale Analysis of the Particle Motion

In this section we verify Eq. (28) analytically. Because the fast variation of the four-potential depends on the phase rather than the proper time, it is advantageous to change the independent variable in Eq. (8) from τ to ϕ. The result is

$$d_\phi\left(d_\tau\phi\, d_\phi x_\mu + a_\mu\right) = d_\phi x^\nu \partial_\mu a_\nu, \tag{34}$$

where $d_\tau\phi = \left(d_\phi x^\nu d_\phi x_\nu\right)^{-1/2}$. The resolution of Eq. (34) into longitudinal and transverse components is facilitated by the introduction of the four-vector k^μ, which is defined by the equation $\phi = k^\nu x_\nu$, and the four-vector l^μ, which is defined by the equations $l^\nu l_\nu = 0$, $k^\nu l_\nu = 2$, and $a^\nu l_\nu = 0$, where a^μ is the transverse four-potential of a plane wave. In the laboratory frame $k^\mu = (1,1,0,0)$ and $l^\mu = (1,-1,0,0)$. By using these four-vectors one can write

$$x^\mu = y^\mu + \theta k^\mu/2 + \phi l^\mu/2, \tag{35}$$

where $\theta = l^\nu x_\nu$. The transverse position four-vector satisfies the equations $k^\nu y_\nu = 0$ and $l^\nu y_\nu = 0$. In a similar way, one can write

$$a^\mu = b^\mu + qk^\mu/2 + pl^\mu/2, \tag{36}$$

where the transverse four-potential satisfies the equations $k^\nu b_\nu = 0$ and $l^\nu b_\nu = 0$. By substituting the decompositions (35) and (36) into Eq. (34) and collecting like terms, one can show

$$\frac{d}{d\phi}\left(\frac{1}{\sigma}\frac{dy_\mu}{d\phi} + b_\mu\right) = \frac{\partial b^\nu}{\partial y^\mu}\frac{dy_\nu}{d\phi} + \frac{1}{2}\left(\frac{\partial p}{\partial y^\mu}\frac{d\theta}{d\phi} + \frac{\partial q}{\partial y^\mu}\right), \tag{37}$$

$$\frac{d}{d\phi}\left(\frac{1}{\sigma} + p\right) = 2\frac{\partial b^\nu}{\partial \theta}\frac{dy_\nu}{d\phi} + \frac{\partial p}{\partial \theta}\frac{d\theta}{d\phi} + \frac{\partial q}{\partial \theta}, \tag{38}$$

$$\frac{d}{d\phi}\left(\frac{1}{\sigma}\frac{d\theta}{d\phi} + q\right) = 2\frac{\partial b^\nu}{\partial \phi}\frac{dy_\nu}{d\phi} + \frac{\partial p}{\partial \phi}\frac{d\theta}{d\phi} + \frac{\partial q}{\partial \phi}, \tag{39}$$

where

$$\sigma = \left(d_\phi y^\nu d_\phi y_\nu + d_\phi \theta\right)^{1/2}. \tag{40}$$

Equation (39) can be derived from Eqs. (37) and (38), as shown in **Appendix B**, and need not be considered further.

One can solve Eqs. (37) and (38) by using multiple scale analysis. Let ε be a measure of the rate at which the wave amplitude varies relative to the rate at which the phase varies. We introduce the scales

$$\phi_0 = \phi, \quad \phi_1 = \varepsilon\phi \tag{41}$$

to resolve the fast oscillation and the slow change in the guiding-center drift, respectively. It follows that

$$\frac{d}{d\phi} = \frac{d}{d\phi_0} + \varepsilon\frac{d}{d\phi_1}. \tag{42}$$

We used the notation $d/d\phi_0$ and $d/d\phi_1$ in Eq. (42) to distinguish these convective derivatives from the partial derivatives of the four-potential. We assume that the dependent variables can be written as

$$\begin{aligned} y_\mu &\approx \varepsilon^{-1} y_\mu^{(-1)}(\phi_1) + y_\mu^{(0)}(\phi_0,\phi_1) + \varepsilon\, y_\mu^{(1)}(\phi_0,\phi_1), \\ \theta &\approx \varepsilon^{-1}\theta^{(-1)}(\phi_1) + \theta^{(0)}(\phi_0,\phi_1) + \varepsilon\,\theta^{(1)}(\phi_0,\phi_1). \end{aligned} \tag{43}$$

The variables $y_\mu^{(-1)}$ and $\theta^{(-1)}$ describe the guiding-center drift, which changes on the slow scale ϕ_1. The variables $y_\mu^{(0)}$ and $\theta^{(0)}$ describe the fast oscillation of the particle about the guiding center, the amplitude of which changes on the slow scale.

The four-potential satisfies Maxwell's wave equation[14]

$$\left(\partial^\lambda\partial_\lambda g_\nu^\mu - \partial^\mu\partial_\nu\right)a^\nu = 0, \tag{44}$$

where $g_\nu^\mu = \mathrm{diag}(1,-1,-1,-1)$ is the metric four-tensor. For a wave of constant amplitude, $a_\mu(x^\nu) = b_\mu^{(0)}(\phi_0)$. For a wave of variable amplitude we assume that

$$a_\mu(x^\nu) \approx a_\mu^{(0)}\left(\phi_0\middle|\varepsilon x^\nu\right) + \varepsilon a_\mu^{(1)}\left(\phi_0\middle|\varepsilon x^\nu\right). \tag{45}$$

Each contribution to the four-potential and its derivatives can be written approximately as

$$\begin{aligned} a\left(\phi_0\middle|\,\varepsilon y_\nu, \varepsilon\theta, \varepsilon\phi\right) \approx\; & a\left(\phi_0\middle| y_\nu^{(-1)}, \theta^{(-1)}, \phi_1\right) \\ & + \varepsilon y^{(0)\nu}\partial_\nu a\left(\phi_0\middle| y_\nu^{(-1)}, \theta^{(-1)}, \phi_1\right) \\ & + \varepsilon\theta^{(0)}\partial_\theta a\left(\phi_0\middle| y_\nu^{(-1)}, \theta^{(-1)}, \phi_1\right). \end{aligned} \tag{46}$$

The first term on the right side of Eq. (46) is the contribution evaluated at the guiding center, and the second and third terms are the deviations from this average contribution that are felt by the particle as it oscillates about the guiding center. The corresponding approximation for the convective derivative of the four-potential is discussed in **Appendix C**. Henceforth, we will use $\bar{a}$ to denote the guiding-center contribution

$$a\left(\phi_0\middle| y_\nu^{(-1)}, \theta^{(-1)}, \phi_1\right).$$

To proceed further one substitutes Eqs. (42), (43), and (46) in Eqs. (37) and (38) and collects terms of like order. The order ε^{-1} equations are satisfied identically by Ansaetze (43).

The order 1 equations are

$$\frac{d}{d\phi_0}\left[\frac{1}{\sigma^{(0)}}\frac{dy_\mu^{(0)}}{d\phi_0} + \bar{b}_\mu^{(0)}\right] = 0, \tag{47}$$

$$\frac{d}{d\phi_0}\left[\frac{1}{\sigma^{(0)}}\right]=0, \tag{48}$$

where

$$\sigma^{(0)}=\left\{\left[d_0 y^{(0)\nu}+d_1 y^{(-1)\nu}\right]\times\left[d_0 y_\nu^{(0)}+d_1 y_\nu^{(-1)}\right]+d_0\theta^{(0)}+d_1\theta^{(-1)}\right\}^{1/2} \tag{49}$$

and $d_n = d/d\phi_n$.

Equation (47) is the analog of Eq. (10). It follows from the former equation that

$$d_0 y_\mu^{(0)} = -\sigma^{(0)}\,\bar{b}_\mu^{(0)}. \tag{50}$$

The arbitrary function of ϕ_1 that results from the ϕ_0 integration can be neglected because $y_\mu^{(-1)}$ already accounts for the slowly varying drift with which this function is associated. Equations (48) and (49) do not resemble any of the equations in the section **Particle Motion in a Plane Wave**. However, different forms of the latter equations are discussed in **Appendix A**, from which it is clear that Eqs. (48) and (49) comprise the analog of Eq. (A9). It follows from Eq. (48) that $\sigma^{(0)}$ is a function of ϕ_1 alone. This result is the analog of Eq. (15) and facilitates the integration of Eq. (50). By combining Eqs. (49) and (50), and equating the oscillatory and slowly varying terms that result, one can show that

$$d_0\theta^{(0)} = 2\sigma^{(0)} d_1 y^{(-1)\nu}\,\bar{b}_\nu^{(0)} + \left[\sigma^{(0)}\right]^2\left[\left\langle \bar{b}^{(0)\nu}\,\bar{b}_\nu^{(0)}\right\rangle - \bar{b}^{(0)\nu}\,\bar{b}_\nu^{(0)}\right] \tag{51}$$

and

$$d_1\theta^{(-1)} + d_1 y^{(-1)\nu} d_1 y_\nu^{(-1)} = \left[\sigma^{(0)}\right]^2\left[1-\left\langle \bar{b}^{(0)\nu}\,\bar{b}_\nu^{(0)}\right\rangle\right]. \tag{52}$$

Equation (51) is the analog of Eq. (17) and the oscillatory part of Eq. (A7), and is easy to integrate.

Now consider the initial condition on the order 1 four-momentum. Consistent with Eq. (35), one can write the initial four-momentum as

$$u^\mu(0) = v^\mu(0) + l^\nu u_\nu(0) k^\mu/2 + k^\nu u_\nu(0) l^\mu/2. \tag{53}$$

It follows immediately that

$$d_1 y_\mu^{(-1)}(0) = \sigma^{(0)} v_\mu(0) - d_0 y_\mu^{(0)}(0), \tag{54}$$

$$d_1\theta^{(-1)}(0) = \sigma^{(0)} l^\nu u_\nu(0) - d_0\theta^{(0)}(0). \tag{55}$$

Equation (54) is the analog of Eqs. (16), and Eq. (55) is consistent with Eqs. (17) and (18).

The order ε equations are

$$\frac{d}{d\phi_1}\left\{\frac{1}{\sigma^{(0)}}\left[\frac{dy_\mu^{(0)}}{d\phi_0}+\frac{dy_\mu^{(-1)}}{d\phi_1}\right]+\bar{b}_\mu^{(0)}\right\} + \frac{d}{d\phi_0}\left\{\frac{1}{\sigma^{(0)}}\left[\frac{dy_\mu^{(1)}}{d\phi_0}+\frac{dy_\mu^{(0)}}{d\phi_1}\right]+\bar{b}_\mu^{(1)}\right\} - \frac{d}{d\phi_0}\left\{\frac{\sigma^{(1)}}{2\left[\sigma^{(0)}\right]^3}\left[\frac{dy_\mu^{(0)}}{d\phi_0}+\frac{dy_\mu^{(-1)}}{d\phi_1}\right]\right\} = \left[\frac{dy^{(0)\nu}}{d\phi_0}+\frac{dy^{(-1)\nu}}{d\phi_1}\right]\frac{\partial \bar{b}_\nu^{(0)}}{\partial y^\mu} \tag{56}$$

and

$$\frac{d}{d\phi_1}\left[\frac{1}{\sigma^{(0)}}\right]-\frac{d}{d\phi_0}\left\{\frac{\sigma^{(1)}}{2\left[\sigma^{(0)}\right]^3}+\bar{p}^{(1)}\right\} = 2\left[\frac{dy^{(0)\nu}}{d\phi_0}+\frac{dy^{(-1)\nu}}{d\phi_1}\right]\frac{\partial \bar{b}_\nu^{(0)}}{\partial\theta}, \tag{57}$$

where

$$\sigma^{(1)} = \frac{d\theta^{(1)}}{d\phi_0} + \frac{d\theta^{(0)}}{d\phi_1} + 2\left[\frac{dy^{(0)\nu}}{d\phi_0} + \frac{dy^{(-1)\nu}}{d\phi_1}\right]\left[\frac{dy^{(1)}_{\nu}}{d\phi_0} + \frac{dy^{(0)}_{\nu}}{d\phi_1}\right], \tag{58}$$

and $\bar{b}_{\mu}^{(1)}$ and $\bar{p}^{(1)}$ represent the sum of the order ε four-potential and the order ε corrections to the order-1 four-potential caused by the oscillation of the particle about the guiding center.

Although Eqs. (56)–(58) are lengthy, they do not need to be solved in their entirety. By equating the slowly varying terms in Eqs. (56) and (57), one can show that

$$\frac{1}{\sigma^{(0)}}\frac{d}{d\phi_1}\left[\frac{1}{\sigma^{(0)}}\frac{dy_{\mu}^{(-1)}}{d\phi_1}\right] = -\frac{1}{2}\frac{\partial\left\langle \bar{b}^{(0)\nu}\,\bar{b}_{\nu}^{(0)}\right\rangle}{\partial y^{\mu}} \tag{59}$$

and

$$\frac{1}{\sigma^{(0)}}\frac{d}{d\phi_1}\left[\frac{1}{\sigma^{(0)}}\right] = -\frac{\partial\left\langle \bar{b}^{(0)\nu}\,\bar{b}_{\nu}^{(0)}\right\rangle}{\partial\theta}. \tag{60}$$

It follows from Eq. (52) that

$$\frac{1}{\sigma^{(0)}}\frac{d}{d\phi_1}\left[\frac{1}{\sigma^{(0)}}\frac{d\theta^{(-1)}}{d\phi_1}\right] = \frac{1-\left\langle \bar{b}^{(0)\nu}\,\bar{b}_{\nu}^{(0)}\right\rangle}{\sigma^{(0)}}\frac{d\sigma^{(0)}}{d\phi_1} - \frac{d\left\langle \bar{b}^{(0)\nu}\,\bar{b}_{\nu}^{(0)}\right\rangle}{d\phi_1} - \frac{1}{\sigma^{(0)}}\frac{d}{d\phi_1}\left\{\sigma^{(0)}\left[\frac{1}{\sigma^{(0)}}\frac{dy^{(-1)\nu}}{d\phi_1}\right]\left[\frac{1}{\sigma^{(0)}}\frac{dy_{\nu}^{(-1)}}{d\phi_1}\right]\right\}. \tag{61}$$

When applied to any guiding-center quantity, the operator

$$\frac{d}{d\phi_1} = \frac{dy^{(-1)\nu}}{d\phi_1}\frac{\partial}{\partial y^{\nu}} + \frac{\partial}{\partial\phi_1} + \frac{d\theta^{(-1)}}{d\phi_1}\frac{\partial}{\partial\theta}. \tag{62}$$

By combining Eq. (61) with Eqs. (59), (60), and (62), one can show that

$$\frac{1}{\sigma^{(0)}}\frac{d}{d\phi_1}\left[\frac{1}{\sigma^{(0)}}\frac{d\theta^{(-1)}}{d\phi_1}\right] = -\frac{\partial\left\langle \bar{b}^{(0)\nu}\,\bar{b}_{\nu}^{(0)}\right\rangle}{\partial\phi_1}. \tag{63}$$

Recall that the preceding derivation of Eq. (63) is based on Eq. (38). Had we analyzed Eq. (39) instead, we would have needed to determine $b_{\nu}^{(1)}$, $p^{(1)}$, $q^{(1)}$, and $y_{\nu}^{(1)}$ explicitly.

In the notation of this section, Eq. (28) can be rewritten as

$$\frac{d^2x_{\mu}^{(-1)}}{d\tau_1^2} = -\frac{1}{2}\frac{\partial\left\langle \bar{b}^{(0)\nu}\,\bar{b}_{\nu}^{(0)}\right\rangle}{\partial x_1^{\mu}}, \tag{64}$$

where $\tau_1 = \varepsilon\tau$ and $x_1^{\mu} = \varepsilon x^{\mu}$. Since $d\phi_1/d\tau_1 \approx 1/\sigma^{(0)}$, Eq. (59) is the transverse part of Eq. (64). By contracting Eq. (64) with k^{μ} and l^{μ}, and using the identities $k^{\mu}\partial_{\mu} = 2\partial_{\theta}$ and $l^{\mu}\partial_{\mu} = 2\partial_{\phi}$, and the fact that $\phi \approx k^{\mu}x_{\mu}^{(-1)}$, one can show that Eqs. (60) and (63) are equivalent to the longitudinal part of Eq. (64). Thus, Eq. (28) is correct.

Finally, notice that Eq. (64) for the guiding-center drift is written in terms of the proper time, which includes the effects of the oscillation about the guiding center. Although this fact does not affect the utility of Eq. (64), it calls into question the aesthetic qualities of the equation. Just as the proper time is defined by the equation $d\tau = \left(dx^{\nu}dx_{\nu}\right)^{1/2}$, one can define the drift time by the equation $ds = \left[dx^{(-1)\nu}\,dx_{\nu}^{(-1)}\right]^{1/2}$.

It follows from this definition, Eq. (52), and the discussion of the preceding paragraph that

$$\frac{ds_1}{d\tau_1} = \left[1 - \left\langle \bar{b}^{(0)\nu}\,\bar{b}_{\nu}^{(0)}\right\rangle\right]^{1/2}. \tag{65}$$

Equation (65) can be used to write Eq. (28) in terms of the drift time.

Summary

In this article we solved the equation of motion for an electron in a plane wave. We used this solution and the principle of Lorentz covariance to deduce a formula for the ponderomotive force exerted by an intense laser pulse on an electron. We verified this formula numerically, for three cases of current interest, and analytically, using the method of multiple scales.

The aforementioned formula can be used to study the effects of the radial ponderomotive force on laser-plasma interactions. For particle accelerators, these effects include the divergence of an electron bunch that is accelerated by a laser pulse,[22] the relativistic focusing of the pulse, and electron cavitation and magnetic field generation in the wake of the pulse.

ACKNOWLEDGMENT

This work was supported by the National Science Foundation under Contracts No. PHY-9057093 and PHY-9415583, the U.S. Department of Energy Office of Inertial Confinement Fusion under Cooperative Agreement No. DE-FC03-92SF19460, the University of Rochester, and the New York State Energy Research and Development Authority. The support of DOE does not constitute an endorsement by DOE of the views expressed in this article.

Appendix A: Covariant Analysis of the Particle Motion in a Plane Wave

The motion of a charged particle in an electromagnetic field is governed by Eq. (8). For a plane wave the four-potential a^μ is a function of the phase $\phi = k^\nu x_\nu$. It follows that $\partial_\mu a_\nu = k_\mu a'_\nu$, where $' = d/d\phi$, and, hence, that

$$d_\tau\left(u_\mu + a_\mu\right) = u^\nu k_\mu a'_\nu. \tag{A1}$$

By substituting the decomposition

$$u_\mu(\tau) = v_\mu(\tau) + k^\nu u_\nu(\tau) l_\mu/2 + l^\nu u_\nu(\tau) k_\mu/2 \tag{A2}$$

into Eq. (A1), where l^ν was defined after Eq. (8), and v_μ satisfies the equations $k^\nu v_\nu = 0$ and $l^\nu v_\nu = 0$, one can show that

$$d_\tau\left(v_\mu + a_\mu\right) = 0,\ d_\tau\left(k^\nu u_\nu\right) = 0,\ d_\tau\left(l^\nu u_\nu\right) = 2v^\nu a'_\nu. \tag{A3}$$

It follows from the first of Eqs. (A3) that

$$v_\mu(\tau) = v_\mu(0) + a_\mu(0) - a_\mu(\tau). \tag{A4}$$

It follows from the second of Eqs. (A3) that

$$k^\nu u_\nu(\tau) = k^\nu u_\nu(0) \tag{A5}$$

and, hence, that

$$\phi = k^\nu u_\nu(0)\tau. \tag{A6}$$

Equations (A4) and (A6) determine $v_\mu(\tau)$ explicitly. There are at least three ways to obtain an expression for $l^\nu u_\nu$. In the first approach, one uses Eq. (A4) to rewrite the right side of the third of Eqs. (A3) in terms of a^μ. It follows from this equation and Eq. (A6) that

$$\begin{aligned} l^\nu u_\nu(\tau) = {} & l^\nu u_\nu(0) + 2\left[v^\nu(0) + a^\nu(0)\right] \\ & \times\left[a_\nu(\tau) - a_\nu(0)\right]/k^\nu u_\nu(0) \\ & + \left[a^\nu(0)a_\nu(0) - a^\nu(\tau)a_\nu(\tau)\right]/k^\nu u_\nu(0). \end{aligned} \tag{A7}$$

In the second approach, one uses Eq. (A4) to rewrite the right side of the third of Eqs. (A3) in terms of v^μ. It follows from this equation and Eq. (A6) that

$$\begin{aligned} l^\nu u_\nu(\tau) = {} & l^\nu u_\nu(0) + \left[v^\nu(0)v_\nu(0)\right. \\ & \left. - v^\nu(\tau)v_\nu(\tau)\right]/k^\nu u_\nu(0). \end{aligned} \tag{A8}$$

In the third approach one uses decomposition (A2) to rewrite the identity $u^\nu u_\nu = 1$ as

$$\left(k^\nu u_\nu\right)\left(l^\nu u_\nu\right) + v^\nu v_\nu = 1. \tag{A9}$$

Since $k^\nu u_\nu$ and $v^\nu v_\nu$ are known quantities, Eq. (A9) provides a third expression for $l^\nu u_\nu$. By rewriting the 1 on the right side of Eq. (A9) in terms of the initial values of the quantities on the left side, one can rewrite Eq. (A9) in the form of Eq. (A8). All three approaches have their uses. Equation (A4) is the covariant version of Eq. (11), and Eqs. (A5) and (A8) are the covariant versions of Eq. (14) for $u_\parallel$ and its analog for γ.

Appendix B: Covariant Lagrangian for the Particle Motion

For a particle in an electromagnetic field the normalized motion[19]

$$S = -\int\left[\left(dx^{\nu}dx_{\nu}\right)^{1/2} + a^{\nu}dx_{\nu}\right]. \tag{B1}$$

Traditionally, one parameterizes the particle motion in terms of the proper time τ, which is a Lorentz invariant. In this case

$$S = -\int\left[\left(d_{\tau}x^{\nu}d_{\tau}x_{\nu}\right)^{1/2} + a^{\nu}d_{\tau}x_{\nu}\right]d\tau. \tag{B2}$$

By applying the Euler-Lagrange equations to the integrand of Eq. (B2), one finds that

$$d_{\tau}\left(d_{\tau}x_{\mu} + a_{\mu}\right) = d_{\tau}x^{\nu}\partial_{\mu}a_{\nu}, \tag{B3}$$

in agreement with Eq. (8). Alternately, one can parameterize the particle motion by the phase $\phi = k^{\nu}x_{\nu}$, which is also a Lorentz invariant. In this case

$$S = -\int\left[\left(d_{\phi}x^{\nu}d_{\phi}x_{\nu}\right)^{1/2} + a^{\nu}d_{\phi}x_{\nu}\right]d\phi. \tag{B4}$$

By using the decompositions (35) and (36) one can rewrite Eq. (B4) as

$$S = -\int\left[\left(d_{\phi}y^{\nu}d_{\phi}y_{\nu} + d_{\phi}\theta\right)^{1/2} + b^{\nu}d_{\phi}y_{\nu} + pd_{\phi}\theta/2 + q/2\right]d\phi. \tag{B5}$$

By applying the Euler-Lagrange equations to the integrand of Eq. (B5), one can show that

$$\frac{d}{d\phi}\left[\frac{1}{\left(d_{\phi}y^{\nu}d_{\phi}y_{\nu} + d_{\phi}\theta\right)^{1/2}}\frac{dy_{\mu}}{d\phi} + b_{\mu}\right]$$

$$= \frac{\partial b^{\nu}}{\partial y^{\mu}}\frac{dy_{\nu}}{d\phi} + \frac{1}{2}\left(\frac{\partial p}{\partial y^{\mu}}\frac{d\theta}{d\phi} + \frac{\partial q}{\partial y^{\mu}}\right), \tag{B6}$$

$$\frac{d}{d\phi}\left[\frac{1}{\left(d_{\phi}y^{\nu}d_{\phi}y_{\nu} + d_{\phi}\theta\right)^{1/2}} + q\right]$$

$$= 2\frac{\partial b^{\nu}}{\partial\theta}\frac{dy_{\nu}}{d\phi} + \frac{\partial p}{\partial\theta}\frac{d\theta}{d\phi} + \frac{\partial q}{\partial\theta}, \tag{B7}$$

in agreement with Eqs. (37) and (38). One can reproduce Eq. (39) by multiplying Eq. (B6) by $-2d_{\phi}y^{\mu}$ and Eq. (B7) by $-d_{\phi}\theta$, and adding the resulting equations.

Appendix C: Evaluation of the Four-Potential

The left side of Eq. (34) contains the term $da_{\mu}/d\phi$, which must be evaluated at the position of the particle. In the section **Multiple Scale Analysis of the Particle Motion** we used Eqs. (42), (43), and (46) to make a guiding-center expansion of a_{μ} *before* we took the convective derivative. Specifically, we wrote

$$d_{\phi}a_{\mu} \approx \left[d_0 + \varepsilon d_1\right]\left[a_{\mu}^{(0)} + \varepsilon a^{(1)}\right], \tag{C1}$$

where

$$a_{\mu}^{(0)} = \overline{a}_{\mu} \tag{C2}$$

is the four-potential evaluated at the guiding center and

$$\overline{a}_{\mu}^{(1)} = y^{(0)\nu}\partial_{\nu}\overline{a}_{\mu} + \theta^{(0)}\partial_{\theta}\overline{a}_{\mu} \tag{C3}$$

is the correction to the four-potential caused by the oscillation of the particle about the guiding center. Since the guiding-center coordinates $y^{(-1)}$ and $\theta^{(-1)}$ are functions of ϕ_1 by construction,

$$\frac{d\overline{a}_{\mu}}{d\phi_0} = \frac{\partial\overline{a}_{\mu}}{\partial\phi_0} \tag{C4}$$

and

$$\frac{d\overline{a}_{\mu}}{d\phi_1} = \frac{dy^{(-1)\nu}}{d\phi_1}\frac{\partial\overline{a}_{\mu}}{\partial y^{\nu}} + \frac{\partial\overline{a}_{\mu}}{\partial\phi_1} + \frac{d\theta^{(-1)}}{d\phi_1}\frac{\partial\overline{a}_{\mu}}{\partial\theta}. \tag{C5}$$

It follows from Eqs. (C1), (C4), and (C5) that

$$\left[\frac{da_\mu}{d\phi}\right]^{(0)} = \frac{\partial \bar{a}_\mu}{\partial \phi_0} \tag{C6}$$

and

$$\left[\frac{da_\mu}{d\phi}\right]^{(1)} = \frac{dy^{(-1)\nu}}{d\phi_1}\frac{\partial \bar{a}_\mu}{\partial y^\nu} + \frac{\partial \bar{a}_\mu}{\partial \phi_1} + \frac{d\theta^{(-1)}}{d\phi_1}\frac{\partial \bar{a}_\mu}{\partial \theta}$$

$$+ \frac{dy^{(0)\nu}}{d\phi_0}\frac{\partial \bar{a}_\mu}{\partial y^\nu} + y^{(0)\nu}\frac{\partial^2 \bar{a}_\mu}{\partial \phi_0 \partial y^\nu}$$

$$+ \frac{d\theta^{(0)}}{d\phi_0}\frac{\partial \bar{a}_\mu}{\partial \theta} + \theta^{(0)}\frac{\partial^2 \bar{a}_\mu}{\partial \phi_0 \partial \theta}. \tag{C7}$$

Alternately, one can write

$$\frac{da_\mu}{d\phi} = \frac{dy^\nu}{d\phi}\frac{\partial a_\mu}{\partial y^\nu} + \frac{\partial a_\mu}{\partial \phi} + \frac{d\theta}{d\phi}\frac{\partial a_\mu}{\partial \theta}, \tag{C8}$$

in which the guiding-center expansion is made *after* the partial derivatives are taken. Since the variation of a_μ with the position variables y^ν and θ is slow,

$$\frac{da_\mu}{d\phi} \approx \varepsilon\left[\frac{dy^{(0)\nu}}{d\phi_0} + \frac{dy^{(-1)\nu}}{d\phi_1}\right]\frac{\partial a_\mu}{\partial y^\nu} + \frac{\partial a_\mu}{\partial \phi_0}$$

$$+ \varepsilon\frac{\partial a_\mu}{\partial \phi_1} + \varepsilon\left[\frac{d\theta^{(0)}}{d\phi_0} + \frac{d\theta^{(-1)}}{d\phi_1}\right]\frac{\partial a_\mu}{\partial \theta}. \tag{C9}$$

The derivatives of the four-potentials appearing in the order ε terms can be approximated by their guiding-center values. The remaining term

$$\frac{\partial a_\mu}{\partial \phi_0} \approx \frac{\partial \bar{a}_\mu}{\partial \phi_0} + \varepsilon y^{(0)\nu}\frac{\partial^2 \bar{a}_\mu}{\partial y^\nu \partial \phi_0} + \varepsilon\theta^{(0)}\frac{\partial^2 \bar{a}_\mu}{\partial \theta \partial \phi_0}. \tag{C10}$$

Equations (C9) and (C10) are equivalent to Eqs. (C4) and (C5). This result shows that the guiding-center expansion discussed previously was made consistently. The expansion based on Eq. (C1) is better because it facilitates the identification of combinations of terms that are oscillatory and, hence, do not affect the guiding-center motion.

REFERENCES

1. H. A. H. Boot and R. B. R. S. Harvie, Nature **180**, 1187 (1957).
2. H. A. H. Boot, S. A. Self, and R. B. R. S. Harvie, J. Electron. Control **IV**, 434 (1958).
3. A. V. Gaponov and M. A. Miller, Sov. Phys.-JETP **7**, 168 (1958).
4. A. V. Gaponov and M. A. Miller, Sov. Phys.-JETP **7**, 515 (1958).
5. G. A. Askar'yan, Sov. Phys.-JETP **15**, 1088 (1962).
6. N. J. Phillips and J. J. Sanderson, Phys. Lett. **21**, 533 (1966).
7. T. W. B. Kibble, Phys. Rev. Lett. **16**, 1054 (1966).
8. T. W. B. Kibble, Phys. Rev. **150**, 1060 (1966).
9. F. F. Chen, *Introduction to Plasma Physics and Controlled Fusion*, 2nd ed. (Plenum Press, New York, 1984), Vol. 1, p. 305.
10. W. L. Kruer, *The Physics of Laser Plasma Interactions*, Frontiers in Physics, Vol. 73 (Addison-Wesley, Redwood City, CA, 1988), p. 60.
11. R. S. Craxton, R. L. McCrory, and J. M. Soures, Sci. Am. **255**, 68 (1986).
12. J. M. Dawson, Sci. Am. **260**, 54 (1989).
13. M. D. Perry and G. Mourou, Science **264**, 917 (1994).
14. C. J. McKinstrie and D. F. DuBois, Phys. Fluids **31**, 278 (1988).
15. H. Goldstein, *Classical Mechanics*, 2nd ed. (Addison-Wesley, Reading, MA, 1980), p. 303.
16. D. M. Volkov, Z. Phys. **94**, 250 (1935).
17. T. J. M. Boyd and J. J. Sanderson, *Plasma Dynamics* (Barnes and Noble, New York, 1969), p. 26.
18. P. C. Clemmow and J. P. Dougherty, *Electrodynamics of Particles and Plasmas* (Addison-Wesley, Reading, MA, 1969), p. 122.
19. L. D. Landau and E. M. Lifshitz, *The Classical Theory of Fields*, 4th ed. (Pergamon Press, Oxford, 1975), pp. 45, 112, and 118.
20. E. A. Startsev and C. J. McKinstrie, Bull. Am. Phys. Soc. **40**, 1723 (1995).
21. C. I. Moore, J. P. Knauer, and D. D. Meyerhofer, Phys. Rev. Lett. **74**, 2439 (1995).
22. C. J. McKinstrie and E. A. Startsev, Phys. Rev. E **54**, R1070 (1996).

Subpicosecond Imaging System Based on Electro-Optic Effect

Ultrafast electro-optic (EO) sampling was first demonstrated in 1982[1] and has since become a valuable tool for testing optoelectronic and electronic devices and materials.[2] Conventional EO sampling of weak electric fields employs a tightly focused, pulsed-laser probe beam to measure electric-field-induced birefringence in an EO crystal; hence, it is referred to as "point" sampling.

Densely packed analog and digital devices make it necessary to probe many nodes simultaneously. Meyer and Mourou[3] first demonstrated electric field mapping by scanning an area using a point sampler. Mertin[4] reviews the development of two-dimensional field measurement technologies including an automated scanning point sampler. Two groups studying photoconductive switches[5,6] pioneered the use of EO imaging, by mapping the field strength with a detector array. Their work differs from the present in that their devices exhibited high fields and were adequately described with 200-ps temporal resolution.

An EO sampling system capable of imaging the voltage distribution over a rectangular region is described. It is comparable to an ultrafast sampling oscilloscope having more than 180,000 channels. This analysis focuses on techniques that take advantage of the speed and convenience of a charge-coupled-device (CCD) sensor while overcoming its limited dynamic range.

System Descriptions

EO sampling requires a pulsed (or gated) laser source to probe the response of the device to the applied transient. Our lab uses a mode-locked Coherent Mira 900 Ti:sapphire laser. It produces a 76-MHz train of linearly polarized, ≈100-fs FWHM pulses, tuned to ≈800 nm. Devices tested in our lab generally include a photoconductive switch that is excited with a fraction of the pulsed beam, thus triggering the measurement and eliminating electrical jitter.

In a point sampler,[2] the EO crystal may be either the device substrate (e.g., GaAs devices) or on an external probe. A linearly polarized optical probe pulse enters the crystal through the first surface. In transmissive sampling, the probe is transmitted at the second surface after a single pass, whereas in reflective sampling, it is reflected, passing through the crystal a second time. The beam exits the crystal and is passed through a compensator or wave plate to introduce a static polarization bias. The bias is adjusted so that in the absence of an electric field, the probe is circularly polarized at the input of an analyzer, thus giving maximum sensitivity and linearity when a field is applied. The analyzer separates the beam into orthogonal polarization components, which are measured by a pair of detectors connected to a differential lock-in amplifier. Signal-to-noise improvements are obtained when the signal is modulated at frequencies approaching the laser $1/f$ noise floor.

Figure 69.31 depicts the imaging system hardware. Reflective sampling was chosen because it doubles system sensitivity, although transmissive sampling is also possible. The laser source is directed through a high-speed modulator followed by a variable-intensity beam splitter consisting of a half-wave plate and polarizing beam splitter. The horizontally polarized "probe" beam is directed back through the polarizer, then into a spatial filter and beam expander. The vertically polarized "excitation" beam passes through a variable-length optical delay and into a fiber coupler.

The probe beam is split into two beams in a small, rigid interferometer. The device-under-test (DUT) is mounted in the device "leg" of the interferometer, and a mirror is installed in the reference "leg." The beams pass through a polarizing filter and relay lens to create an interference pattern at the camera. The beam splitter in the interferometer is an uncoated, ≈3-mm-thick, BK-7 wedged window. The first surface of the window is aligned at Brewster's angle to eliminate multiple reflections and maximize transmitted intensity. The reference

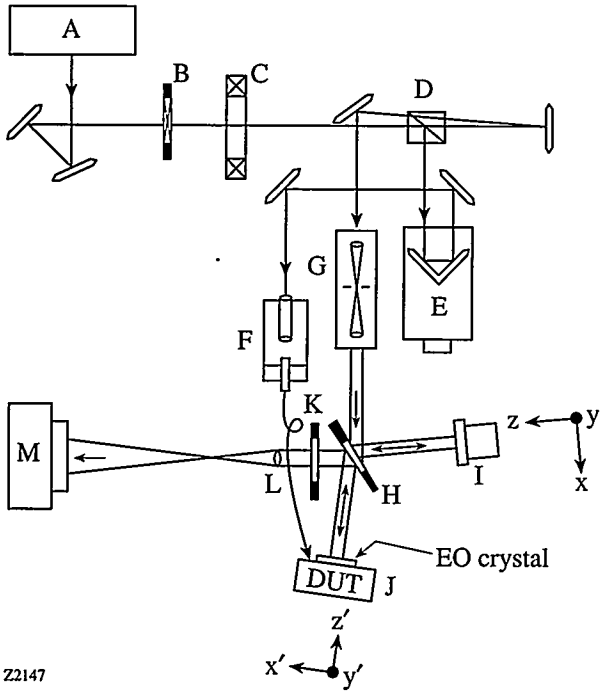

Figure 69.31
Imaging system hardware: (A) Ti:sapphire laser, (B) high-frequency modulator, (C) half-wave plate, (D) polarizing beam splitter, (E) optical delay stage, (F) excitation beam fiber coupler, (G) spatial filter and probe beam expander, (H) wedged beam splitter, (I) reference mirror on piezoelectric actuator, (J) EO crystal on DUT, (K) polarizing filter, (L) relay lens and aperture, and (M) CCD camera.

mirror is mounted on a piezoelectric actuator, which is used to modulate the length of the reference leg. The DUT is mounted on a stationary structure. Each leg has adjustments for static alignment.

As in point sampling, the electric fields on the DUT are measured by using the linear EO, or Pockels, effect. A propagating electrical transient is launched on the DUT when an optical excitation pulse is applied to a biased, photoconductive switch. An EO crystal having a high-reflectivity (HR) coating on one side covers the region of interest with the coating in intimate contact with the DUT. "Fringing" E-fields caused by the propagating transient couple into the crystal to produce a temporally and spatially variant refractive index.

The EO-induced index perturbation in the crystal alters the phase of the linearly polarized optical probe as it traverses the device leg of the interferometer. When recombined with an unperturbed reference beam, an intensity pattern results that corresponds to phase differences between the two legs of the interferometer. If the reference beam is static, then changes in intensity at each point can be attributed to spatial phase variations in the crystal induced by the EO effect.

A video camera (DVC Corp., DVC-0A) having a low-noise, frame-transfer charge-coupled device (CCD) (Texas Instruments, TC-245) records the intensity pattern created by the interferometer. The analog camera output is digitized by a frame grabber (Matrox Corp., Pulsar) and stored on a personal computer (Pentium 133-MHz, PCI bus). Timing control for modulation uses custom-built electronics (see **Modulation** section).

Spatial resolution of the system is determined by the active image area and number of discrete pixels in the image sensor. Image (de)magnification can be adjusted by altering the position of the relay lens and camera.

The CCD has 755 (8.5-μm) pixels horizontally (H) and 242 (19.75-μm) pixels vertically (V) for an active area of 6.4 mm (H) × 4.8 mm (V). Typical magnification is 4:1, giving a measurement area of 1.6 mm (H) × 1.2 mm (V). The resulting spatial resolution is 2.13 μm (H) × 4.9 μm (V), which is comparable to point sampling. If desired, cylindrical lenses or prisms could be used to correct the pixel aspect ratio.

It is possible to increase optical magnification to 8:1, then digitally average 2 × 2-pixel cells to obtain 4:1 effective magnification. This would reduce noise by 1/2; however, it may prove disadvantageous since more photons from the excitation source will be collected by the sensor [see also **Interferometer Operation** section].

Important distinctions exist between the imager and scanning point samplers. The imaged nodes must lie within a finite rectangular region, whereas a scanning system can probe random points over an extended area. Furthermore, the imager measures all nodes simultaneously, whereas a scanning sampler probes one node at a time.

Electro-Optic Interferometer

We present the reasons for choosing an interferometer and discuss its operation. We begin by mathematically describing the EO effect, and the relationship between the voltages present on the DUT, fringing fields coupled into the crystal, and resulting phase delay experienced by the optical probe. We then use this information to estimate the temporal resolution of the system. Following this discussion, we analyze the design in Fig. 69.31 to estimate the expected system sensitivity.

The refractive index in an EO crystal is altered in the presence of an electric field. The perturbed index n' is dependent on the field-free index n, field strength E, and Pockels coefficients r. By applying the techniques of Ref. 7 to x-cut $LiTaO_3$ (<3 m> point group), a material commonly used for EO sampling, we find (neglecting terms quadratic in field strength E_y)

$$n_y' = n_y - \frac{n_y^3}{2}\left(r_{22}E_y + r_{13}E_z\right) = n_y + \Delta n_y, \tag{1a}$$

$$n_z' = n_z - \frac{n_z^3}{2}\left(r_{33}E_z\right) = n_z + \Delta n_z. \tag{1b}$$

Numeric subscripts are indices of the tensor elements, and y, z subscripts are direction vectors in crystalline coordinates; z is parallel to the optic axis. These equations show that the refractive index along y is influenced by the electric fringing fields directed along both y and z, whereas the index along z is influenced only by fringing fields along z. It is also evident that the optical probe polarization must be aligned to measure the desired refractive index perturbation, while the optic axis of the crystal must be aligned on the DUT such that the fringing fields of interest maximize the index perturbation.

If we substitute values for $LiTaO_3$[7] into Eqs. (1a) and (1b), we find that $\Delta n_z \approx 4.4\,\Delta n_y$, and the contribution from E_y is negligible. In point sampling, it is common (and convenient) to measure the induced birefringence, which is the difference in index perturbation along z and y, or

$$\Delta n_{zy} = \Delta n_z - \Delta n_y \approx \Delta n_z / 1.3.$$

Since the refractive index change along z is greater than that along y and greater than the induced birefringence, system sensitivity will be maximized by measuring Δn_z. An interferometer was chosen for this purpose. [Note: EO materials from other point groups (e.g., ZnTe, <43 m>) have greater sensitivity when the induced birefringence is measured.]

Having determined that we wish to measure the refractive index perturbation using an interferometer, we must consider how it will be used. An interferometer is sensitive to phase delays imposed on a propagating optical wavefront, which in our case is the probe beam. As an optical beam traverses a dielectric material, it suffers a phase delay $\Delta\Gamma$, determined by the refractive index n, wavelength λ, and material thickness X:

$$\Delta\Gamma = \int_0^X \frac{2\pi}{\lambda} n(x)\,dx. \tag{2}$$

We showed above that the refractive index was dependent upon the electric fringing field, but we must also consider that the fringing field is not uniform throughout the thickness of the material. As a result, the refractive index is a function of depth x, determined by the penetration depth of the fringing field into the crystal.

Substituting Eq. (1b) into Eq. (2), we obtain a static phase delay component Γ_0 (independent of E fields):

$$\Gamma_0 = \frac{2\pi}{\lambda} n_z X, \tag{3a}$$

and a dynamic phase delay attributed to the EO effect $\Delta\Gamma_{EO}$. The interferometer measures $\Delta\Gamma_{EO}$, given by

$$\Delta\Gamma_{EO} = \frac{\pi}{\lambda} n_z^3 r_{33} \int_0^X E_z(x)\,dx. \tag{3b}$$

The E-field distribution within the crystal depends upon the test structure. For this example, consider a coplanar waveguide on which we wish to probe the E-field at the center of the gap g. In general, if a superstrate having the same relative dielectric constant as the substrate (ε_{sub}) is placed on a coplanar structure, we would expect the fringing fields in the superstrate to be confined to a depth comparable to the gap separating device features. When the superstrate is the EO crystal (dielectric = ε_{EO}), the depth of the fringing field, g', is dependent upon the ratio of the two dielectric constants; the confinement depth becomes $g' \cong g\,\varepsilon_{sub}/\varepsilon_{EO}$. The field strength decreases rapidly inside the crystal, so we approximate the integral with the product $E_z^{surface}\,g'$, where $E_z^{surface}$ is the transverse E-field magnitude at the surface of the crystal. We then obtain

$$\Delta\Gamma_{EO} \cong \frac{\pi}{\lambda} n_z^3 r_{33}\left(\frac{\varepsilon_{sub}\, g E_z^{surface}}{\varepsilon_{EO}}\right), \tag{3c}$$

or in words, the measured phase change at any point is proportional to the E-field at that point. The voltage on the gap V^{gap} is the product of the gap and the E-field:

$$V^{gap} = g\,E_z^{surface}. \tag{3d}$$

Note that for a given value of $\Delta\Gamma_{EO}$, the voltage is independent of the gap, whereas the field depends upon the gap. This can be understood by considering that a device having a larger gap has deeper fringing-field penetration in the crystal. The fields have a longer interaction length with the probe; hence, the field required to produce a given phase change is reduced.

Temporal resolution of the system is determined by the largest of (1) response time of the EO material, or (2) probe-pulse duration convolved with the fringing fields profile; this convolution is approximately equal to the sum of the pulse FWHM and the time of flight t_{fl} of an infinitely short pulse through the fringing fields. The EO response is limited by phonon resonance and for $LiTaO_3$ is of the order of 10^{-14} s.[8] The probe pulse is ≈100-fs FWHM and can be reduced to ≈50-fs FWHM using a pulse compressor. The optical path length through the fringing fields is $pl = (2ng\,\varepsilon_{sub}/\varepsilon_{EO})$. Time of flight $t_{fl} = pl/c$, with c = speed of light in vacuum. For a coplanar waveguide fabricated on silicon ($\varepsilon_{sub} = 11.9$), having $g = 10\ \mu$m, and $LiTaO_3$ ($n \approx 2.2$, $\varepsilon_{EO} = 43$), we find $t_{fl} \approx 40$ fs. From these values, we expect (temporal resolution) ≈ (pulse FWHM + t_{fl}) = 140 fs, well below 1 ps.

Interferometer Operation

Now that we have described how Pockels effect alters the phase of an optical probe beam, we discuss the interferometer in detail. We begin with its intensity transfer function and discuss the ideal case. We then consider factors that cause deviations from ideal that reduce system sensitivity, and estimate their magnitude. Finally, we consider how to optimize system sensitivity given these constraints.

The normalized intensity measured by the detector, $I_d = I_{out}/I_{ref}$, is the ratio of the output intensity from the interferometer to the intensity present in the reference leg:

$$I_d \equiv \frac{I_{out}}{I_{ref}} = (1+\alpha) + 2\sqrt{\alpha}\cos(\delta) + b. \tag{4}$$

I_d depends on $\alpha = I_{DUT}/I_{ref}$, the normalized intensity in the device leg, the phase difference δ between the E-field of the optical probe in each leg, and normalized background illumination b. Using Eqs. (3a) and (3c) to expand δ, we get

$$\delta = 2(\Gamma_0 + \Delta\Gamma_{EO}) \equiv 2\Gamma, \tag{5}$$

where Γ_0 was redefined to include both the static phase difference governed by the differing lengths of the interferometer legs, as well as the static phase delay of the EO crystal. The factor of 2 results from using reflective sampling. The probe passes through the fringing field two times, accumulating twice the phase delay.

In an ideal interferometer $\alpha = 1$ and $b = 0$, and Eq. (4) reduces to

$$I_d \propto \cos^2(\Gamma), \tag{6}$$

which is also the intensity transfer function used to describe point sampling. As a result, all modulation and detection principles described herein apply equally to a system such as that in Ref. 2, wherein a variable retarder is used in place of the quarter-wave plate or optical compensator. The variable retarder would take on the modulation function of the piezoelectric actuator, as discussed in the section entitled **Modulation**.

CCD's have a finite electron well-capacity, and consequently, sensitivity will be greatest when the ratio q/Q is maximized, where q = number of electrons attributed to the EO signal and Q = total number of electrons. Assuming that the number of electrons in each pixel is linearly proportional to the incident radiant flux,

$$Q \propto I_d, \tag{7a}$$

and

$$q \propto \Delta I_{EO} \equiv I_d - I_d\big|_{\Delta\Gamma_{EO}=0}, \tag{7b}$$

where ΔI_{EO} is the intensity contribution from the EO effect alone. Combining Eqs. (4), (5), (7a), and (7b) yields

$$\frac{q}{Q} = \frac{\cos 2(\Gamma_0 + \Delta\Gamma_{EO}) - \cos 2(\Gamma_0)}{p + \cos 2(\Gamma_0 + \Delta\Gamma_{EO})}, \tag{8}$$

where

$$p \equiv \frac{1+\alpha+b}{2\sqrt{\alpha}}. \tag{9}$$

In the small-signal limit, Eq. (8) becomes

$$\frac{q}{Q}\bigg|_{\mathrm{Lim}\,\Delta\Gamma_{EO}\to 0} = f(p,\Gamma_0)\Delta\Gamma_{EO}, \tag{10a}$$

where

$$f(p,\Gamma_0)\equiv\left[\frac{2\sin(2\Gamma_0)}{p+\cos(2\Gamma_0)}\right]. \tag{10b}$$

Equation (10a) describes the fraction of electrons in each pixel attributed to the EO effect. We now consider how to use this information to optimize the system sensitivity.

Figure 69.32(a) presents a plot of Eq. (9), and Fig. 69.32(b) shows $f(p, \Gamma_0)$ defined in Eq. (10b) for the nonideal case p = 1.05. From Fig. 69.32(b), we see that $f(p, \Gamma_0)$ has two points for which the amplitude is a maximum. We wish to find Γ_0^{opt}—bias points for which this function is optimized. To do so, we take the derivative of $f(p, \Gamma_0)$ with respect to Γ_0, equate to zero, and solve

$$\Gamma_0^{opt}(p)=\frac{1}{2}\cos^{-1}\left(-p^{-1}\right). \tag{11}$$

Equation (11), plotted in Fig. 69.32(c), shows a distinct Γ_0 that maximizes q/Q. Therefore, we wish to optically bias the interferometer at this point, about which the small EO signal is superimposed. We note that for an ideal interferometer p = 1, giving $\Gamma_0^{opt} = \pi/2$ where the derivative of Eq. (6) is zero. This conclusion is very different from wide-bandwidth detectors used in point sampling that achieve maximum sensitivity when $\Gamma_0 = \pi/4$, where the derivative of Eq. (6) is maximized, as explained in Ref. 2. In the general case of a nonideal interferometer, two solutions exist [as originally expected from Fig. 69.32(b)], one on either side of $\pi/2$.

Substituting Eq. (11) into Eq. (10b), we find

$$f(p,\Gamma_0)\Big|_{\Gamma_0=\Gamma_0^{opt}}=\frac{2}{p\sqrt{1-p^{-2}}}\equiv f^{opt}(p). \tag{12}$$

The factor $f^{opt}(p)$ is also plotted in Fig. 69.32(c). It has the greatest value for an ideal interferometer and decreases as we depart from ideal.

Until now, we have ignored sources of optical phase-front distortions to the probe beam. Each optical component has a finite surface accuracy and refractive index inhomogeneities. These inaccuracies are stationary in time, and spatially random, so the cumulative error is the rms combination of all components. These errors will make it impossible to achieve optimum system sensitivity at every pixel simultaneously, but two observations can be made:

1. As the region-of-interest (ROI) is decreased (within diffraction limits), the magnitude of phase distortions will decrease, and

2. As a system, sensitivity will be maximized when the average optical bias point in the ROI corresponds to the optimum bias conditions.

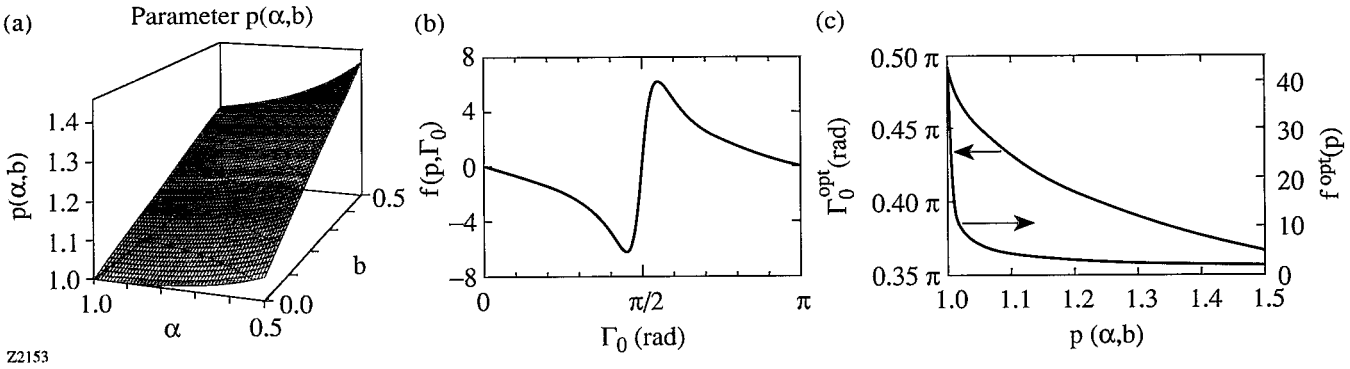

Figure 69.32
(a) Parameter $p(\alpha, b) = 1$ for an ideal interferometer and increases as (α, b) depart from ideal. (b) Sensitivity factor $f(p, \Gamma_0)$ for an arbitrary nonideal interferometer (p = 1.05) has two peaks, corresponding to optimum operating bias points Γ_0^{opt}. (c) Optimum optical bias points Γ_0^{opt} and sensitivity factor $f^{opt}(p)$ can be determined knowing p.

We have shown that there exists an optimum bias point about which we must modulate our signal. To determine this bias point, we must understand the origins of α and b and estimate their magnitudes.

In an ideal interferometer, the beam splitter would be infinitely thin, so that reflections occur only at one surface. Pellicle beam splitters are thin but are subject to acoustic and mechanical vibrations, making them unsuitable for this application. A thick beam splitter is more stable, but reflections from the second surface must be eliminated. Coated optics are an option, but we chose to eliminate unwanted reflections by using a wedged window. The beam is incident at Brewster's angle at the first surface such that reflectivity of p-polarized radiation is zero. The beam splitter then behaves ideally, i.e., $\alpha = 1.0$.

Background illumination, factor b in Eq. (4), is radiation collected by the detector that does not contribute to the desired signal. Fresnel reflections occur at each dielectric interface (window or lens), as in Fig. 69.33(a). Each transmitted beam is the superposition of many reflections. Beams that experience multiple reflections will be delayed more than the duration of the probe pulse, so will not interfere. To estimate b_{lens}, we compare the intensity of transmitted light delayed by more than $n_1 t$ to that delayed by exactly $n_1 t$. For a system of M windows and lenses,

$$b_{\text{lens}} = \left(1 - R^2\right)^{-M} - 1. \tag{13}$$

Since system sensitivity decreases with increasing b, it is advantageous to minimize the reflection coefficient R at each optical element by using coated optics. A conservative estimate for the system shown in Fig. 69.31 (not all optics shown) having seven uncoated BK-7 windows (R = 0.04) gives $b_{\text{lens}} \cong 1.2\%$.

Fresnel reflections occur also at the surface of the crystal. Most EO materials used for sampling have a large refractive index, giving large reflections. The following expression for background contributions from the crystal, b_{EO}, is evident from Fig. 69.33(b):

$$b_{\text{EO}} = 1 - \left(1 - R_{\text{EO}}\right)^{-2}. \tag{14}$$

Reflections from the top surface of the crystal are potentially the most detrimental to system performance. Uncoated $LiTaO_3$ has $R_{\text{EO}} \cong 14\%$, making $b_{\text{EO}} \cong 26\%$; anti-reflection (AR) coatings, which make $R_{\text{EO}} \cong 0.03$, yield $b_{\text{EO}} \cong 6\%$. R_{EO} also effectively reduces α to α' by

$$\alpha' = \frac{I_{\text{DUT}}}{I_{\text{ref}}}\left(1 - R_{\text{EO}}\right)^2 = \alpha\left(1 - R_{\text{EO}}\right)^2, \tag{15}$$

since only a fraction of the incident pulse makes exactly one round-trip through the crystal.

Uncoated $LiTaO_3$ makes $\alpha' = 0.74\ \alpha$, whereas coated $LiTaO_3$ produces $\alpha' = 0.94\ \alpha$. To minimize these detrimental effects, the crystal requires a nearly perfect AR coating on the first surface ($R_{\text{EO}} = 0$) and a perfect HR coating ($R = 1$) on the second surface.

The final source of background is the light reflected by the DUT from the fiber-coupled beam used to trigger the photoconductive switch. A conservative estimate assumes that the fiber is positioned at the DUT and pointed directly toward the interferometer beam splitter [Fig. 69.33(c)]. The results of this analysis will be at least an order of magnitude too large because the estimate neglects the following facts:

(1) the fiber is directed toward the DUT and will shadow reflected light;

(2) the DUT will absorb incident photons;

(3) the polarizing filter will attenuate reflected (scattered) light that is depolarized; and

(4) the photoconductive switch may be located outside the image area.

From the above argument, the results of the following simplified analysis will be reduced by a factor of 10.

The divergence angle of the beam is determined by the fiber diameter and wavelength. A fraction of the light is reflected off the beam splitter toward the camera. The distance between the relay lens and DUT is determined by the desired magnification m and lens focal length f. The lens has a finite aperture and collects only a fraction of the diverging beam from the fiber, b_{fiber}. Assuming a gaussian beam from the fiber tip, this simplified approach yields

$$b_{\text{fiber}} \approx \frac{I_{\text{ex}} R_{\text{bs}}}{I_{\text{ref}}}\,\text{erf}\left(\frac{D}{D'}\right), \tag{16a}$$

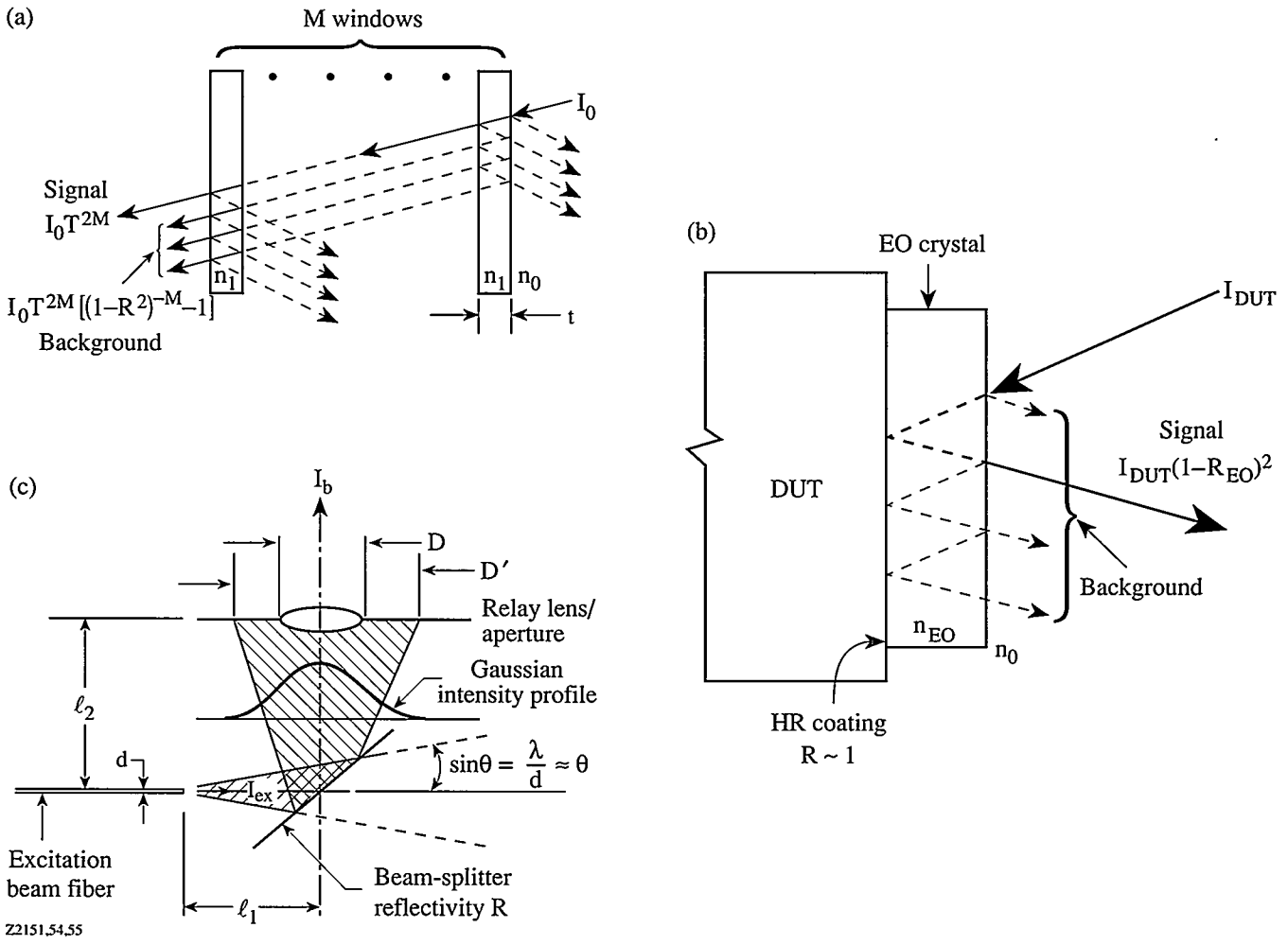

Figure 69.33
Factors that degrade interferometer performance: (a) multiple reflections from windows and lenses [R = intensity reflection coefficient, T = intensity transmission coefficient = $(1-R)$], (b) Fresnel reflections at the surface of the EO crystal, and (c) light escaping from excitation fiber.

where

$$\frac{D}{D'} = \frac{\lambda Dm}{2df(m+1)} \tag{16b}$$

and where I_{ex} = intensity of the excitation pulse (≈1 mW), $I_{ref} \approx 10\ \mu$W (for pixel saturation), R_{bs} = beam-splitter reflectivity, erf( ) is the error function, D = lens-aperture diameter, $D' = 1/e$ beam diameter at the lens, λ = wavelength, and d = fiber-core diameter.

Clearly, R_{bs} and m should be minimized, and f should be large. From Eqs. (16a) and (16b), typical operating conditions give $b_{fiber} \cong 13\%$, which we reduce to 1.3%, as discussed above.

We have considered several factors that contribute to the nonideal terms α and b in the interferometer transfer function. It is essential to use precision optics and minimize front-surface reflections from the EO crystal to prevent system degradation. Proper adjustment of the excitation beam intensity and fiber placement will limit background contributions from the excitation source. Finally, coated optics will reduce multiple reflections from other system optics. For a well-designed system having an AR-coated crystal, we obtain $b = b_{EO} + b_{fiber} + b_{lens} \cong 0.06 + 0.012 + 0.013 = 0.085$, and $\alpha = 0.94$, thus making $p \cong 1.044$. This value for p will be used in the remaining discussion.

System Linearity and Sensitivity

Linearity of the measurement system can be derived from the ratio of Eqs. (10a) and (8), where Γ_0 is replaced with Γ_0^{opt}, and $\Delta\Gamma_{EO}$ is a small-signal perturbation about Γ_0^{opt}. Evaluating linearity at $p = 1.044$, one can show that the measured response is linear within ±5% for $|\Delta\Gamma_{EO}| < 0.015$ rad; this is more than adequate for expected signals.

We have obtained an expression for the optimum sensitivity factor $f^{opt}(p)$ and numerical estimates of the parameter p. The next step is to determine the measurement resolution of the system given this information. First, we determine the system dynamic range (DR) and minimum resolvable phase change, then the voltage and E-field needed to produce this phase change.

From Eq. (10), we can determine DR_{signal} if we assume that the pixel is nearly saturated so that $Q \approx Q_{well}$. The CCD has an electronic noise-equivalent signal $q_{eq} = 30$ electrons, shot noise $q_{shot} = 40$ electrons, and well capacity $Q_{well} = 80 \times 10^3$ electrons.[9] Setting $q_{noise} = \left(q_{eq}^2 + q_{shot}^2\right)^{1/2} = 50$ electrons, we find

$$DR_{signal} = 20 \cdot \log\left(\frac{Q_{well}}{q_{noise}}\frac{q}{Q}\right)\Bigg|_{\frac{q}{Q}=f^{opt}(p)\Delta\Gamma_{EO}}. \quad (17)$$

For $\Delta\Gamma_{EO} = \pm 0.015$ rad (the limit of "linear" range) and $p = 1.044$, we find $f^{opt}(p) = 6.25$, and $DR_{signal} = 43$ dB.

The minimum detectable signal $\Delta\Gamma_{EO}^{min}$ is that which makes $q/Q = q_{noise}/Q_{well}$:

$$\Delta\Gamma_{EO}^{min} = \left(\frac{q_{noise}}{Q_{well}\, f^{opt}(p)}\right), \quad (18)$$

which gives $\Delta\Gamma_{EO}^{min} = 100$ μrad, corresponding to $\lambda/6 \times 10^4$ resolution.

We relate $\Delta\Gamma_{EO}^{min}$ to the voltage necessary to produce it, using Eqs. (3c) and (3d):

$$\Delta\Gamma_{EO}^{min} \cong \frac{\pi}{\lambda} n_z^3 r_{33}\left(\frac{\varepsilon_{sub}}{\varepsilon_{EO}}\right)\left(V^{gap,min}\right). \quad (19)$$

The minimum detectable voltage $V^{gap,min}$ is constant for any (coplanar) gap geometry. $E_z^{surface,min}$ is the minimum field, which, if present at the surface of the crystal, could be resolved by the system:

$$E_z^{surface,min} = \frac{V^{gap,min}}{g}. \quad (20)$$

When testing a device fabricated on silicon ($\varepsilon_{sub} = 11.9$) using $LiTaO_3$ ($\varepsilon_{EO} = 43$, $r_{33} = 33$ pm/V, $n_z = n_e = 2.180$),[7] and $\lambda = 800$ nm, we find $\Delta\Gamma_{EO}^{min} = 3.7 \times 10^{-4}\, V^{gap,min}$. By equating $\Delta\Gamma_{EO}^{min}$ to 100 μrad, $V^{gap,min} = 270$ mV, which corresponds to 27 kV/m on a 10-μm gap.

This sensitivity is well suited to measurement of microwave devices and complex transmission line structures. Several enhancements can be made to improve suitability for digital applications. A nonlinear organic salt known as DAST has $\varepsilon_{EO} = 7.0$, Pockels coefficient $r_{11} = 160$ pm/V, and $n = 2.460$.[10] From Eq. (19), this would increase sensitivity by a factor of 43. Cooling the sensor reduces shot noise so that $q_{noise} \cong q_{eq}$, thus by Eq. (18), increasing sensitivity by a factor of 1.6. In combination, these produce $V^{gap,min} \cong 4$ mV, and $E_z^{surface,min} \cong 400$ V/m.

Modulation

Having discussed the attributes of an integrating detector, we now show how the signal is modulated about the desired operating bias point. We first discuss how the signal is modulated in each image and the timing required. We then discuss the characteristics of a frame transfer sensor and how to use these characteristics to our advantage.

Figure 69.34(a) is an expanded view of Eq. (6), about $\pi/2$. In the absence of an electric field, points A and B have equal intensity when the optical bias is adjusted to $\pm\Gamma_0^{opt}$ by displacing the reference mirror. When an E-field is present on the DUT, the resulting EO phase shift is added to the optical bias. This causes the intensity at point A to increase to C, while that at point B decreases to D. Analysis of the data is achieved by subtracting field D from B, and C from A.

The data-acquisition system is synchronized to the camera's pixel and field clocks and acquires images with the timing shown in Fig. 69.34(b). The electrical bias on the device's photoconductive switch is synchronously modulated at the 30-Hz camera field clock frequency, thus decreasing $1/f$ noise (both laser and mechanical vibrations of the interferometer). The reference mirror position is modulated at 1/2 the bias frequency. A trigger pulse generated on the mutual rising edge of bias and actuator signals triggers the digitization of

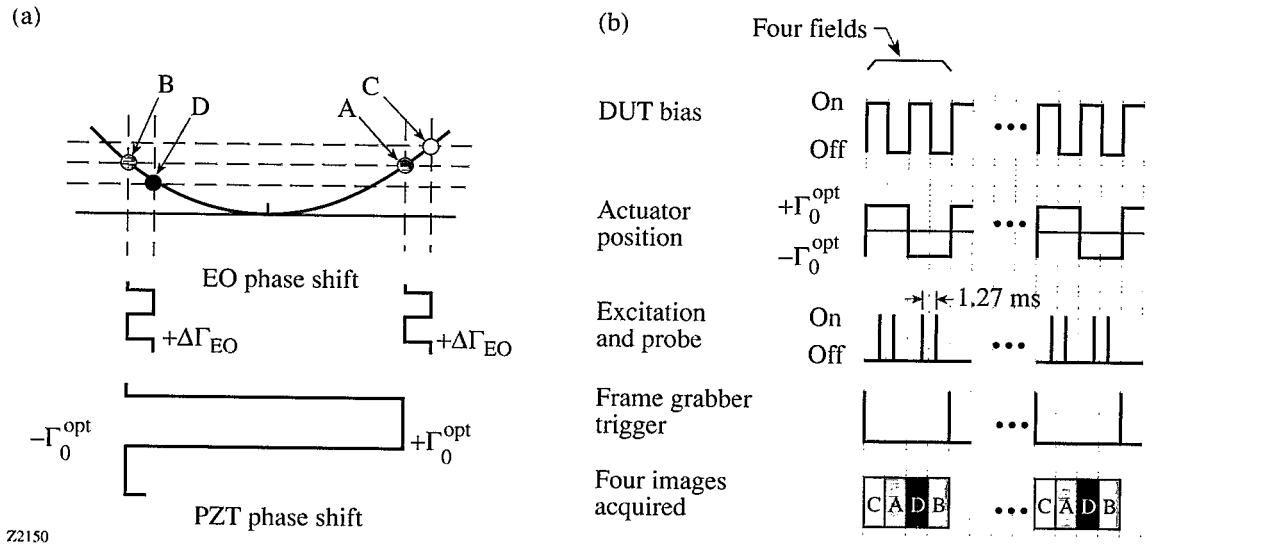

Figure 69.34
Modulation: (a) expansion of Eq. (6) about an interferometric null showing EO modulation about $\pm\Gamma_0^{opt}$ bias points, (b) modulation and image capture timing diagram.

four consecutive fields, corresponding to points C, A, D, B in Fig. 69.34(a).

The frame transfer CCD has two discrete sensor regions: an active-pixel site and a storage site of equal size. Each field is acquired over a 1/60-s integration period. An advantage of using a detector with a 1/60-s integration period is that 60-Hz electrical noise will average to zero. During integration, the active pixels integrate charge proportional to photon flux, while electrons in the storage site are clocked to the output amplifiers. During frame transfer, charges in the active pixels are transferred vertically via "bucket brigade" into the storage site. Charge transfer causes slight smearing due to transfer inefficiency, and distortion occurs for charge packets that are transferred through brightly illuminated pixels.

A high-speed modulator "gates" the laser "on" immediately before and after alternate frame transfer cycles, and "off" at all other times. This eliminates charge smearing during frame transfer and reduces the effective laser- and vibration-noise bandwidth significantly. The limiting speed for this modulation is governed by the frame transfer period (1.27 ms for our camera). If the laser is gated "on" for ~100 pulses, the effective modulation frequency would be ~750 Hz.

Summary

We have described and analyzed an ultrafast EO imaging system that uses an interferometer and CCD detector to map 2-D electric fields on an optoelectronic device. It is comparable to an ultrafast sampling oscilloscope having more than 180,000 channels. Limitations caused by using an integrating detector are reviewed, and optimum operating conditions are identified. Techniques are presented that allow modulation of the signals at 750 Hz, which will reduce sensitivity to laser and mechanical $1/f$ noise. System sensitivity in the absence of laser noise is estimated to be 270 mV, corresponding to 27 kV/m for a 10-μm coplanar structure. These values make the system well suited for testing microwave devices. Sensor cooling and the use of alternative EO materials should improve sensitivity by factors of 1.6 and 43, respectively, making the minimum resolvable voltage 4 mV. The system would then be easily capable of digital (e.g., CMOS) circuit evaluation.

ACKNOWLEDGMENT

This work is supported by the University Research Initiative at the University of Rochester sponsored by the Army Research Office grant number DAAL03-92-G-0112. Additional support was received from the Army Research Office AASERT grant number DAAH04-95-1-0428 and the Frank J. Horton Graduate Fellowship Program.

REFERENCES

1. J. A. Valdmanis, G. Mourou, and C. W. Gabel, Appl. Phys. Lett. **41**, 211 (1982).
2. J. M. Wiesenfeld, IBM J. Res. Develop. **34**, 141 (1990).
3. K. E. Meyer and G. A. Mourou, in *Picosecond Electronics and Optoelectronics*, edited by G. A. Mourou, D. M. Bloom, and C. H. Lee (Springer-Verlag, New York, 1985), pp. 46–49.
4. W. Mertin, Opt. Quantum Electron. **28**, 801 (1996).
5. W. R. Donaldson, L. Kingsley, M. Weiner, A. Kim, and R. Zeto, J. Appl. Phys. **68**, 6453 (1990).
6. R. A. Falk *et al.*, in *Ninth IEEE International Pulsed Power Conference*, Digest of Technical Papers, edited by K. R. Prestwich and W. L. Baker (IEEE, New York, 1993), Vol. 1, pp. 88–91.
7. A. Yariv and P. Yeh, *Optical Waves in Crystals: Propagation and Control of Laser Radiation* (Wiley, New York, 1984), pp. 220–245.
8. D. H. Auston and M. C. Nuss, IEEE J. Quantum Electron. **24**, 184 (1988).
9. *Area Array Image Sensor Products Data Book*, Texas Instruments (1994), pp. 2-135–2-151.
10. Molecular Optoelectronics Corporation, 877 25th St. Watervliet, NY, 12189. DAST has a different Pockels coefficient matrix than the <3 m> point group, so substituting r_{11} for r_{33} is an approximation.

Nuclear Diagnostics for High-Density Implosions

The measurement of fuel compression, specifically the density-radius product (ρR), is of fundamental importance in analyzing ICF implosions. To probe the large values of ρR anticipated for OMEGA (and NIF) experiments, nuclear diagnostics must be used.

Three ρR diagnostics are being developed for OMEGA. They rely on detecting the following nuclear particles: (1) energetic D and T ions (knock-ons) produced by colliding 14-MeV neutrons;[1] (2) elastically scattered DT neutrons;[2,3] and (3) tertiary DT neutrons.[2,4] The starting point for generating each of these particles is the 14-MeV neutron produced in DT fusion, i.e.,

$$\mathrm{D}+\mathrm{T}\rightarrow\alpha+n(14.1\ \mathrm{MeV}). \tag{1}$$

A small percentage of these neutrons (typically less than 0.01% for ICF conditions) will scatter elastically from D or T ions in the fuel (a prime indicates a scattered particle):

$$n+\mathrm{D}(\text{or T})\rightarrow n'+\mathrm{D}'(\text{or T}'), \tag{2}$$

where D′ will be produced in a continuous spectrum from 0 to 12.5 MeV and T′ in the range of 0 to 10.6 MeV, with the remainder of the 14.1-MeV energy going to the scattered neutron. The number of such scattering events per DT-fusion neutron is directly proportional to the ρR of the fuel. This forms the basis for two of the nuclear diagnostics under development—knock-ons and elastically scattered neutrons: (1) the techniques for detecting the D and T knock-ons that were developed on the 24-beam OMEGA system will be extended to accommodate the higher values of ρR expected in future, near-term experiments (total target $\rho R \le 200$ mg/cm^2); and (2) techniques for detecting the elastically scattered neutrons and separating that signal from the expected neutron background will be investigated.

The third diagnostic involves reactions with the knock-on D and T ions. As these ions pass through the fuel, there is a small probability that they will undergo an in-flight fusion reaction with one of the thermal fuel ions:

$$\mathrm{D}'(0-12.5\ \mathrm{MeV})+\mathrm{T}(\text{thermal})\rightarrow\alpha+n''(12-30\ \mathrm{MeV}), \tag{3}$$

and similarly for the knock-on tritons, where n'' indicates a neutron scattered by an already scattered D. Because the D and T knock-ons are charged particles, they will be slowing down as they fuse. This can complicate the interpretation of the diagnostic signal, as the rate of slowing down depends on the temperature in the fuel as well as the density. The number of these high-energy neutrons from the tertiary reaction actually measures the product (ρR) ($\rho R'$), where R' is either the radius of the target or the range of the D or T knock-on ions, whichever is smaller. The first factor of ρR comes from the production of the knock-ons. Thus, for small ρR (OMEGA), the tertiary yield varies as $(\rho R)^2$, and for large ρR (NIF), it is proportional to ρR.

This article presents more details about these three diagnostics, together with comments on where further development is necessary. Two other nuclear diagnostics are under consideration but will not be discussed here, because they involve the additional complication of adding He^3 to the target. These two diagnostics use the D-He^3 proton: the energy loss of the 14.7-MeV proton from thermal D-He^3 fusion can measure the target ρR up to several hundred mg/cm^2,[1] and tertiary protons from in-flight D-He^3 fusion, using knock-on D or He^3 ions, can measure the ρR of the He^3 in the target.[5] The detection of these protons from different directions can give information about gross asymmetries of the compressed core.

Knock-Ons

The knock-on diagnostic was developed at LLE for the 24-beam OMEGA laser and used to diagnose implosions with a fuel ρR up to ~30 mg/cm^2 and with a comparable $\rho\Delta R$ for the glass shell around the fuel.[6] For values of fuel-plus-shell ρR in excess of 100 mg/cm^2, the knock-on spectrum becomes

substantially distorted due to significant slowing down of the D and T ions as they pass through the target; this can introduce some uncertainty in interpretation of the diagnostic signal. It is important to spectrally resolve the high-energy portion of this charged-particle signal, to separate the knock-ons from other sources of energetic ions, and to determine how the knock-on spectrum has been modified by slowing down in the target. Gross spectral resolution was obtained on the 24-beam OMEGA laser using stacked track detectors.[1,6] Higher resolution will be obtained in future OMEGA experiments using a charged-particle spectrometer. This will extend the applicability of the knock-on diagnostic to meet the needs of the OMEGA experimental program for the first few years of operation.

To illustrate how the diagnostic can be used, Fig. 69.35 shows the calculated spectrum of knock-on deuterons for the simple model of a hot DT core surrounded by a "cold" (0.5-keV), denser CH shell. A characteristic feature of the spectrum is a peak at high energies produced by the forward-peaked cross section for scattering with 14-MeV neutrons. (This peak contains ~16% of the deuteron knock-ons.) Figure 69.35 shows how the peak is shifted to lower energies due to increased slowing down as the $\rho\Delta R$ of the plastic shell increases. [The energy loss in the fuel is relatively small in this example because the fuel temperature is high and the ρR is small (40 mg/cm^2).] The peak changes position and shape but remains well defined. By spectrally resolving this peak, it is possible to obtain simultaneously two important pieces of information about the compressed core: the position of the peak determines the $\rho\Delta R$ of the plastic shell, and the number of knock-on deuterons in the peak determines the ρR of the fuel. The fuel ρR is related to the number of deuterons in the peak (N_D) and the DT neutron yield (Y) by the following relation:

$$\rho R = 83\, N_D/Y \quad \text{g/cm}^2 \tag{4}$$

for equimolar DT. A similar relation is available for knock-on tritons, but the more energetic deuterons can be used to diagnose higher values of ρR.

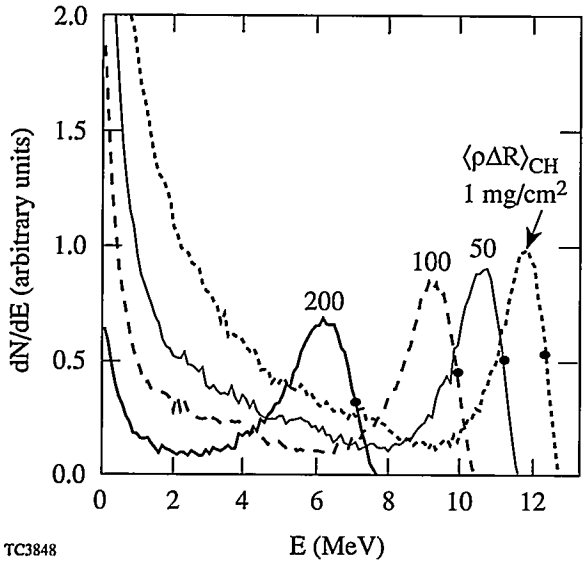

Figure 69.35
Calculated spectrum of knock-on deuterons escaping from compressed targets, with constant fuel ρR (40 mg/cm^2) and variable $\rho\Delta R$ (1 to 200 mg/cm^2) for a CH shell (of temperature 0.5 keV) surrounding the fuel. The energy shift of the high-energy peak measures the $\rho\Delta R$ of the shell, and the number of deuterons in the peak determines the ρR of the fuel.

To facilitate measurement of the knock-on spectrum, a charged-particle spectrometer[7] is being developed at MIT for OMEGA experiments. The spectrometer uses a 7.5-kG magnet to momentum select the particles and deflect them from the straight-line path followed by neutrons and x rays. The charged-particle paths are determined from trajectory calculations. The magnet has recently been tested at MIT using protons with energies from 1 to 15 MeV. As depicted in Fig. 69.36, the particles are deflected and then impinge onto a detector plane where they are intercepted by a combination of charged-coupled devices (CCD's) and CR-39 plastic track detectors. As demonstrated in recent experimental studies at MIT, the CCD's act as high-resolution energy detectors. Through the combination of magnetic momentum selection and the energy determination of the detectors, either CCD or track, the energy and identity of each particle will be uniquely specified. From these data, the spectra of all charged particles will be constructed, and vital information about the core conditions and dynamics will be measured.

This spectrometer also forms the basis of a joint proposal between MIT, LLE, and LLNL for a NIF diagnostic that will measure both the implosion symmetry and the core ρR.[5] This makes use of very energetic tertiary protons (~31 MeV) that can easily penetrate all plasmas envisaged for the NIF. For example, the range of these protons is ~3 g/cm^2, whereas the ρR expected for a typical NIF capsule is ~1 g/cm^2. Even for some implosion scenarios simulated for OMEGA,[5] situations have been encountered where these tertiary protons could prove particularly useful for determining core conditions, beyond the range of applicability of the knock-on diagnostic.

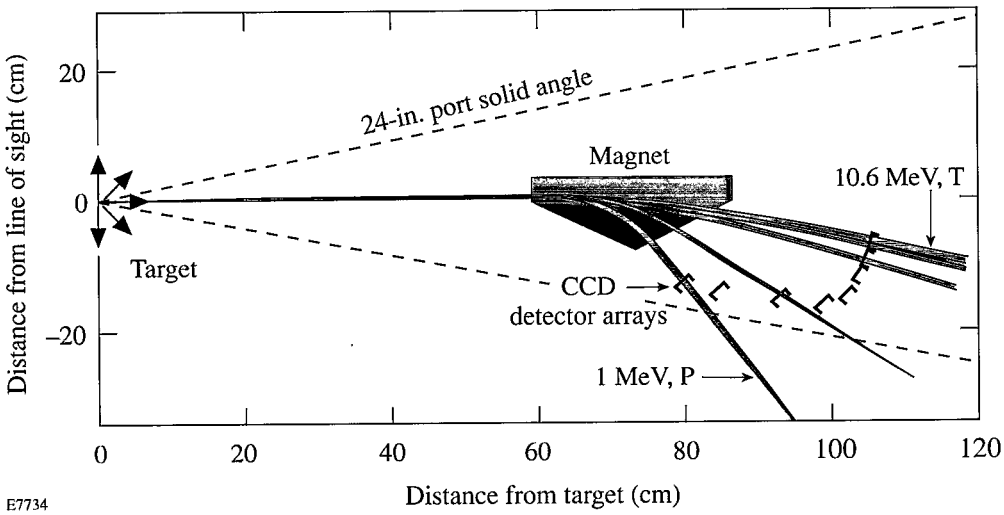

Figure 69.36
Measurement of the spectrum of charged particles escaping from the target. A spectrometer uses a magnet to momentum select the particles and CCD's or track detectors to detect the particles and provide energy resolution.

Elastically Scattered Neutrons

The second reaction product from (n,D) and (n,T) scattering, namely the elastically scattered neutron, could be used to diagnose all values of ρR of interest to ICF. Like the charged-particle knock-ons, the number of these is directly proportional to the ρR of the fuel but, since they are neutral, they do not slow down in the target, and therefore this diagnostic is not limited to small values of ρR.

To determine if the elastically scattered neutrons can be separated from other sources of neutrons produced in the target, Monte Carlo calculations have been performed to calculate the spectrum of all neutrons emerging from the target. The spectra for two values of ρR are shown in Fig. 69.37. The peak at 14 MeV is, of course, the primary source from DT fusion. The neutrons above 14 MeV are from tertiary reactions, discussed in the next section. In the range of 8 to 10 MeV, there are contributions from many sources including $(n,2n)$ reactions with deuterium and $T(T,2n)\alpha$ reactions; it is not possible to separate out the contribution from elastic scattering in this region. However, in the range of 10 to 13 MeV, elastically scattered neutrons completely dominate the spectrum. The number of neutrons in this range is large enough to provide a model-independent determination of ρR for all experiments planned for OMEGA and NIF. (It should be noted that the two curves shown in Fig. 69.37 are distinguishable because they are both normalized to the primary yield.)

The main effort in neutron diagnostic development is to devise a method for shielding against the effects of the primary DT neutrons. These 14-MeV neutrons can lose energy as they scatter from structural material around the target chamber or within the diagnostic instrument itself, and they can enter the 10- to 13-MeV window that is being scanned for the elastically scattered neutrons from the target.

Tertiary Neutrons

A significant portion of the tertiary neutron spectrum lies above the 14-MeV primary source (Fig. 69.37). There are no other reactions that can produce neutrons in the range of ~15 to 30 MeV. However, because this is a tertiary reaction, the number of neutrons produced is several orders of magnitude lower than for elastic scattering. For the NIF, yields are sufficiently high that this should not be a problem. However, for OMEGA experiments, it might be difficult to collect a statistically useful number of tertiaries for targets with low neutron yields. Time-of-flight detectors with a solid angle of $\sim 10^{-5}$ should be adequate for the NIF. On OMEGA, it might be necessary to use carbon activation foils that could increase the detection solid angle by an order of magnitude. The carbon foils would detect all neutrons with energy above ~18 MeV, without spectral resolution. However, since there are no other sources of neutrons in this range, spectral separation is not necessary.

For OMEGA implosions, the "cold" part of the fuel will have temperatures below ~1 keV throughout the implosion. In this range, the slowing down of the high-energy knock-on deuterons is relatively temperature independent, for the intermediate step in tertiary-neutron production. Figure 69.38 shows the expected ratio of tertiary neutrons (detected by a carbon foil) to the primary DT fusion yield as a function of ρR, assuming temperatures of 0.5 keV and 1 keV. The neutron ratio determines ρR to within ±5% for these conditions. Superim-

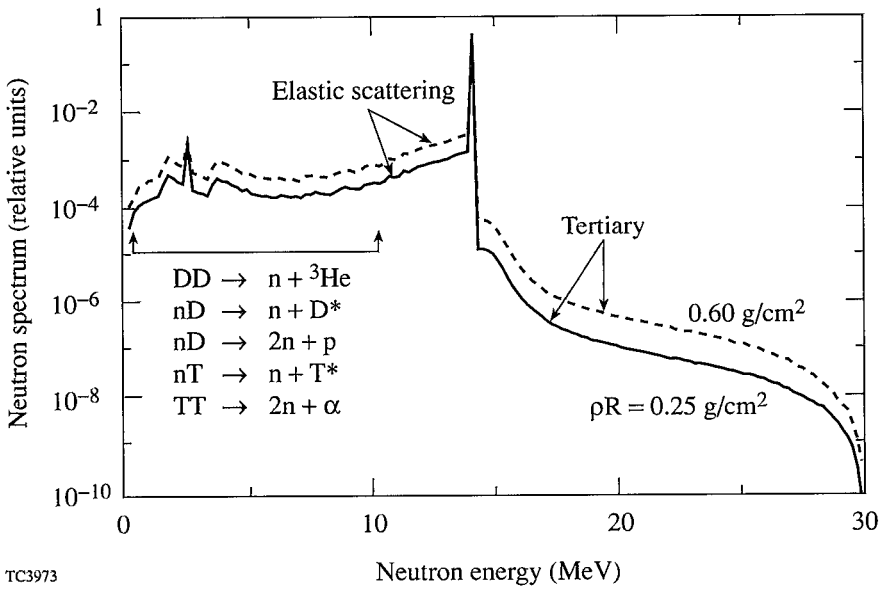

Figure 69.37
Calculated spectrum of neutrons escaping from a compressed target for two values of ρR. In the energy range between 10 MeV and 13 MeV, elastically scattered neutrons dominate; above 15 MeV, only tertiary neutrons contribute.

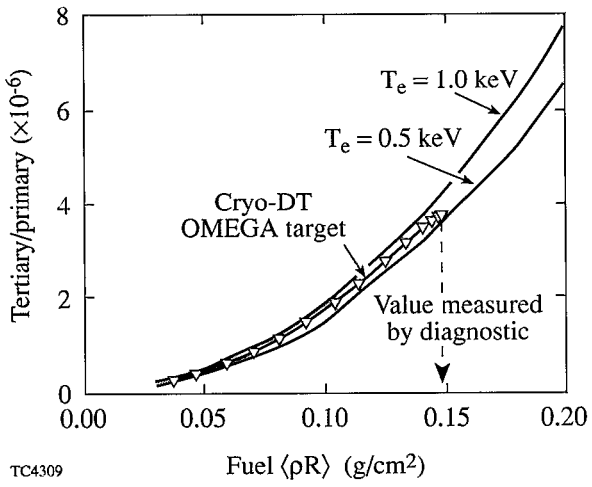

Figure 69.38
Ratio of tertiary neutrons to the primary DT fusion yield as a function of fuel ρR for two values of fuel temperature.

posed on Fig. 69.38 are results from a full hydrodynamic simulation of an OMEGA implosion showing how the neutron ratio varies with the neutron-weighted ρR at different times during the implosion. The neutron ratio varies roughly as $(\rho R)^2$, as the range of the knock-on deuterons and tritons is larger than or comparable to the radius of the target.

For a burning NIF target, the temperatures will be considerably higher and the temperature dependence of the diagnostic will be much larger. Uncertainties of interpretation due to this temperature sensitivity can be reduced by a detailed analysis of the tertiary spectrum using a neutron time-of-flight detector.

ACKNOWLEDGMENT

This work was supported by the U.S. Department of Energy Office of Inertial Confinement Fusion under Cooperative Agreement No. DE-FC03-92SF19460, the University of Rochester, and the New York State Energy Research and Development Authority. The support of DOE does not constitute an endorsement by DOE of the views expressed in this article.

REFERENCES

1. S. Skupsky and S. Kacenjar, J. Appl. Phys. **52**, 2608 (1981).
2. H. Azechi, M. D. Cable, and R. O. Stapf, Laser Part. Beams **9**, 119 (1991).
3. S. Cremer and S. Skupsky, "Diagnosing High-ρR Implosions Using Elastically Scattered DT Neutrons," presented at the 26th Anomalous Absorption Conference, Fairbanks, AK, 26–30 August 1996.
4. D. R. Welch, H. Kislev, and G. H. Miley, Rev. Sci. Instrum. **59**, 610 (1988).
5. R. D. Petrasso, C. K. Li, M. D. Cable, S. M. Pollaine, S. W. Haan, T. P. Bernat, J. D. Kilkenny, S. Cremer, J. P. Knauer, C. P. Verdon, and R. L. Kremens, Phys. Rev. Lett. **77**, 2718 (1996).
6. R. L. McCrory, J. M. Soures, C. P. Verdon, F. J. Marshall, S. A. Letzring, S. Skupsky, T. J. Kessler, R. L. Kremens, J. P. Knauer, H. Kim, J. Delettrez, R. L. Keck, and D. K. Bradley, Nature **335**, 225 (1988).
7. D. G. Hicks, C. K. Li, R. D. Petrasso, F. H. Seguin, B. E. Burke, J. P. Knauer, S. Cremer, R. L. Kremens, M. D. Cable, and T. W. Phillips, "Design of an Electronic Charged Particle Spectrometer to Measure (ρR) on Inertial Fusion Experiments," to be published in the Review of Scientific Instruments.

Publications and Conference Presentations

Publications

K. L. Baker, R. P. Drake, B. S. Bauer, K. G. Estabrook, A. M. Rubenchik, C. Labaune, H. A. Baldis, N. Renard, S. D. Baton, E. Schifano, A. Michard, W. Seka, and R. E. Bahr, "Thomson Scattering Measurements of the Langmuir Wave Spectra Resulting from Stimulated Raman Scattering," Phys. Rev. Lett. **77**, 67 (1996).

S.-H. Chen, J. C. Mastrangelo, and H. Shi, "Electroluminescent Diodes Using Cyclohexane-Based Glass-Forming Liquid Crystals and Their Analogues," in *Liquid Crystals for Advanced Technologies*, edited by T. J. Bunning, S.-H. Chen, W. Hawthorne, N. Koide, and T. Kajiyama, Materials Research Society Symposium Proceedings (Materials Research Society, Pittsburgh, PA, 1996), Vol. 425, pp. 233–238.

S.-H. Chen, H. Shi, B. M. Conger, J. C. Mastrangelo, and T. Tsutsui, "Novel Vitrifiable Liquid Crystals as Optical Materials," Adv. Mater. **8**, 998 (1996).

S.-H. Chen, H. Shi, B. M. Conger, D. Katsis, and J. C. Mastrangelo, "Novel Vitrified Liquid Crystals and Potential Applications," in *Liquid Crystals for Advanced Technologies*, edited by T. J. Bunning, S.-H. Chen, W. Hawthorne, N. Koide, and T. Kajiyama, Materials Research Society Symposium Proceedings (Materials Research Society, Pittsburgh, PA, 1996), Vol. 425, pp. 13–18.

S.-H. Chen, H. Shi, and J. C. Mastrangelo "Use of Glass-Forming Liquid Crystal Materials for Electroluminescent Diodes," in *Liquid Crystals for Advanced Technologies*, edited by T. J. Bunning, S.-H. Chen, W. Hawthorne, N. Koide, and T. Kajiyama, Materials Research Society Symposium Proceedings (Materials Research Society, Pittsburgh, PA, 1996), Vol. 425, pp. 225–232.

B. M. Conger, H. Shi, S.-H. Chen, and T. Tsutsui, "Polarized Fluorescence from Vitrified Liquid Crystalline Films," in *Liquid Crystals for Advanced Technologies*, edited by T. J. Bunning, S.-H. Chen, W. Hawthorne, N. Koide, and T. Kajiyama, Materials Research Society Symposium Proceedings (Materials Research Society, Pittsburgh, PA, 1996), Vol. 425, pp. 239–244.

V. N. Goncharov, R. Betti, R. L. McCrory, and C. P. Verdon, "Self-Consistent Stability Analysis of Ablation Fronts with Small Froude Numbers," Phys. Plasmas **3**, 4665 (1996).

J. C. Mastrangelo, S.-H. Chen, T. N. Blanton, and A. Bashir-Hashemi, "Vitrification and Morphological Stability of Liquid Crystals," in *Liquid Crystals for Advanced Technologies*, edited by T. J. Bunning, S.-H. Chen, W. Hawthorne, N. Koide, and T. Kajiyama, Materials Research Society Symposium Proceedings (Materials Research Society, Pittsburgh, PA, 1996), Vol. 425, pp. 19–25.

C. J. McKinstrie and E. J. Turano, "Spatiotemporal Evolution of Parametric Instabilities Driven by Short Laser Pulses: One-Dimensional Analysis," Phys. Plasmas **3**, 4683 (1996).

A. V. Okishev, M. D. Skeldon, S. A. Letzring, W. R. Donaldson, A. Babushkin, and W. Seka, "The Pulse-Shaping System for the 60-Beam, 30-kJ (UV) OMEGA Laser," in *Superintense Laser Fields*, edited by A. A. Andreev and V. M. Gordienko (SPIE, Bellingham, WA, 1995), Vol. 2770, pp. 10–17.

H. Shi, D. Katsis, S.-H. Chen, M. E. De Rosa, W. W. Adams, and T. J. Bunning, "Dynamics of Defect Annihilation in Vitrified Liquid Crystalline (VLC) Thin Films Upon Thermal Annealing," in *Liquid Crystals for Advanced Technologies*, edited by T. J. Bunning, S.-H. Chen, W. Hawthorne, N. Koide, and T. Kajiyama, Materials Research Society Symposium Proceedings (Materials Research Society, Pittsburgh, PA, 1996), Vol. 425, pp. 27–32.

A. V. Okishev and W. Seka, "Diode-Pumped Nd:YLF Master Oscillator for the 30-kJ (UV), 60-Beam OMEGA Laser Facility," to be published in the IEEE Journal of Selected Topics in Quantum Electronics.

A. V. Okishev and W. Seka, "Diode-Pumped Single-Frequency Nd:YLF Laser for the 60-Beam OMEGA Laser Pulse-Shaping System," to be published in Solid State Lasers VI.

R. D. Petrasso, C. K. Li, M. D. Cable, S. M. Pollaine, S. W. Haan, T. P. Bernat, J. D. Kilkenny, S. Cremer, J. P. Knauer, C. P. Verdon, and R. L. Kremens, "Implosion Symmetry and ρR Measurements of the National Ignition Facility from Nascent 31-MeV Tertiary Protons," to be published in Physical Review Letters.

J. Z. Roach, A. Ninkov, S. W. Swales, and T. Morris, "Design and Evaluation of a Screen CCD Imaging System," to be published in Optical Engineering.

J. Z. Roach and S. W. Swales, "A Network-Based Imaging System for the OMEGA Laser System," to be published in SPIE's Proceedings of the European Symposium on Lasers, Optics, and Vision for Productivity in Manufacturing I, Micropolis, Besangon, France, 10–14 June 1996.

A. W. Schmid, T. J. Kessler, S. Papernov, and J. Barone, "Low-Surface-Energy Photoresist as a Medium for Optical Replication," to be published in Applied Physics Letters.

H. Shi, B. M. Conger, and S.-H. Chen, "Circularly Polarized Fluorescence from Chiral Nematic Liquid Crystalline Films: Theory and Experiment," to be published in Liquid Crystals.

M. J. Shoup III, J. H. Kelly, and D. L. Smith, "Design and Testing of a Large-Aperture, High-Gain, Brewster's-Angle Zigzag Nd:Glass Slab Amplifier," to be published in Applied Optics.

A. Simon, "Comparison Between SBS Theories and Experiment," to be published in the Proceedings of the LaJolla Summer School '95, Plasma Physics and Technology (AIP).

J. M. Soures, "Inertial Fusion Research Using the OMEGA Laser Facility," to be published in Physics Today.

J. M. Soures, S. J. Loucks, R. L. McCrory, C. P. Verdon, A. Babushkin, R. E. Bahr, T. R. Boehly, R. Boni, D. K. Bradley, D. L. Brown, J. A. Delettrez, R. S. Craxton, W. R. Donaldson, R. Epstein, R. Gram, D. R. Harding, P. A. Jaanimagi, S. D. Jacobs, K. Kearney, R. L. Keck, J. H. Kelly, T. J. Kessler, R. L. Kremens, J. P. Knauer, S. A. Letzring, D. J. Lonobile, L. D. Lund, F. J. Marshall, P. W. McKenty, D. D. Meyerhofer, S. F. B. Morse, A. Okishev, S. Papernov, G. Pien, W. Seka, R. W. Short, M. J. Shoup, III, M. D. Skeldon, S. Skupsky, A. W. Schmid, D. J. Smith, S. Swales, M. D. Wittman, and B. Yaakobi, "The Role of the Laboratory for Laser Energetics in the National Ignition Facility Project," to be published in Fusion Technology.

E. A. Startsev and C. J. McKinstrie, "Multiple Scale Derivation of the Relativistic Ponderomotive Force," to be published in Physical Review E.

M. D. Wittman, R. Q. Gram, H. Kim, C. K. Immesoete, S. G. Noyes, and S. Scarantino, "Increased Retention Time for Hydrogen and Other Gases by Polymer Shells Using Optically Transparent Aluminum Layers," to be published in the Journal of Vacuum Science and Technology.

W. Xiong, Y. Kostoulas, X. Weng, P. M. Fauchet, and R. Sobolewski, "Femtosecond Study of the Electronic Structure in Semiconducting Y-Ba-Cu-O," to be published in Physical Review B.

Z. Xu, Ju. V. Vandyshev, P. M. Fauchet, C. W. Rella, H. A. Schwettman, and C. C. Tsai, "Ultrafast Excitation and De-excitation of Local Vibrational Modes in a Solid Matrix: The Si-H Bond in Amorphous Silicon," to be published in the Proceedings of OSA's Tenth International Topical Meeting on Ultrafast Phenomena, San Diego, CA, 28 May–1 June 1996.

B. Yaakobi, F. J. Marshall, and J. A. Delettrez, "Abel Inversion of Cryogenic Laser Target Images," to be published in Optics Communications.

J. D. Zuegel and W. Seka, "Direct Measurements of Lower-Level Lifetime in Nd:YLF," to be published in the Bulletin of the American Physical Society.

J. D. Zuegel and W. Seka, "Upconversion and Reduced $^4F_{3/2}$ Upper-State Lifetime in Intensely Pumped Nd:YLF," to be published in Optics Letters.